

In-Flight Jet Engine Thrust Prediction by Measuring the Engine Vibration Isolators Deformation

by
B.J. Poppe

September 15th, 2021

Delft University of Technology
Faculty of Aerospace Engineering



MASTER THESIS

In-Flight Jet Engine Thrust Prediction by Measuring the Engine Vibration Isolators Deformation

by

B.J. Poppe

To obtain the degree of Master of Science at the Delft University of Technology,
to be defended publicly on the 15th of September 2021.

Graduation committee

Chair:	Dr. ir. M.M. van Paassen	TU Delft
Supervisor:	Dr. ir. C.C. de Visser	TU Delft
Committee:	Dr. F. Yin	TU Delft
	Ir. T.J. Mulder	TU Delft

Student number: 4966856
Project duration: 15 September 2020 - 15 September 2021
Faculty: Aerospace Engineering
Master track: Control & Operations
Master profile: Control & Simulation



Preface

This document is the thesis of my Master's graduation project which I started in September 2020. This report will finalise my Aerospace Engineering Master and with that my life as a student. The origin of the graduation topic is found when my system identification lecturer, Coen, discussed a missing component of aircraft system identification, namely the in-flight thrust measurement of the jet engine. As a part-time aircraft mechanic a broader knowledge of aircraft systems and construction is established, leading to an original and innovative way of determining the in-flight jet engine thrust. After presenting this method, Coen was very enthusiastic and introduced me to the PH-LAB team to work out the research approach.

The process to go from an idea to an implemented system is divided into three phases. The first phase is to determine if the rubber vibration isolators have the right characteristics to be used as a thrust sensor. The following phase is the implementation on a jet engine which is mounted in an experiment setup. The last phase is a full implementation on the PH-LAB and develop a generic approach to implement this system on other development or research aircraft.

With a clearly defined research scope, I started with my literature study to ensure that this method has not been tested or implemented before, which is not the case. With this in mind, Hans managed to clear a budget to purchase a vibration isolator for the experiments. This was followed by several weeks of designing and manufacturing the experiment setup, during which my brother Michiel was a great help. For the design and construction of the hydraulic control system my dad, Bennie, was a great support. With the experiment setup manufactured and the vibration isolator ordered, Dave and Alexander provided guidance with the build up of the whole experiment system.

With two months of experiment data which required an extra hard drive, the data analyses are started. The analysis are focused on determining the influence of engine vibrations, temperatures and engine weight on the measured deformation. Followed by the construction of a mathematical model of the vibration isolator that relates the measured deformation to the applied thrust force.

I would like to thank Coen especially for being my supervisor, motivating me during the research and guiding me in the model estimation elements. Coen even makes me consider continuing this research in the form of a PhD, something I didn't expect to do. My gratitude goes to the aircraft technicians of the PH-LAB, Menno and Fred, for thinking with me on the future implementation, ordering the parts and even personally delivering them. Another thanks goes to Ferdinand for thinking with me on the future implementation of the system into the PH-LAB and the accompanied restrictions on the design. Thanks to Xander and Hans for recognising the potentials of this sensor as test pilots, and an extra thanks to Hans for funding the research, which I understand is unusual for a master student. I would like to thank Johan Martens of Textron Aviation for providing me with technical drawings which allowed me to start my experiment setup design.

The largest thank you goes to my friends and family, as they are the people that supported me the most in the difficult times and cheered me on when I needed it. In particular, I cannot thank enough Ben and Luuk with whom I shared these years at the TU Delft, studying many hours together and having hefty discussions on irrelevant topics which cooled down after some beers. I would like to thank my girlfriend Anna-Maria for always joining me to the UB and providing valuable feedback on detailing the final thesis.

Summary

The direct measurement of in-flight thrust is considered impracticable, and estimating the in-flight thrust is achieved by placing the engine in an altitude test cell, where the measured thrust is related to certain engine parameters. This is a tedious and expensive process that requires regular recalibration due to engine wear. Most general aviation jets, that often are used as research platform, are constructed with the engines on the side of the rear fuselage. In this construction, the thrust is transferred to the fuselage via two vibration isolators, which consist of silicone rubber and hence easily deform. The thrust force which the engine generates also deforms this rubber and is the basis of this research.

By designing and manufacturing an experiment setup, a vibration isolator of the Cessna model 550 is subjected to simulations of engine vibrations, temperature and varying weight. These experiments are performed to determine the influence of these variables on the deformation caused by the thrust force. Note that the thrust direction is perpendicular to the engine vibrations, which are mainly due to rotor imbalance.

The experiments showed that the thrust force deformation is not influenced by varying engine vibration frequency or amplitude within the operational range. Also, temperatures up to 80 degrees showed no measurable influence on the deformation characteristics of the vibration isolator in thrust direction. This is due to the fact that silicone rubber has little-varying mechanical properties over a large temperature range. The weight of the engine on the other hand has a direct relation to the measured deflection. An increase of 500 newtons of engine weight, resulted in a reduction of the perpendicular thrust deflection of 5 μm . This is at a maximum thrust force of 6 kN and corresponds to approximately an error of 30 Newtons. The engine weight is dependent on the directional acceleration and therefore varies during flight manoeuvres.

Relating the measured force and correlating deformation is not trivial. The force-deformation curve shows nonlinear dynamic behaviour in the form of a hysteresis. This is in line with the expected behaviour of viscoelastic material, which bears both viscous and elastic properties. Combining a static nonlinear polynomial model with a linear dynamic output error model resulted in an average model error below 1% of the maximum thrust force on the validation data. In this estimation and validation data, the input force cycles through random thrust values in the operational range to map the complete force-deformation hysteresis.

The combinations of static nonlinear models and linear dynamic models are called Hammerstein and Wiener models, depending on the order. To aim for a generic model approach, piecewise-linear nonlinearity are introduced, to include possible backlash or dead-zone behaviour. Combining this piecewise-linear nonlinearity, in combination with the best performing output error model, resulted in a 56 newtons root mean square error on the validation data which ranges up to 6.5 kN. The average model error in the operational range (> 2 kN) on 37 hours of validation data is 1.1%.

To conclude, using the engine vibration isolator as a thrust sensor is found highly feasible. This opens a new field of research and allows for non commercial research groups to measure direct in-flight thrust for a fraction of the costs.

Table of Contents

Preface	iii
Summary	v
List of Figures	ix
List of Tables	xi
List of Abbreviations	xiii
List of Symbols	xvi
I Literature Study	1
1 Introduction	3
2 Aircraft System Identification	5
2.1 System Identification	5
2.2 Aircraft System Identification	6
2.3 Jet Engine System Identification	6
2.4 Direct Thrust Measurement	7
2.5 Proposed Direct Thrust Measurement	7
2.6 Conclusion	9
3 Aircraft Engine Characteristics	11
3.1 Engine Description	11
3.2 Engine Vibrations	13
3.3 Conclusion	15
4 Aircraft Engine Vibration Isolator Characteristics	17
4.1 Vibration Isolators	17
4.2 Elastomeric Characteristics	17
4.2.1 Viscoelastic Properties	17
4.2.2 Hysteresis	18
4.2.3 Stiffness Effects	19
4.2.4 Material Ageing	22
4.3 Engine Isolator Specifications	22
4.3.1 Spring Rates	23
4.3.2 Isolator Loading	24
4.4 Conclusion	26
5 Experiment Setup	27
5.1 Test Machine	27
5.2 Test Frame	28
5.3 Test Object	28
5.4 Sensors	29
5.5 Conclusion	30

6	Model Construction	31
6.1	Physical Models	31
6.1.1	Maxwell Model	32
6.1.2	Voigt model	32
6.2	Linear Regression Model	33
6.2.1	Define a Linear Regression Model	34
6.3	Conclusion	36
7	Problem Formulation	37
7.1	Research Question	37
7.2	Research Objective	38
7.3	Research Scope	38
7.4	Research Necessities	38
7.5	Research Assumptions	38
8	Conclusion	41
II	Thesis	43
9	Introduction	45
9.1	Context and Problem Statement	45
9.2	Approach and Challenges	45
9.3	Contributions	46
9.4	Research Objective	46
10	Experiment Setup	47
10.1	Elastomer Test System	47
10.1.1	MTS Software	48
10.2	Thrust Force Simulation	48
10.2.1	Hydraulic Cylinder	50
10.2.2	Adaptors	54
10.3	Deformation Measurement	55
10.4	Conclusion	56
11	Experiments	59
11.1	Characterisation Experiments	59
11.1.1	Frequency	59
11.1.2	Amplitude	60
11.1.3	Mean Load	60
11.2	Temperature experiments	61
11.3	Identification Experiments	61
11.4	Conclusion	61
12	Experiment Results	63
12.1	Characterisation Experiments	63
12.1.1	Vibrations	63
12.1.2	Mean load	64
12.2	Temperature	65
12.3	Identification Experiments	67
12.4	Conclusion	68
13	Model Construction	69
13.1	Physical Models	69
13.1.1	Maxwell Model	70
13.1.2	Kelvin-Voigt Model	70
13.2	Static Nonlinear Models	71

13.2.1	Define a Linear Regression Model	72
13.3	Linear Dynamic Models	74
13.3.1	Equation Error Model	74
13.3.2	Output Error Model	75
13.4	Nonlinear Models	76
13.4.1	Decomposition of Block-oriented Nonlinear Systems	78
13.4.2	Piecewise-linear	80
13.5	Conclusion	84
14	Model Results	85
14.1	Model Parameters	85
14.2	Physical Models	86
14.3	Static Nonlinear Model	86
14.4	Linear Dynamic Models	87
14.4.1	Equation Error Models	87
14.4.2	Output Error Models	87
14.5	Nonlinear Dynamic Models	88
14.6	Model comparison	89
14.7	Observations	91
14.8	Conclusion	93
15	Conclusions	95
16	Recommendations	97
III	Scientific Paper	99
	References	113
A	Model performance on validation data	119

List of Figures

2.1	Representation of a dynamic system	5
2.2	Aircraft as an input-output system (Tischler & Remple, 2006)	6
2.3	Typical jet engine installation for the general aviation (Gudmundsson, 2014)	8
2.4	Forward engine vibration isolators of Cessna 560XL (Textron, 2020a)	9
3.1	Forward engine vibration isolators of Cessna model 550 (Textron, 2020b)	12
3.2	Cross-section of JT15D-4 engine (Pratt & Whitney, 1975)	13
3.3	Critical speeds of JT15D-4 (Botman, 1980)	14
3.5	Low & high rotor excited vibrations (Botman, 1980)	15
3.4	Coupled rotor modes of JT15D-4 (Botman, 1980)	16
4.1	Schematic representation of the relationship between stress and strain in different materials (Murata, Taguchi, Hamada & McCabe, 2000)	18
4.2	Dynamic stress-strain plot of viscous material (Gent, 2012)	18
4.3	Static deformation of the JT15D-4 vibration isolator	19
4.4	Schematic diagrams illustrating the simplest form of time-temperature equivalence (Ward & Sweeney, 2004)	21
4.5	Stress-strain plot of viscous material showing Mullins effect (Laka, 2016)	21
4.6	Radial deformation characteristics of the JT15-4 vibration isolator	22
4.7	Static and dynamic representation of spring rate (Larsen, 1966)	23
4.8	Engine vibration isolator positions with respect to the centre of gravity	24
4.9	Engine front mount structure dimensions in meters	25
5.1	Static deflection process graph	28
5.2	Lower engine mount of PH-LAB engine 2	29
6.1	Static and dynamic representation of spring rate (Mukhopadhyay, Adhikari & Batou, 2019)	31
6.2	Maxwell model (Schreurs, 2012)	32
6.3	Voigt model (Schreurs, 2012)	32
10.1	MTS Elastomer Test System 831	47
10.2	Thrust simulation setup designs	49
10.3	MTS Elastomer Test System 831 with adaptors and test object	50
10.4	Cylinder preparation	51
10.5	Hydraulic scheme of experiment setup	52
10.6	Hydraulic components stand construction	53
10.7	Zwick-Roell's cylinder calibration setup	54
10.8	Horizontal mounting	55
10.9	Vertical mounting	55
10.10	Fork adaptors	55
10.11	LVDT bracket design (left) and experiment setup (right)	56
11.1	Measurement points in experiment program	60
12.1	Influence of varying frequency and amplitude on the isolator deformation.	63
12.2	Shows the influence of varying mean load levels.	64
12.3	The simulated thrust force at various frequencies, amplitudes and mean loads.	65
12.4	Temperature influence on measured deformation	66

12.5	Linearly compensated deformation	66
12.6	Engine vibration isolator characteristics at different temperatures	67
12.7	Force-deformation curve for sine input	67
13.1	Static and dynamic representation of spring rate (Mukhopadhyay et al., 2019)	70
13.2	Maxwell model (Schreurs, 2012)	70
13.3	Kelvin-Voigt model (Schreurs, 2012)	71
13.4	Hammerstein model	77
13.5	Wiener model	77
13.6	Hammerstein-Wiener model	77
13.7	Wiener-Hammerstein model	78
13.8	Four segment piecewise-linear nonlinearity model representation of the first nonlinear block NL ₁	80
13.9	Four segment piecewise-linear nonlinearity model representation of the second nonlinear block NL ₂	81
14.1	Simulated thrust force - deformation relation	86
14.2	3 th order polynomial ordinary least squares static model	87
14.3	Output error model	88
14.4	Hammerstein-Wiener model with 10 piecewise-linear input and output nodes.	89
14.5	Comparison of model characteristics on sine wave input.	90
14.6	Model error comparison	91
14.7	Hammerstein-Wiener model with sinusoidal thrust input	91
14.8	Hammerstein-Wiener model estimated with 0.003 Hz data	92

List of Tables

4.1	The vibration isolator static spring rates at normal room temperature	23
4.2	The vibration isolator dynamic spring rate for normal cruise conditions based on test data at 20Hz at normal room temperature	23
4.3	Increase of spring rate due to temperature decrease	24
4.4	Engine vibration isolator positions with respect to the centre of gravity of the engine	24
4.5	Static directional and normal engine mount forces	25
14.1	Model performance on validation data.	90

List of Abbreviations

AGARD	Advisory Group for Aerospace Research and Development
AOA	Angle Of Attack
APU	Auxiliary Power Unit
ARMAX	AutoRegressive model with eXogenous terms and Moving Average
ARX	AutoRegressive model with eXogenous terms
ATF	Altitude Test Facility
BJ	Box-Jenkins model
BLUE	Best Linear Unbiased Estimator
CAD	Computer Aided Design
CG	Centre of Gravity
CNC	Computer Numerical Control
DMA	Dynamic Mechanical Analysis
DXF	Drawing Exchange Format
FEA	Finite Element Analysis
FAA	Federal Aviation Administration
GLTB	Ground Level Test Bench
GLS	Generalised Least Squares
GMM	Generalised Maxwell Model
HP	High Pressure
IPS	Inch Per Second
LP	Low Pressure
LTI	Linear Time Invariant
LVDT	Linear Variable Differential Transformer
MLE	Maximum Likely Estimation
MISO	Multiple Input - Single Output
NARX	Nonlinear AutoRegressive model with eXogenous terms
NASA	National Aeronautics and Space Administration
NLR	Nederlands Lucht- en Ruimtevaartcentrum
OE	Output Error model
OLS	Ordinary Least Squares
RMSE	Root Mean Squared Error
RPM	Revolutions Per Minute
RPS	Revolutions Per Second
SAE	Society of Automotive Engineers
SISO	Single Input - Single Output
SLS	Standard Linear Solid
ToF	Time of Flight
UAV	Unmanned Aerial Vehicle
WLS	Weighted Least Squares

List of Symbols

α	Angle of attack	[rad]
β	Angle of slip	[rad]
δ	Phase angle	[rad]
γ	Material strain	%
μ	Viscosity	[Pa · s]
ω	Vibration frequency	[RPS]
ϕ	Bank angle	[rad]
ψ	Yaw angle	[rad]
σ	Material stress	[MPa]
σ_{∞}	Settled relaxation stress	[MPa]
τ	Creep time constant	[s]
θ	Parameter vector	[-]
ε	Linear regression residual	[-]
ε	Material strain	%
φ	Particle movement rate	[s ⁻¹]
φ	Regression vector	[-]
a_T	Time-temperature superposition shift	[Hz]
a_x	Linear acceleration	[$\frac{m}{s^2}$]
a_y	Linear acceleration	[$\frac{m}{s^2}$]
a_z	Linear acceleration	[$\frac{m}{s^2}$]
b	Creep rate constant	[-]
D	Diameter	[m]
e	Noise	[-]
E	Young's modulus	[GPa]
E''	Tensile loss modulus	[GPa]
E'	Tensile storage modulus	[GPa]
E^*	Complex dynamic tensile modulus	[GPa]
F	Force	[N]
P	Pressure	[$\frac{N}{m^2}$]
q	Forwar shift operator	[-]
T	Temperature	[°C]

t	Time	[s]
T_g	Glass transition temperature	[°C]
Δ	Relative deformation over one minute of time	[%]
Δ'	Creep rate	[-]
δ_a	Aileron deflection angle	[rad]
δ_e	Elevator deflection angle	[rad]
δ_r	Rudder deflection angle	[rad]
δ_t	Throttle setting	[%]
$\hat{\theta}$	Linear regression estimator	[-]
θ	Pitch angle	[rad]
Θ	Unknown model parameters	[-]
N_1	Low pressure engine section rotation speed	[%]
N_2	High pressure engine section rotation speed	[%]
p	Angular velocity	$\left[\frac{rad}{s}\right]$
q	Angular velocity	$\left[\frac{rad}{s}\right]$
r	Angular velocity	$\left[\frac{rad}{s}\right]$
u	Translational velocity	$\left[\frac{m}{s}\right]$
v	Translational velocity	$\left[\frac{m}{s}\right]$
w	Translational velocity	$\left[\frac{m}{s}\right]$

Part I

Literature Study

Chapter 1

Introduction

Gordon Moore, CEO and co-founder of Intel, famously predicted that the number of transistors of a computer chip would double roughly every two years. Alternatively, the price of the same calculating power would decrease at the same rate. Although transistors are beginning to approach their theoretical limit, much progress has been made since this statement in the 60s. A significant contributor to the demand for ever-increasing computational power has been the desire to model and simulate more complex systems, with an ever-increasing degree of accuracy. For the aerospace industry, one of the implementations is modelling the behaviour of aircraft and aircraft sub-systems.

One of the first approaches for obtaining static and dynamic parameters from flight data was given by Milliken (1947) using frequency response data and a simple semi-graphical method for the analysis. Drastic improvement in aircraft aerodynamic modelling techniques came in the late 1960s and early 1970s, because of the availability of digital computers and progress in the new technical discipline known as system identification (Morelli & Klein, 2016). A good practice definition of system identification is given by Zadeh (1962) :

"System identification is the determination, on the basis of observation of input and output, of a system within a specified class of systems to which the system under test is equivalent."

This indicates the crucial importance of accurate, reliable in- and output data in order to construct a reliable analysis. Most input parameters such as control surface deflections can be measured directly by installing a rotary angle encoder. However, as of the writing of this report, it is generally accepted that thrust has not such properties. This is substantiated by the first sentence of the book *Guide to In-Flight Thrust Measurement of Turbojets and Fan Engines*, which states: 'Direct measurement of thrust and drag in flight is not feasible' (AGARD, 1979). The basis of this literature study and graduation research is the pursuit to disprove this statement.

The method of thrust measurement discussed in this literature study is based on measuring the deformation of the engine vibration isolators. The vibration isolators attach the engine to the airframe and reduce the audible vibrations conveyance. No research has been performed on using the aircraft vibration isolator deformation for a thrust estimate. Therefore, this literature study focuses on the characteristics of the vibration isolators and the feasibility of the proposed thrust measurement method.

The report is structured as follows: in chapter 2, the theoretical background on system identification is discussed. Subsequently, the focus is placed on aircraft and more specifically jet engine identification methods. The direct thrust measurement is the field of interest for this thesis and therefore elaborated on further. This is followed by a detailed description of the proposed method. Chapter 3 elaborates on the engine in question, namely, the Pratt & Whitney JT15D-4. Starting with the engine description, followed by the engine vibration characteristics. Afterwards, in chapter 4 the characteristics of the engine vibration isolator are discussed. Among others, the elastomeric characteristics, stiffness effects and the isolator specifications are described in detail. This is followed chapter 5 which describes the experiment test bench, frame and object and the therefore required sensors. Subsequently, within chapter 7, the problem formulation is outlined. This includes the research question, objective, scope, and the according assumptions. Finally, in chapter 8, the conclusion of this literature study is drawn by discussing the results of the previously mentioned chapters.

Chapter 2

Aircraft System Identification

Aircraft system identification is a procedure that can rapidly and efficiently extract an accurate dynamic model of an aircraft by measuring the response to known specific inputs. The same method can be used to characterise subsystems like actuators, rotor systems or engines as in this case. The main applications of aircraft system identification include piloted simulation models, comparison of wind tunnel and flight measurement, validation and improvement of physics-based simulation models, flight-control system development and validation, and handling-qualities specification compliance testing (Tischler & Remple, 2006).

2.1 System Identification

The subject of system identification is closely related to the other problems in dynamics, and is accordingly explained by Jategaonkar (2006). For a dynamic system described in state space, three quantities that mainly describe the system are the inputs u , the outputs z or y , and the system model functions f and g , see fig. 2.1. Depending upon the availability of the in- and output, three different types of problems are observed in the system theory:

1. Simulation deals with finding the outputs y for given inputs u and given system functions f and g .
2. The control problem aims to find the control inputs u for given f and g , and y .
3. The identification problem attempts to find the system model f and g from the given measurements of inputs u and outputs z .

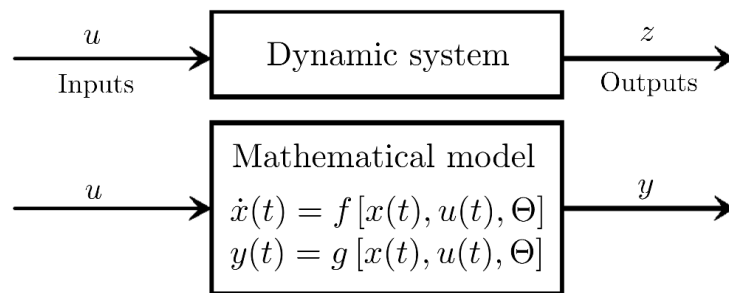


Figure 2.1: Representation of a dynamic system

Although the state variables x are not specified explicitly, they show implicitly in the description above. This is due to the fact that the outputs are functions of the internal system state variables. Similarly, the system functions f and g contain unknown parameters Θ .

The process of system identification is determining an adequate mathematical model, that usually contains differential equations with unknown parameters, that must be determined indirectly from the in- and output measurements. So, part of the process is the actual measuring of the in- and output of the system in a suitable experiment. The modelling aspect combines the determining of the required equations and the unknown model parameters Θ . This, in such a way that the model responses y match adequately with the measured system responses z . Note that perfect fits are not possible for real processes.

2.2 Aircraft System Identification

To elaborate on the system identification of aircraft, an introduction to the basic terminology and concepts are discussed according to Tischler and Remple (2006). An aircraft is seen as a dynamic system with inputs and outputs as shown in fig. 2.2. The system dynamics are excited with control inputs. For an aircraft, there are four inputs of which three are aerodynamic surfaces. A list of all inputs is given by:

- Aileron δ_a for roll control
- Elevator δ_e for pitch control
- Rudder δ_r for yaw control
- Throttle δ_t for speed control

The dynamic response of the aircraft to the inputs is recorded using onboard measurement systems. Some typical measurements for flight dynamic consideration are as follows:

- Translational velocities
- Angular velocities
- Attitudes
- Linear accelerations
- Aerodynamic angles

Additional measurements are, for example, engine responses, wing strain or the aircraft position.

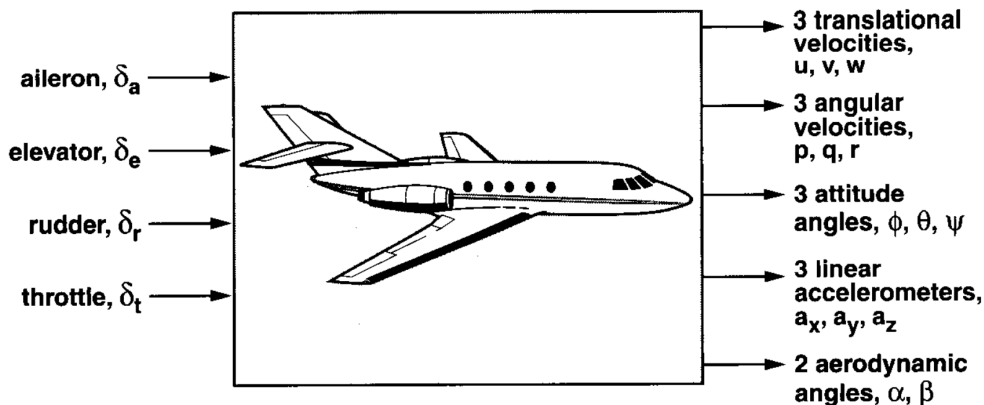


Figure 2.2: Aircraft as an input-output system (Tischler & Remple, 2006)

The mathematical model of the dynamics relates the control inputs to the measured aircraft dynamic response. The complexity of such a mathematical model can vary from a linear graph of the input-to-output response to large sets of differential equations of motion.

2.3 Jet Engine System Identification

Most in- and output parameters like aileron deflection are measured directly. This, however, is not possible for the engine thrust force. There is no general approach to measure or determine the in-flight thrust. The simplest method to determine the thrust is to use the *brochure description* of the engine performance which is tuned for each individual engine or is an average of all engines. This method uses engine parameters such as rotation speed and fuel flow to relate the output thrust to the performance of the engine in Ground Level Test Benches (GLTB) or Altitude Test Facilities (ATF) that are provided by the manufacturer (Negrão, Fanton, de La Fuente & Barbosa, 1998). The key distinction of the *brochure description* or sometimes called *overall performance method* is that it does not require special instrumentation within the propulsion system to perform measurements within the flow path. This method lacks accuracy due to external flow (wind-on/-off) effects, sensitivity to engine build standards or instrumentation that is

not built for this purpose (Abernethy et al., 1986, section 4-1). A different method of measuring the flow in the engine nozzle by using a *traversing rake* or sometimes called *swinging probe method* improves the performance estimate with a small range. The traversing rake is a beam that swings across the exhaust and measures the temperature, static- and dynamic pressure over a range of positions in the exhaust flow. This method however, requires a large test setup installation on the engine. The benefit of this method is that it allows be used in-flight (Covert, James & Kimzey, 2000; Davidson, 1964). The *gas generator* method is the most relied upon. This method is based on measurements taken within the engine and nozzle such that flow characteristics can be calculated and cross-referenced to the engine performance. The engine flow measurements are calibrated to the thrust of the engine in the ground test facility. The 'measurement' of in-flight thrust then becomes one of relating the measurements made on the ground to similar measurements made in flight. For the gas generator method, an ATF is required to calibrate the measurements (AGARD, 1979). The latest development of more accurate methods are found in Del Mònaco Monteiro, Machiaverni, Bringhenti and Tomita (2018) and Di Fiore Dos Santos, Lewis and Barbosa (2000). Several comparisons between methods are found in Hughes (1981) and Ray (1994). The standard for constructing *gas generator* models is made by the Society of Automotive Engineers (SAE) and is called AIR1701. The use of altitude test facilities is very expensive and for most research departments not feasible.

2.4 Direct Thrust Measurement

The only form of direct thrust measurement for commercial or general aviation aircraft is called the *trunnion thrust* method which refers to the force at the engine mounts or so-called trunnions. For Unmanned Aerial Vehicles (UAVs) for example, the engines can be completely suspended in load cells to measure the engine characteristics as shown by Bronz, de Marina and Hattenberger (2017) and L'Erario et al. (2020). This is because a UAV can be built solely for that purpose where an aircraft is built for transportation objectives only. Chen (2012) perhaps has the simplest yet elegant way to determine the engine thrust and uses a large concrete block, a cable and a load cell that is connected to the aircraft. This method only allows the measurement of static thrust.

The trunnion thrust method involves measuring the force transmitted to the airframe via the engine mounting trunnions. The force at the engine trunnions is not the engine thrust. This is because at the points of measurement, a part of the nacelle drag is added to the sum of forces. Also, different load paths such as fire bulkheads, slip joints, tubing or ventilation flows can change the sum of forces. This must be accounted for when measuring thrust as a force at for example the engine mounts (Adams et al., 1983). The SAE AIR1701 standard for *In-Flight Thrust Determination* states:

"If interference forces are negligible, the thrust-minus-drag of the pod would be determined and could be used directly, or corrected for drag terms, to yield in-flight net thrust"

The *Strain-gauge* method is one approach to measure the trunnion thrust, where the strain-gauges, as the name implies, measures the strain in a structure. This structure is calibrated to correlate the applied force and the according strain. This method is successfully tested on engine mounts at the NASA Dryden Flight Research Center (Connors & Sims, 1998). And also tested by measuring the deformation of mounting frames (Muhammad, Kuntjoro & Sritjahjono, 2000; Neef, Fritzen & Schuhmacher, 2003; Bauer, Friedrichs, Wulff & Werner-Spatz, 2018). Research into using the thrust pin deformation as a measure for thrust force is researched by Lei, Zhang, Wen, Ren and Lei (2017) and Lei, Li, Zhang, Gao and Wen (2018).

2.5 Proposed Direct Thrust Measurement

For general aviation, it is common to have the engines mounted on the rear fuselage of the aircraft. This is because the wings are mounted below the fuselage which leaves no space to install an engine below the wing. For aircraft with engines mounted to the rear fuselage, most mounting constructions are very similar and consists of two front mounts and one rear mount as depicted in fig. 2.3.

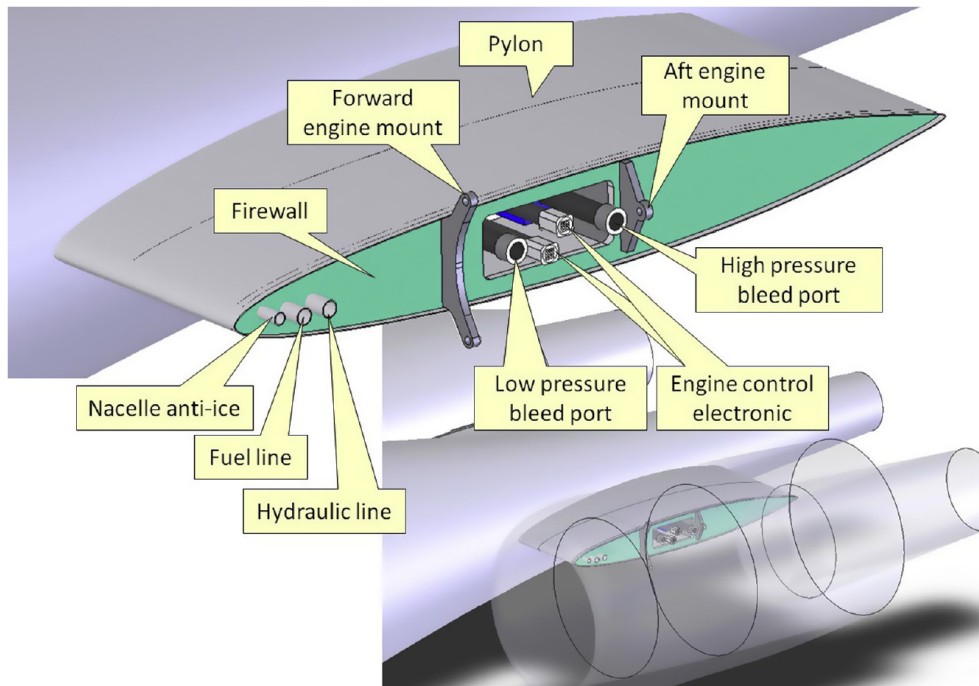


Figure 2.3: Typical jet engine installation for the general aviation (Gudmundsson, 2014)

The mounting construction of Gulfstream, Learjet and the newer Cessna aircraft are very similar. However, the shape of the engine vibration isolators is varying over the different aircraft types and manufacturers. The Gulfstream vibration isolators are circular and installed with the mounting bolt perpendicular to the flight direction. Figure 2.4, used with permission of Textron Aviation, shows a square-shaped engine vibration isolator construction of the Pratt & Whitney Canada PW545 engines where the mounting bolts are aligned with the flight direction. Which is similar to the isolator shape and construction of the Dassault Falcon aircraft.

The proposed method of new thrust measurement is based on the deformation of the vibration isolator. As mentioned in this chapter, a large amount of different methods of direct thrust determination is researched. All measuring the deformation of the metal in the engine mounts or pins. The benefit of this material is the linearity in stress-strain behaviour. However, the material is strong and shows relatively low strain behaviour and besides that, the metal shows expansion due to temperature changes. The one component in the engine mounting construction that is constructed to deform is the vibration isolator. The challenge is the highly non-linear behaviour that is observed in the deformation of rubber-like materials, on which more can be found in chapter 4.

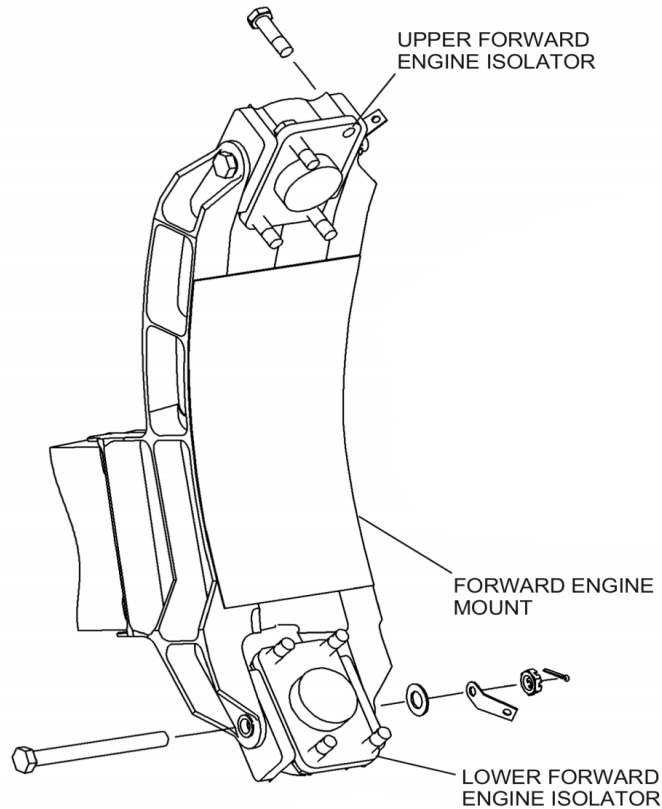


Figure 2.4: Forward engine vibration isolators of Cessna 560XL (Textron, 2020a)

2.6 Conclusion

The main applications of aircraft system identification can be found in piloted simulation models, comparison of wind tunnel and flight measurement, validation and improvement of physics-based simulation models, flight-control system development and validation, and handling-qualities specification compliance testing. For this, it is required to have accurate measurements of all aircraft in- and output parameters. Most of these parameters like surface deflection can easily be measured. Thrust however, is generally based on engine models that are constructed by the manufacturer and relate engine parameters to the test performance in the test facility. Engines degraded and thrust performances change over the life of an engine and recalibration is required, which is an expensive undertaking. This led to many kinds of research into the possibilities of determining the thrust by measuring some deformation in the engine mounts. None of these researches considered measuring the deformation of the vibration isolator. Most likely since only a specific group of aircraft with the correct mounting system is suited for this approach, namely, aircraft with fuselage engines containing three-point engine mounts. This restricts the use of this method to only a part of the general aviation aircraft which is a few percent of the total aircraft count.

Chapter 3

Aircraft Engine Characteristics

As mentioned in section 2.5, different constructions are used by different aircraft and engine manufacturers. This literature study focuses on one type of aircraft and corresponding jet engine. Namely, the Cessna Citation II (Model 550) with a corresponding Pratt & Whitney Canada JT15D-4 jet engine.

This is because the Delft University of Technology and the National Aerospace Laboratory (NLR) jointly own and operate a Cessna Citation II (model 550) under the registration PH-LAB. This aircraft is extensively modified to serve as a versatile airborne research platform. The Pratt & Whitney Canada JT15D-4 engines are mounted as shown in fig. 3.1, which is used with permission from Textron Aviation. The engine vibration isolator has a cylindrical shape. This shape is certainly uncommon, however, might prove very useful in subsequent research as the modelling might be reduced to two dimensions. This chapter presents a detailed description of the construction and characteristics of the engine.

3.1 Engine Description

The project manager of the JT15D-4 engine development, Mr Wrong (1969), sheds some light on the construction of the jet engine. The JT15D-4 is a two-spool, medium bypass ratio turbofan engine. The single-stage fan produces on average just under a 1.5 pressure ratio. The part-span shroud that is incorporated into the titanium fan blades is implemented to reduce vibrations. Behind the rotor, the airflow splits, where one part continues to the core of the engine and 3.2 parts are conducted through the engine bypass. The installation of a stator behind the fan blades reduces the flow whirl and guides the air straight down the full length of the duct.

The part that continues to the engine core first passes the inner stator, followed by the boost compressor stage, down the inter-compressor duct which leads to the high pressure (HP) compressor. The HP compressor is a single-stage centrifugal compressor (impeller) which on average produces a pressure ratio of 7. On an average axial compressor, this pressure ratio takes six or seven stages.

The compressed air flows through the diffuser and reverses direction to continue to the fully annular combustion chamber. Dual orifice nozzles are used to inject fuel into the air at the dome end of the flame tube. A medium energy spark system ensures ignition of the fuel-air mixture. The ignited mixture again reverses flow and enters the single-stage high-pressure turbine that drives the impeller. From the HP turbine, the air flows through the inter-turbine duct to the LP turbine. The LP turbine consists of two stages, which drive the engine fan blades. The LP turbine section makes use of a so-called shrouded blade to increase efficiency. The HP sections are connected using a torque tube. The hollow torque tube of the HP sections allows the connection of the LP sections by another torque tube. Note that the HP sections are the impeller and the first, single-stage turbine section. The LP sections are the fan, booster stage and the two-stage shrouded turbine section. These high- and low-pressure sections are not mechanically connected, the so-called free-turbine principle, well known, and probably borrowed from the Pratt & Whitney PT6. So, in theory, it is possible to start the engine while holding the fan blades still. For the PT6 engine, the propeller can be locked, and the engine then functions as an Auxiliary Power Unit (APU).

A cross-section view of the JT15D-4, showing the engine components, can be seen in fig. 3.2 which is retrieved from the *"Pratt & Whitney Canada LTD.- JT15D Series Installation Handbook"* provided by the PH-LAB maintenance crew.

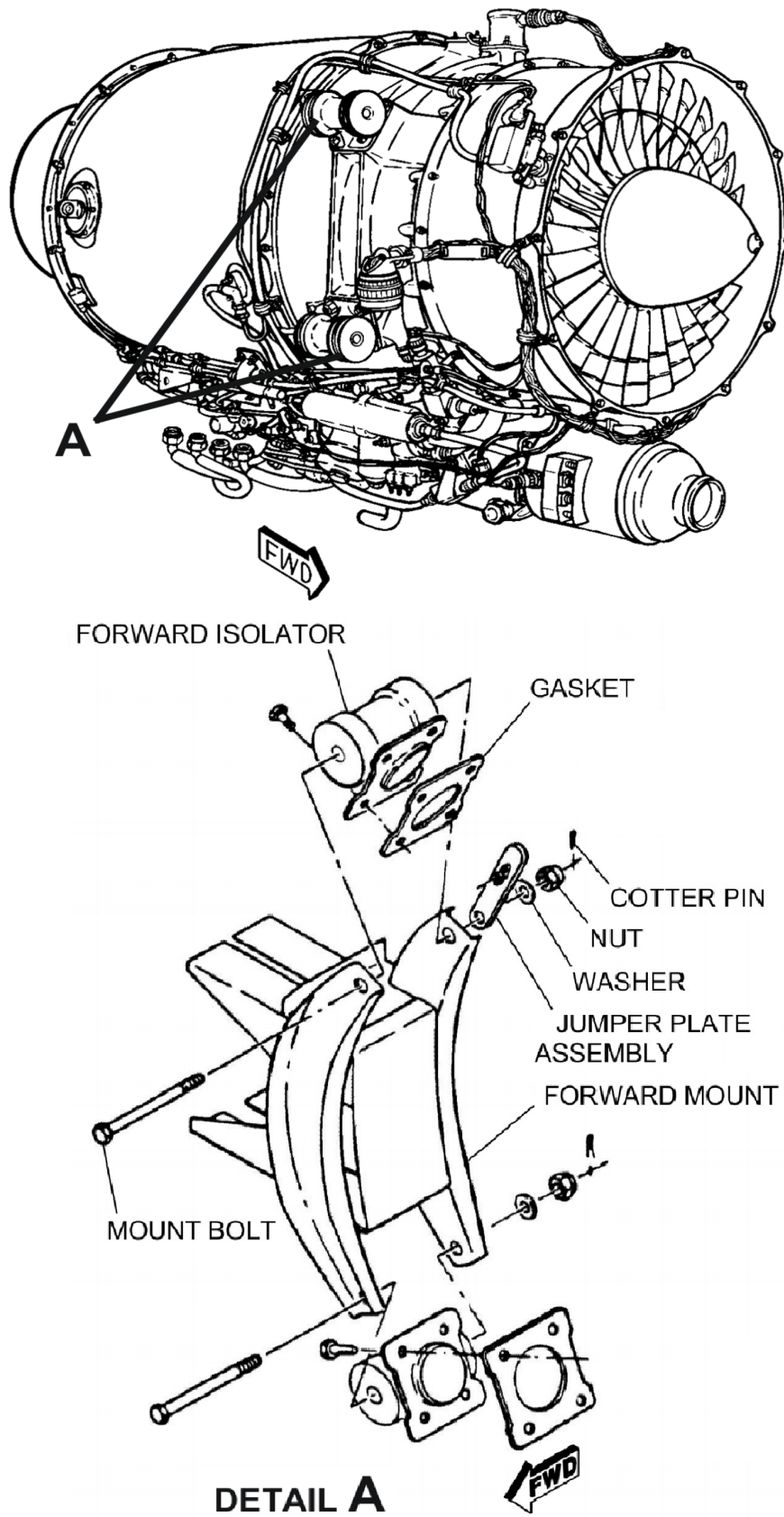


Figure 3.1: Forward engine vibration isolators of Cessna model 550 (Textron, 2020b)

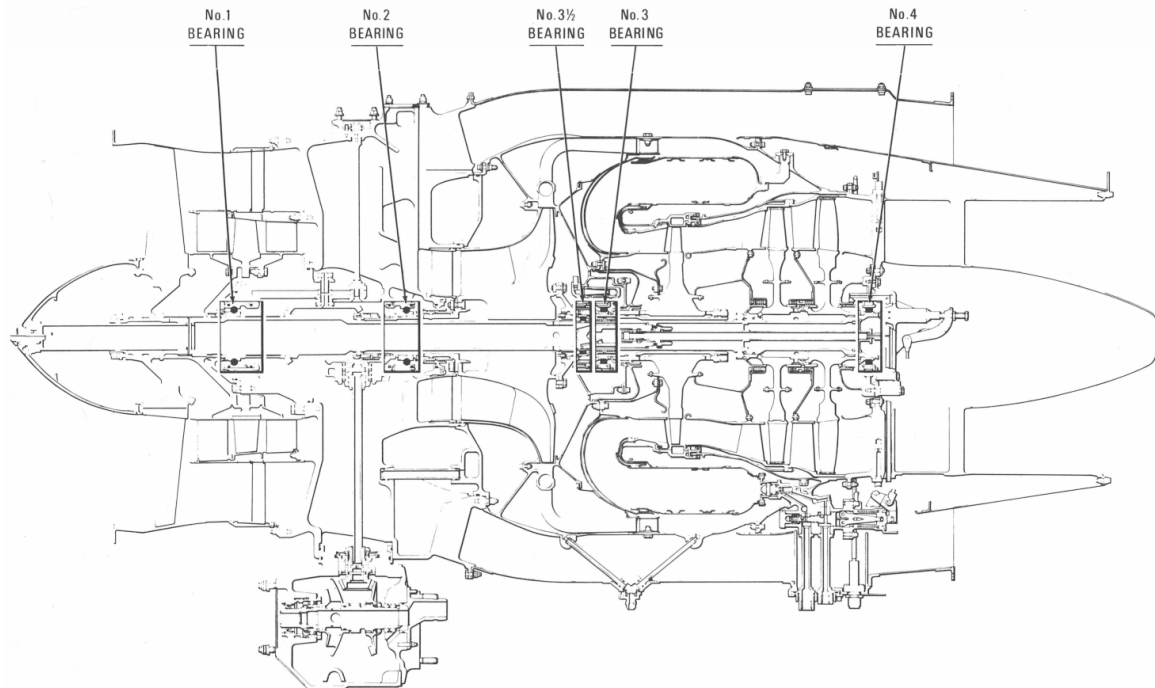


Figure 3.2: Cross-section of JT15D-4 engine (Pratt & Whitney, 1975)

3.2 Engine Vibrations

Chapter 4 discusses the independent variables regarding the vibration isolator stiffness. Two of the parameters that influence the stiffness of the vibration isolator are the frequency and amplitude of the vibration. Excellent research into the vibration characteristics of the engine in question, the Pratt & Whitney Canada JT15D-4, is performed by Botman (1980) and used as input for this section.

The engine vibrations are in general caused by the imbalance of rotating parts. These vibrations are via the bearings guided into the engine structure. The HP compressor or impeller and the HP turbine are supported by two bearings, bearing no.2 which is a ball bearing and by bearing no.3 which is a roller bearing. The impeller rotates clockwise when facing the flight direction and rotates with 31450 revolutions per minute (RPM) which is 524 revolutions per second (RPS). The LP compressor or fan and the boost stage are supported by the no.1 ball bearing. The LP turbine is mostly supported by the no.4 roller bearing and partly by the roller bearing supporting the LP torque tube. This bearing in between the two torque tubes is called the no.3 $\frac{1}{2}$ bearing. The LP sections rotate in the same direction as the HP sections and reach a maximum speed of 16540 RPM or 275 RPS. As mentioned in section 3.1, the engine is based on the free-turbine principle. This also means there is no fixed speed relation between the high- and low-sections, and is purely determined by the aerodynamics and the fuel flow in each flight situation. Each engine is unique, as each engine wears in a different pattern.

However, to give an impression of the relation between the N1 and N2, a running line is defined, as shown in fig. 3.3, where N1 represents the LP and N2 the HP speed. Again, the running line of each engine is expected to differ from the one shown, also depending on the flight conditions and engine wear.

Considering vibrations of rotating parts at different speeds, critical speeds are the most important. At a critical speed, both rotors vibrate at a frequency that corresponds to the rotation speed of the exciting rotor, while the other rotor rotates at its own rotation speed. This results in a constant deflected shape of the exciting rotor, exposing the same rotor location to possible rubbing. The excited rotor experiences continuous flexing as the vibration and rotation speed do not match. The critical speeds occur in two independent groups: the LP rotor excited modes at N1 speeds or the HP rotor excited modes at N2 speeds. Basically, what happens is that one of the rotors starts vibrating at the rotation speed of the other rotor, which causes the vibrations to couple and amplify.

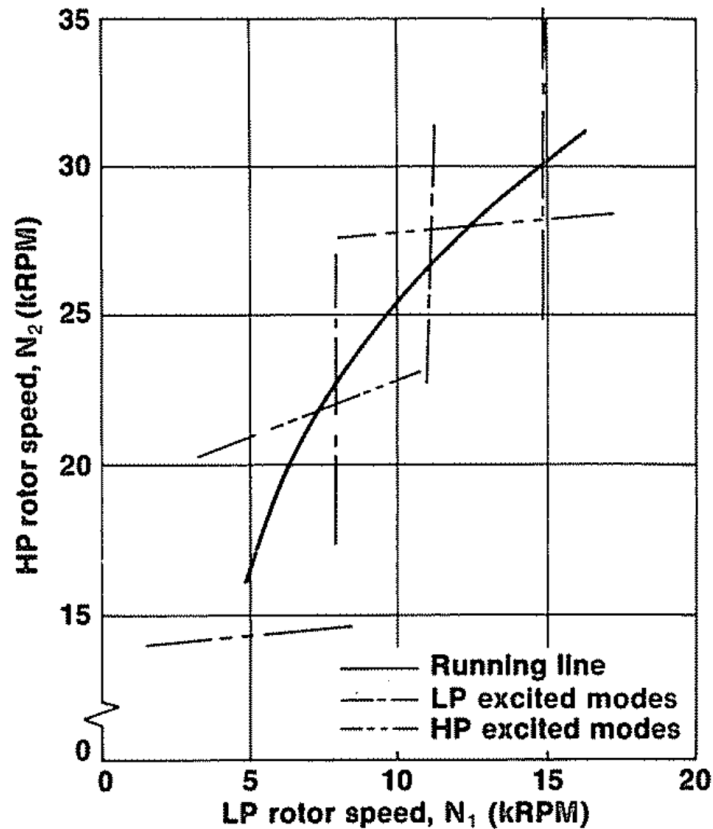


Figure 3.3: Critical speeds of JT15D-4 (Botman, 1980)

Figure 3.3 shows the mentioned critical speeds with respect to the engine running line or N_1 and N_2 speeds. Since the running line is plotted against the N_1 and N_2 speed, the points of interest are the crossing of the running line with the horizontal and vertical critical speed lines. Again, the running line and critical speed plots differ from engine to engine due to wear and geometry.

In fig. 3.3, three horizontal and three vertical lines are distinguished. Each of these lines corresponds to a critical speed or a so-called mode. The shape of the mode or the intensity distribution of the vibration mode over the engine is shown in fig. 3.4. Due to a flexible LP rotor, three modes are observed. The first mode is a bearing mode, the second mode is caused by the bending of the LP rotor, and the last mode is again a bearing mode. The first mode at 8000 RPM is caused by unbalance of the fan and is controlled by the bearing no.1 stiffness and damping. The third mode at 15000 RPM is comparable and is caused by an unbalance in the LP turbine and is controlled by the stiffness and damping of bearing no.4. The second mode at 11100 RPM is caused by an excited mode of the LP rotor, with the HP rotor pitching around a point close to the LP rotor. The second mode is controlled by the stiffness of bearing no.3. This mode is considered unimportant as this mode is not excited by any significant LP rotor mass. The damping in bearings is accomplished by utilising oil-film dampers.

Figure 3.3 shows that the HP rotor has three critical speeds, the horizontal lines. These lines are again found in fig. 3.4. For the HP rotor, a few extra modes are observed, these are well below idle speeds and will therefore not be excited for a longer period of time. The first HP mode is found at 14800 RPM and is a borderline case considering the start of the running line. The first HP excited mode shows a large response in the LP turbine area. The mode is controlled by the stiffness and damping of the no.4 bearing. The second mode is observed at 22000 RPM and is coupled with the flexible LP rotor which shows the most response at the fan side. The mode is controlled by the stiffness and damping of the no.1 bearing. The third HP rotor excited mode is observed at 27400 RPM and a rotor pitching mode which is controlled by the stiffness and damping of bearing no.2 and shows little effect in the LP rotor.

Further analysing the unbalance of major rotating components indicates that the LP rotor unbalance is mostly felt locally in the engine. So, a vibration generated by the LP turbine does in general not affect other sections that are not located close to the LP turbine. Unbalance of the fan produces large so-called

1 EN_1 responses, which is the component of the vibration frequency at N_1 speed, at the no.1 bearing at 8000 RPM. This is mainly due to the coupled modes of the HP and LP rotors. Unbalance in the LP turbine is mainly observed at the no.4 bearing at 15000 RPM. HP rotor unbalance is felt locally, though also distributes over the engine. This is mainly caused by the relatively high participation of the LP rotor. Unbalance in the impeller produces large 1 EN_2 responses at bearing no.2 at 28000 RPM. Here, 1 EN_2 responses are the vibration frequency component at N_1 speed, at the no.2 bearing.

To measure the mentioned engine vibrations, two locations are used on the engine. Both locations are at the top dead centre, with the first at the flange that separates the fan case and intermediate case. The vibration that is measured at this location gives a good indication of unbalance that result in high loads in the no.1 and no.2 bearings. The other vibration measurement location is found at the front flange of the exhaust duct. At this location, the unbalances that produce high no.4 bearing loads are detected. Standard brackets and velocity pick-ups are used. This results in an average overall velocity reading, a measure of vibration intensity at a specific frequency. The engine certification limit is set at 1.5 inch/sec while the production acceptance limit is 0.8 inch/sec in both measurement locations.

By plotting the 1 EN_1 and 1 EN_2 contents of the vibration as a function of the rotor speeds, a better interpretation of the measured vibrations is created. Figure 3.5 shows an example of such plots. Note that the order of the modes is not always distinct in the overall record. However, the speeds at which the peaks and thus modes occur, are a direct indicator for which mode is involved.

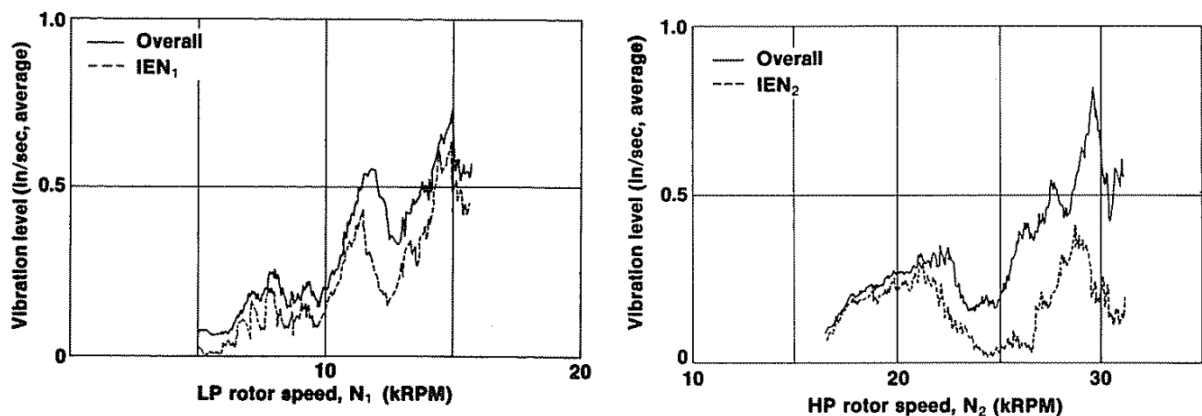


Figure 3.5: Low & high rotor excited vibrations (Botman, 1980)

3.3 Conclusion

The Pratt & Whitney JT15D-4 engine is developed for small business jets, such as the Cessna model 550. To reduce vibrations and noise, the engine thrust is lead through two vibration isolators into the aircraft structure. The high- and low-pressure engine sections rotate at two different rotation speeds, and therefore two vibration frequencies are observed. At certain rotation speeds these frequencies couple and amplify, these are called critical speeds. The largest engine vibrations are induced by unbalance in fan, impeller or turbine sections, which are local vibrations. This information is useful as the characteristics of the vibration isolator are dependent on the amplitude and frequency of the isolator, as described in the following chapter.

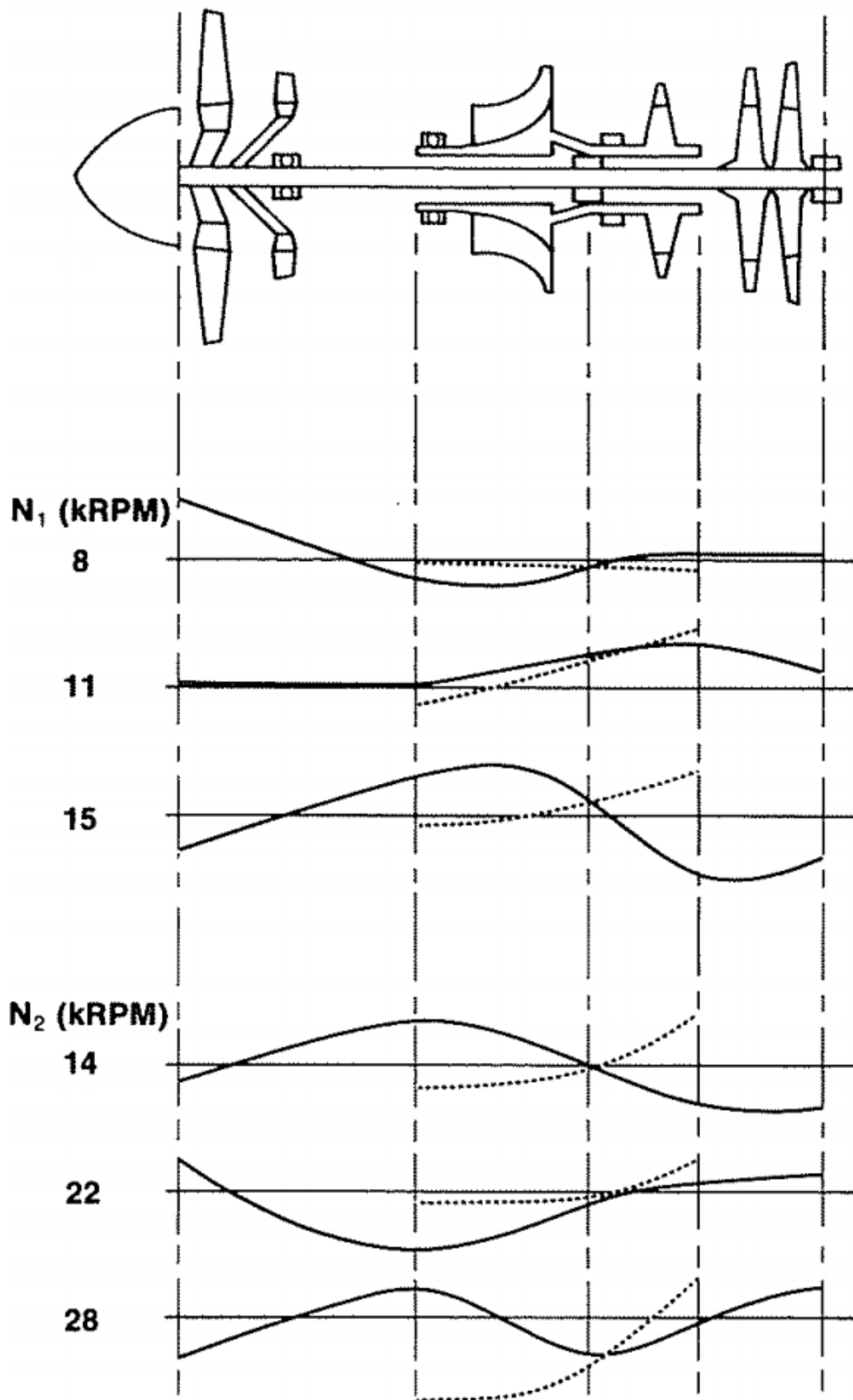


Figure 3.4: Coupled rotor modes of JT15D-4 (Botman, 1980)

Chapter 4

Aircraft Engine Vibration Isolator Characteristics

This chapter reflects on the characteristics of the vibration isolator. Rendering a model of a vibration isolator sounds trivial, yet highly non-linear behaviour is observed in vibration isolator deformation. Different aspects on the cause of the nonlinearity are discussed. Followed by detailed information on the vibration isolator of the Pratt & Whitney JT15D-4 engine.

4.1 Vibration Isolators

Vibration isolators are commonly used to isolate a receiving structure from a source of vibration. If the vibrations are in the audible frequency, the vibrations radiate sound. To increase passenger comfort and reduce structural peak loads, vibration isolators are used to connect the jet engine to the airframe.

These vibration isolators use elastomers as isolation material. Elastomeric materials embody long polymer chains that are cross-linked into loose networks, having entanglements and intramolecular loops, which enables elastomers to withstand large strains of up to several hundred percent (Kari, 2001).

Vibration isolation elastomers, such as natural rubber, neoprene, polyurethane and silicone rubber all have different properties. The key properties of elastomers are dynamic modulus and damping. The effect of strain amplitude, repeated cycling, and temperature influence these key properties (P. Wang, Su, Lai, Jiang & Wang, 2015). LORD corporations is the manufacturer of the engine vibration isolator of the Cessna Citation II and therefore the PH-LAB (LORD, 2020b). The material used in the JT15D-4 engine vibration isolators is the BTR[®]II “Broad Temperature Range” elastomer (LORD, 2020a). BTR[®]II is a silicon rubber which has according to Rivin (2003) indeed little-varying performance characteristics in rather broad temperature ranges.

The engine vibrations of the JT15D-4 are primarily due to rotor unbalances, which may produce large responses at some of the critical speeds (Botman, 1980). The maximum fan-blade rotation speed of the JT15D-4 engine is 275 RPS. The maximum N1 speed is 31450 revolutions per minute and therefore generates a vibration of maximum 525 Hz (Wrong, 1969; Cook, 1972; Ferrar, Schneck, Wicks & O’Brien, 2016).

4.2 Elastomeric Characteristics

This section describes the characteristics of elastomeric or rubber-like materials. By investigating the characteristics of elastomeric materials and by what these characteristics are influenced. Where the magnitude and the linearity of the influence are of most importance. Later on, the reviewed literature helps to explain the non-linearity of vibration isolators during experiments.

4.2.1 Viscoelastic Properties

This section captures the theory of the viscoelastic phenomenon and covers the mechanistic explanation. An ideal linear elastic solid obeys Hooke’s law: stress is proportional to strain. An ideal viscous liquid obeys Newton’s law: stress is proportional to the rate of change of strain with time (Gent, 2012). Elastomers show properties that intermediate between these two cases and are therefore called *viscoelastic*. The ratio of which the material behaves like a viscous or elastic material depends upon the rate of change in

the load. Figure 4.1 shows the stress due to a dynamically applied strain in a Hookean body, viscoelastic material and Newtonian fluid, where δ is the phase angle and E^* the complex modulus.

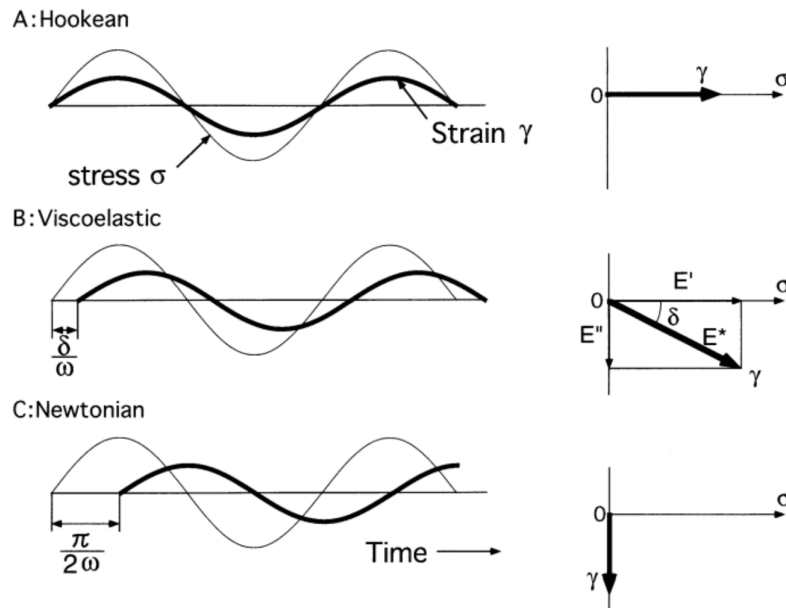


Figure 4.1: Schematic representation of the relationship between stress and strain in different materials (Murata et al., 2000)

The fact that viscoelastic material bears properties of both linear elastic and viscous material is also shown in fig. 4.2. Where (a) represents the plot of an ideal linear material, (b) represents an ideal viscous material and (c) shows a clear combination of the two aforementioned properties and, is often called a Lissajous figure (Pain, 2005).

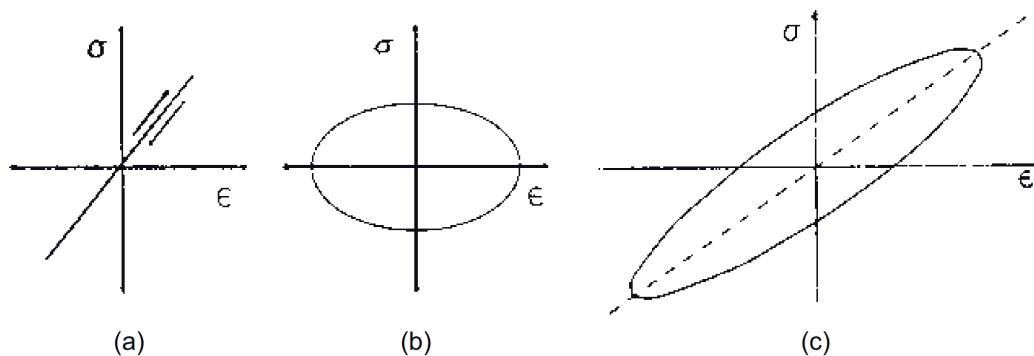


Figure 4.2: Dynamic stress-strain plot of viscous material (Gent, 2012)

4.2.2 Hysteresis

Viscoelastic materials have the property of showing a hysteresis shaped stress cycle. The stress level at a certain deformation in the loading cycle is higher than the same deformation in the unloading cycle. The difference between the loading and unloading curve represents the amount of mechanical energy that is internally dissipated. The mechanical energy is lost in viscous flows or internal breaking of bonds due to stresses. This behaviour is desirable for vibration isolators, as this magnitude of the effect defines the damping. In a cyclic loading, two lines are distinguished, the loading path and the unloading path. The surface under the loading curve represents the energy stored in the system, while the surface under the unloading curve represents the energy that is released by the system. The surface between the two lines represents the amount of dissipated energy, which is normally transformed into heat (Z. Wang, Golob &

Chesler, 2016). A relation between the maximum stored energy and the dissipated energy provides an indication of the damping characteristics δ of the material and are found in eq. (4.1).

$$\frac{\text{Dissipated energy}}{\text{Max stored energy}} = 2\pi \tan\delta \quad (4.1)$$

The δ which is found in eq. (4.1) is the same δ as described in section 4.2.1, however, represented in a different way. The larger the energy dissipation, the better the damping characteristics of the material. The hysteresis effect is seen in the static deformation cycle of the JT15D-4 vibration isolator which is shown in fig. 4.3 and was provided by Textron Aviation.

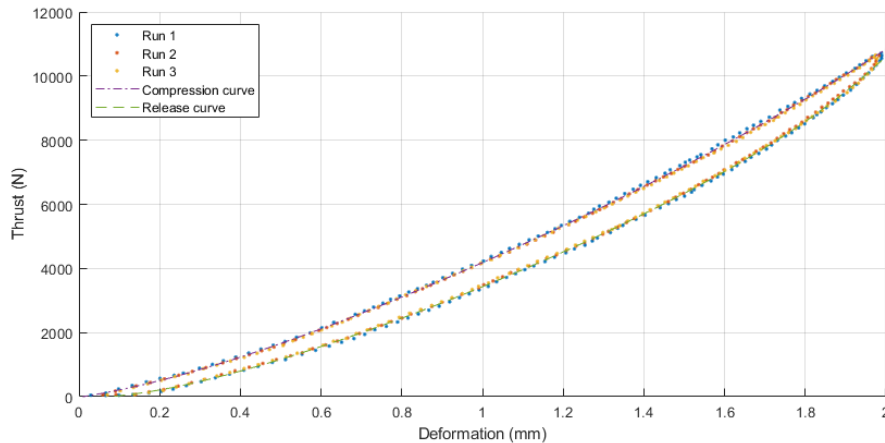


Figure 4.3: Static deformation of the JT15D-4 vibration isolator

4.2.3 Stiffness Effects

The stiffness or spring rate of viscoelastic material is influenced by several factors. Some of which are dynamic, others are static. The important factors are presented as follows:

Static effects

- Creep
- Stress relaxation
- Temperature

Dynamic effects

- Wave effect
- Pre-strain
- Payne effect
- Mullins effect

Here dynamic is considered an input with a sinusoidal shape and static a constant input. The output of the static input system is still dynamic as it evolves over time, except the temperature.

Creep

The gradual increase of deformation while the load remains constant is called creep. For a vibration isolator, this is normally due to the weight of the engine. The formula that describes the characteristics of creep is given in eq. (4.2) (Rivin, 2003).

$$\Delta' = \Delta + b \log t \quad (4.2)$$

Where Δ is the relative deformation of the element at one minute after the load is applied. And b is a constant that characterises the creep rate. Creep is expressed as a percentage increase over a given

period of time. For the research experiments, creep might have an influence during cruise flight, where a constant thrust force is exerted on the vibration isolator.

Stress Relaxation

The decrease of stress with a constant strain over a period of time is called stress relaxation. This is comparable to creep, however, this time the strain is constant with decreasing stress instead of constant stress with increasing strain. The constant strain that acts on the isolator decreases the stress exponentially over time and settles at σ_∞ . Stress relaxation is not expected to influence the experiments in this research. This is due to the fact that constant stress is imposed by the weight, which leads to creep.

Temperature

The internal viscosity between the molecular chains of the viscoelastic material causes the delayed elastic response. Temperature strongly affects this property. This dependence is mainly determined by the rate φ at which small parts of the molecule move into the new position, which is the result of the random Brownian motion. An increase in temperature causes a large increase of φ . This results in a lower internal viscosity, energy dissipation and therefore lower damping at increased temperatures. The relation between temperature and φ was found by Williams, Landel and Ferry (1955) and follows a characteristic law:

$$\ln \left[\frac{\varphi(T)}{\varphi(T_g)} \right] = \frac{A(T - T_g)}{(B + T - T_g)} \quad (4.3)$$

Where A and B are constants for a wide range of elastomers with values of 40 and 50 °C. The reference temperature at which the molecules practically stop moving, and the material becomes a rigid glass is called T_g or glass transition temperature. A more general use of Equation (4.3) is relating the dynamic behaviour at one temperature T_1 to another temperature T_2 . Properties like the dynamic modulus E_1 and loss factor $\tan \delta$ are dependent on the frequency of the vibration. Jones (2001) states that qualitatively, the effect of frequency is the inverse of the effect of temperature, increasing frequency being similar to the effect of decreasing temperature, but at much different rates. Figure 4.4 shows an example of the mentioned dynamic properties.

Here, the time or frequency axis is on a logarithmic scale, which results in a lateral displacement of the curves if the temperature is changed. This relationship goes under different names and varies from terminological simplicity, the time-temperature superposition principle (often confused with the Boltzmann superposition principle) to time-temperature reducibility (Ferry, 1980; Tanner, 2000). The magnitude of displacement, $\ln a_T$, on the frequency axis is given by eq. (4.4).

$$\ln a_T = \frac{\ln [\varphi(T_2) / \varphi(T_1)] \times 40 \times 52 (T_2 - T_1)}{(52 + T_2 - T_g) (52 + T_1 - T_g)} \quad (4.4)$$

This formula provides a powerful time-temperature, frequency-temperature, and rate-temperature equivalence principle that enables the user to correlate mechanical behaviour over wide ranges of time, frequency, and rate with temperature, so-called master curves (Gent, 2012).

Mullins Effect

The Mullins effect or also called stress-softening was apparently first studied by Holt (1932) and later by Mullins (1949). Bueche (1961) developed a molecular theory for the softening and Harwood, Mullins and Payne (1965) extended the research to different materials. The Mullins effect describes the pronounced softening of the viscoelastic material after prior straining. The softening increases with larger imposed strain. The effect over several cycles is shown in fig. 4.5. For the research experiments, the Mullins effect only requires attention for new vibration isolators.

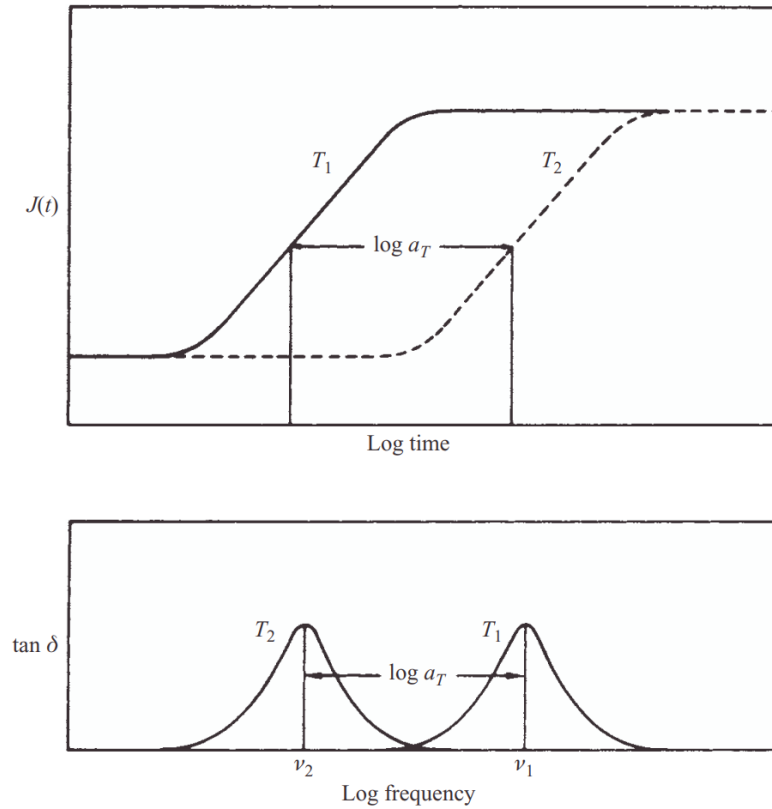


Figure 4.4: Schematic diagrams illustrating the simplest form of time-temperature equivalence (Ward & Sweeney, 2004)

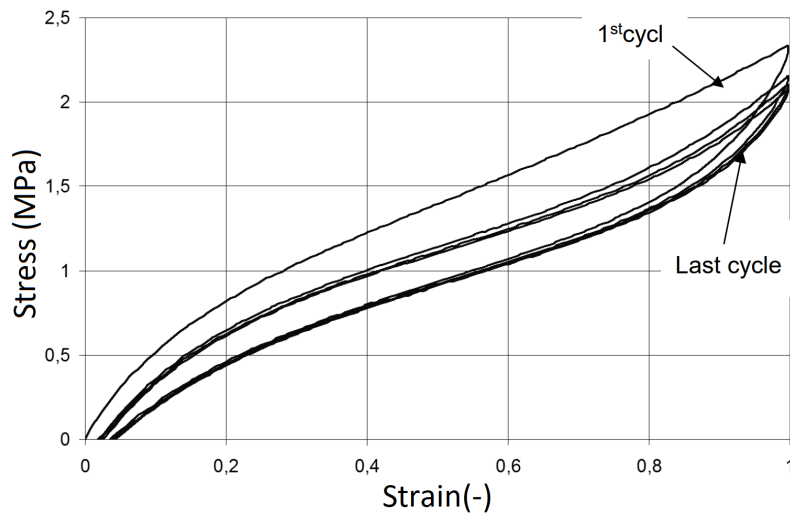


Figure 4.5: Stress-strain plot of viscous material showing Mullins effect (Laka, 2016)

The Mullins effect can also be observed in the radial deformation cycle data in fig. 4.6 which is provided by Textron Aviation. Here, the first cycle requires a slightly higher load compared to the second and third cycle.

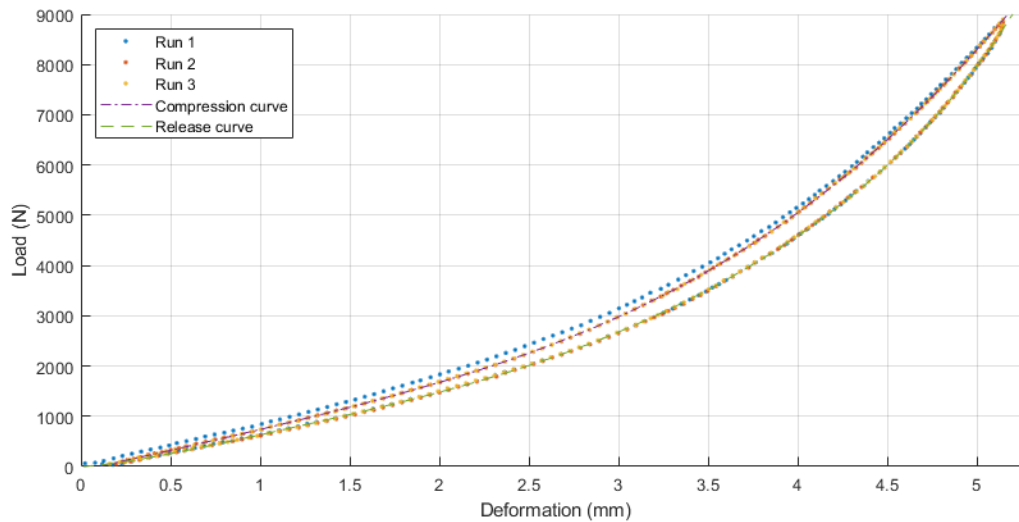


Figure 4.6: Radial deformation characteristics of the JT15-4 vibration isolator

Payne Effect

The Payne effect, or sometimes called the Fletcher-Gent effect, appears when viscoelastic materials are loaded in a cyclical fashion at different vibration amplitudes. This causes the dynamic stiffness of viscoelastic material to decrease as the vibration amplitude increases (Payne, Whittaker & Smith, 1972). The focus of this research lies on high-frequency excitation which has low vibration amplitudes and therefore no large influence of the Payne effect is expected.

Wave Effect

At higher frequencies resonances can occur in vibration isolators, these change the stiffness characteristics drastically in a specific frequency region (Vahdati & Saunders, 2002). For vibration isolators, it is highly undesirable to have resonance to occur in the operation range (Harrison, Sykes & Martin, 1952; Snowdon, 1980). Therefore, no wave effects or resonances are expected in the operation range of the engine vibration isolator.

Biaxial Effect

The engine vibration isolator of an aircraft is loaded in different directions and in different forms. A few forms of loading are weight, radial vibration, and axial thrust force. These different loads affect the stiffness of the vibration isolator material in different ways, or is a biaxial influence. Lakes (1999) discusses several experimental setups that test the influence of excitations in different axis. The cross-coupling of stiffness behaviour in vibration isolators is later researched by Kari (2001, 2003) and found a similar result. This indicates that vibrations in the radial direction influence the stiffness in the axial direction, and that engine rotation vibrations influence the axial isolator stiffness.

4.2.4 Material Ageing

Elastomers are traditionally designed for use in applications that require specific mechanical properties. Unfortunately, these properties change with respect to many different variables including heat, light, fatigue, oxygen, ozone, and the catalytic effects of trace elements (Gruenberg, Blough, Kowalski & Pistana, 2001). Hence, vibration isolators are subjected to ageing and deterioration of the material properties. As ageing is per definition a function of time, the influence of ageing in this research is expected to be negligible provided that the time between model generation and use is small.

4.3 Engine Isolator Specifications

The Cessna model 550 utilises three vibration isolators, one rear and two front isolators of which one is the upper isolator, and one is the lower isolator. The isolators are manufactured by Lord Corp. and are

required to fulfil certain specifications that are imposed by Pratt & Whitney Canada Inc. and Cessna, now Textron Aviation. The specifications for the manufacturer were provided for this research by Mr. Martens, the technical representative of Textron Aviation.

4.3.1 Spring Rates

The spring rate of a material provides an indication of the force that is required to achieve a certain deformation. Often, spring rate is interchangeably used with *modulus* or *stiffness*. As discussed in section 4.2.3 is the stiffness of a viscoelastic material influenced by the vibration frequency. This results in so-called static and dynamic spring rates. A clear difference in the slope, and thus the spring rate due to vibration, which is shown in fig. 4.7.

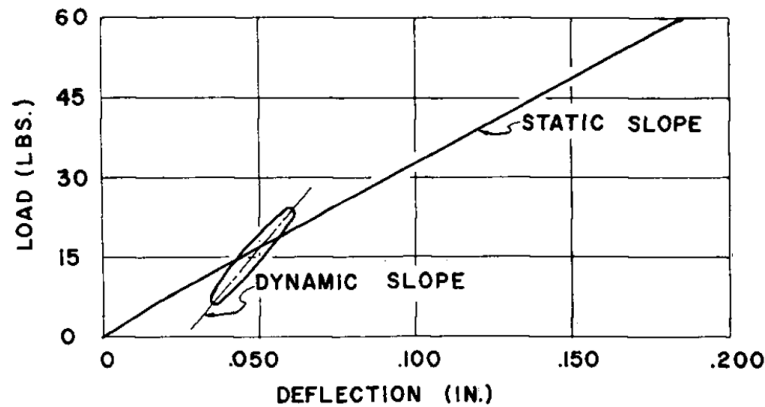


Figure 4.7: Static and dynamic representation of spring rate (Larsen, 1966)

The specification sheet of the engine vibration isolators for the Cessna model 550 gives the spring rates of each isolator, both static and dynamic. The dynamic measurements are performed at a 20Hz input vibration. The spring rates for the static condition are given in table 4.1. The spring rates for the dynamic test case are given in table 4.2.

Mount Position	Fore & Aft (N/mm)	Lateral (N/mm)	Vertical (N/mm)
Front Upper	5079	1646	1646
Front Lower	5954	1926	1926
Rear	0	875	875

Table 4.1: The vibration isolator static spring rates at normal room temperature

Mount Position	Fore & Aft (N/mm)	Lateral (N/mm)	Vertical (N/mm)
Front Upper	6480	2980	2980
Front Lower	7355	4553	4553
Rear	0	1664	1664

Table 4.2: The vibration isolator dynamic spring rate for normal cruise conditions based on test data at 20Hz at normal room temperature

As discussed in section 4.2.3, the stiffness of the elastomer is dependent on the temperature. The specification sheet for the vibration isolator states that the decrease in temperature should have a limited increase in stiffness or spring rate. The limits for the increases in dynamic stiffness of table 4.2 are stated in table 4.3, where the temperatures are based on the expected operating temperatures of the vibration isolators. The higher temperature of the front isolators is explained by the fact that the bleed air tubes are routed relatively close to the isolators and reach temperatures up to 380°C according to the installation handbook. Besides the bleed air tubes, does the engine oil also heat up the isolators. This is because the

engine oil is stored in the engine casing, on which the vibration isolators are mounted. The fact that this engine cools the oil behind the oil pump and then uses the oil to cool and lubricate the bearings, means that the hot oil from the bearings flows back into the oil reservoir, a so-called *hot reservoir system*.

Mount	Temperature (° C)	Max. Increase (%)
Front	-7	30
Rear	-37	70

Table 4.3: Increase of spring rate due to temperature decrease

4.3.2 Isolator Loading

The preload on the vibration isolators influences the spring rate or stiffness of the elastomer material. In static conditions, this preload is defined by the mass of the engine, which is 822 pounds (373 kg) for an installed engine according to the vibration isolator specification sheet. This same document provides information about the location of the centre of gravity. With this information, an estimate for the preloads per isolator can be calculated.

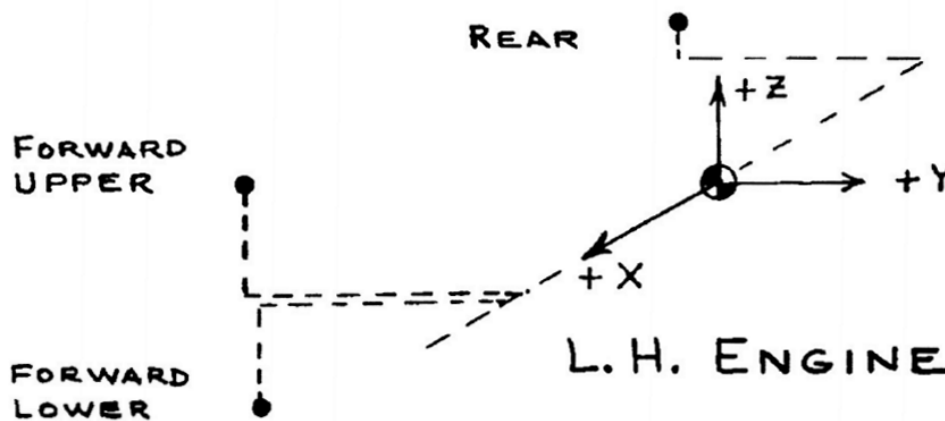


Figure 4.8: Engine vibration isolator positions with respect to the centre of gravity

A schematic representation of the location of the vibration isolators with respect to the centre of gravity (CG) is given in fig. 4.8. The exact positions of the vibration isolators are given in table 4.4.

Axis	Upper (mm)	Lower (mm)	Rear (mm)
x	263.9	276.1	-390.1
y	-289.1	-263.1	-367.5
z	235.5	-109.0	33.5

Table 4.4: Engine vibration isolator positions with respect to the centre of gravity of the engine

By observing the geometry, the two front mounts are located at approximately the same distance forward of the CG. Assuming the engine is a rigid body, and the load is evenly distributed by the distance to the CG, a simple calculation estimates the load on the front and rear vibration isolators. The calculations are shown in eqs. (4.5) and (4.6).

$$\begin{aligned}
 F_{z\ fwd} &= \text{Engine weight} \cdot \frac{\text{length rear}}{\text{total length}} \\
 &= -3658(N) \cdot \frac{390.1}{270 + 390.1} \\
 &= -2162(N)
 \end{aligned}
 \tag{4.5}$$

4.4 Conclusion

The vibration isolators that are used for the Cessna model 550, consist out of silicone rubber and metal. Silicone rubber is a viscoelastic material and has relative little-varying mechanical properties over a large temperature range, which is beneficial for aircraft engine vibration isolators. Rubber-like materials show viscoelastic properties, resulting in shifted stress-strain graphs. And due to the energy dissipating in the material, the stress cycle shows a hysteresis shape. The stiffness of viscoelastic material is influenced by the temperature, preload, frequency and amplitude of the input vibration. The Mullins, Payne, wave, and biaxial effect also influence the stiffness of the vibration isolator, where the Mullins, and biaxial effect are expected to have the largest influence in this experiment. The Temperature, preload and vibration frequency and amplitude are the independent variables of the research, with the stiffness or spring rate the dependent variable. The static and a dynamic spring rates are provided by Textron Aviation and provide an indication of the magnitude of these values. A preliminary calculation of the mount loading gives an indication of the vibration isolator preloads.

Chapter 5

Experiment Setup

The proposed method of determining the jet engine thrust by measuring the vibration isolator deformation requires a mathematical model of the isolator. In general, material properties like the loss factor or spring rate are key values to develop a mathematical model of an isolator. This time however, an isolator is given and the CAD models or exact material properties are not provided by the manufacturer. This prevents the use of purely numerical models and requires models that are based on experimentally obtained data.

This data is generated by performing deflection measurements under different controlled environments and inputs. These measurements are performed in an experiment setup that simulates the conditions a vibration isolator experiences during flight. This chapter provides an overview of the possible experiment setups and the according benefits or downsides. The experimental setup contains several parts: test machine, test frame, test object. Where the *test machine* is used to generate vibrations and measures the response of the isolator to construct a dynamic model. The *test frame* is basically an adaptor that ensures comparable measurements on the test machine and aircraft. The *test object* is in this case a vibration isolator for the Pratt & Whitney Canada Inc. JT15D-4, which is used on the PH-LAB, a Cessna model 550.

5.1 Test Machine

For testing elastomeric vibration isolators, the dynamic properties are of most importance. Therefore, a test setup that generates/simulates vibrations is required. Where the magnitude and frequency range of the equipment are required to simulate the vibration frequency and amplitude of an operating Pratt & Whitney JT15D-4 jet engine.

These experiments are in general performed in fatigue test benches or specially produced *rubber vibration isolator test benches*, which are technically fatigue test benches optimised for viscoelastic materials. The more expensive versions of these optimised test machines include a temperature-controlled test environment. Research performed with a conventional test machine is for example Sjöberg and Kari (2002). A wider variety of these conventional test setups are shown in Ibrahim (2008)

The aircraft hall at the TU Delft facilitates the structures & materials research department that possesses a dedicated elastomer testing machine. The test machine in question is an MTS-831 elastomer test system with a maximum frequency of 550 Hz and an option for thermal manipulation.

An alternative option to determining the dynamic stiffness characteristics is developed in recent years. The approach of this method is completely different as the system, or in this research, a vibration isolator is excited with a pulse hammer, after which the response is measured with accelerometers. These measurements provide enough information to model the characteristics into the kHz range, where conventional machines are limited to about 900Hz due to eigenfrequencies (Haeussler, Klaassen & Rixen, 2020). Other important research in the field of multidimensional vibration isolator identification is performed by Kim and Singh (2001); Lin, Farag and Pan (2005); Ooi and Ripin (2011). The downside of this method is that the accelerations measured on the isolator do not represent the vibrations measured in flight and therefore are not comparable to the aircraft installation. Therefore, this method is not used for the research experiments.

The test machine of the TU Delft aircraft hall is equipped with several software packages for different purposes. Due to the fact that the testing procedure is not a straightforward measurement of force and deflection, special software packages are developed that are optimised to perform a certain test. Examples

of specific test software are static characterisation, dynamic characterisation and resonance search packages. An example of a typical static characterisation process flow is found in fig. 5.1¹.

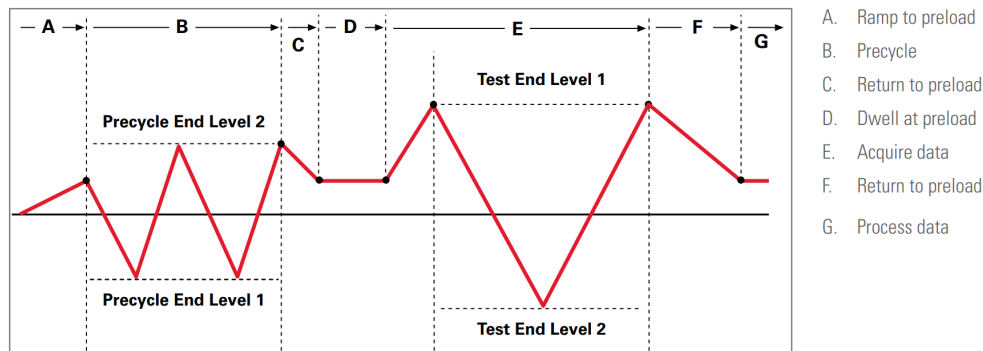


Figure 5.1: Static deflection process graph

The process of dynamic characterisation is a dedicated software for this purpose. The dynamic characterisation is performed by using frequency sweep vibration inputs. This frequency-based approach results in a model that excludes the transient response of the vibration isolator. However, it is expected that the transient response of the vibration is an order of magnitude faster than the transient response of the engine and would not influence the outcome of the research. The dynamic characterisation software includes a package for temperature control, which can be used to generate a master curve as discussed in section 4.2.3. The test machine is able to generate pulse, step and sinusoidal vibration signals, where this experiment uses sinusoidal wave signals to simulate the engine rotor.

5.2 Test Frame

For the measured data to be comparable between tests, test setups or aircraft, the sensors are required to be installed in the same position with respect to the vibration isolator. To achieve this, a test frame is connected to the vibration isolator. Several construction possibilities are considered with the PH-LAB crew, including using the flange or the unused oil filler tube. These however, are not available during testing in the experiment setup. The best option is to use the same bolts on which the vibration isolator is mounted to the engine. The vibration isolator mounting bolts are currently NAS566-35, the next length is -37 and creates 3.175 mm to mount a test frame. Figure 5.2 shows these bolts and a general impression of the engine mount. Also, the previously discussed bleed air tubes are seen in the lower part of the picture.

By utilising two or four bolts for mounting a frame, a comparable measurement setup is created for both flight and test bench. The sensor that is installed on this frame is for the deformation measurement. The accelerometers are most likely installed directly onto the vibration isolator with adhesive. This, to get a direct as possible reading of the vibrations. This is of less importance for the deformation sensor, as minimal vibrations are expected in forward direction.

5.3 Test Object

The test object for this experiment is an engine vibration isolator that is used to impede vibration transmission to the Cessna model 550 aircraft. A total of three vibration isolators are installed per engine, two front and one rear. The front isolators have different dynamic characteristics and therefore also different part numbers. The part numbers for the upper and lower isolator are 9912172-8 and 9912172-9 respectively. For this research, only one isolator is sufficient to determine if the dynamic characteristics are sufficient for the purpose of measuring thrust.

¹Retrieved from https://test.mts.com/-/media/ground_vehicles/pdfs/brochures/100-168-661c_elastomerepress.pdf?as=1 on 14-Dec-2020



Figure 5.2: Lower engine mount of PH-LAB engine 2

5.4 Sensors

The required sensors are divided into two parts, of which the first is the *test machine* and the second is the *test frame*. Where the test machine is either the conventional machine or the new impulse method. In case a conventional test machine is used, all the sensors and vibration generators are embedded into the machine. Therefore, only one triaxial accelerometer and one deformation sensor is required for validation on the vibration isolator and test frame respectively. In case the impulse test method is used to model the dynamic behaviour of the vibration isolator, the instruments and sensors are provided in the test kit as it is not a test machine. Note that for this test method, the preloads still need to be applied externally. This results in a required mounting frame where the test object is preloaded in a forward and radial direction. Applying the preloads is best done by installing hydraulic cylinders. To have an indication of what load is applied in what direction, two load cells are required.

The triaxial accelerometer and linear deformation sensor are required for the test frame/adaptor and are therefore already considered. For the triaxial accelerometer, it counts that the minimum sampling frequency is at least twice the highest expected excitement frequency, the so-called Nyquist frequency (Oppenheim, Willsky & Nawab, 1997, p. 519). The highest expected frequency is 525 Hz and therefore the minimum sampling frequency is 1050 Hz. The maximum expected acceleration is 6.7g and is based on the vibration intensity of the production acceptance limit which is 0.8 inch/sec (IPS) at the highest rotation frequency of 525 RPM as found in section 3.2. The measurement range for the acceleration is therefore set to a minimum of 0.5g and a maximum of 10g. The minimum accuracy has a large influence on the cost price of the sensor and is therefore set to 0.02g. The requirements for the displacement sensor are heat and vibration resistance. Two sensor technologies are considered, namely, the linear variable differential transformer (LVDT) sensor and the laser time of flight (ToF) sensor. Where the LVDT sensor is better heat and vibration resistant, does the laser sensor not require contact with the test object. Comparable accuracy levels are achieved, although the LVDT is the cheaper option for comparable accuracy. The requirements for either sensor include a minimum stroke, accuracy and bandwidth. The maximum expected deformation of the vibration isolator is 2 mm, therefore, a 5 mm stroke is considered sufficient. In order to get the accuracy of the thrust measurement below 50 N, a sensor accuracy of at least 15 μm is required. The bandwidth of the linear displacement sensor is of less importance since the vibrations are in a different plane. Therefore, a bandwidth of 200 Hz is expected to suffice for this purpose.

5.5 Conclusion

In order to relate the measured deflection to the thrust force, a mathematical model of the isolator is required. This model accounts for temperature, preload and vibration characteristics. The exact vibration isolator material properties and dimensions are not known, which prevents us from using a purely numerical approach and requires a model which is based on experimentally obtained data.

The fatigue test bench approach is best suited for this research. This is mainly to simulate the engine installation as accurately as possible and to maintain comparability between the data obtained in the test machine and the aircraft. The test frame can best be mounted with the bolts that mount the vibration isolator to the engine. This ensures the exact same installation position on both the test bench and aircraft. The test object is a vibration isolator of the Cessna model 550 aircraft. The sensors which are installed on the test frame are used to relate the test bench results to the aircraft measurements. The requirement for the linear displacement sensor is high temperature and vibration resistance, and for the triaxial accelerometer counts that the lowest sample frequency is 1050 Hz.

Chapter 6

Model Construction

This chapter elaborates on the different approaches to construct a model of the test object. A common approach to model elastomeric objects is defining the material properties using Dynamic Mechanical Analysis (DMA) in combination with the object geometry, which is the basis for a Finite Element Analysis (FEA) approach as described by Menard and Menard (2020); Sjöberg and Kari (2003); Sepe (1998). For this research however, the interest is only a small, very specific part of the elastomeric characteristics. Namely, the influence of certain parameters on the deflection caused by the thrust force. For the broad understanding of mathematical models of viscoelastic material, a section on conventional viscoelastic models is included. This is followed by a section on linear regression models, which is intended to be used for modelling the thrust force.

6.1 Physical Models

As mentioned in section 4.2.1, rubber-like materials bear properties of both viscous liquids and elastic solids. Where ideal viscous liquids obey Newton's law and ideal linear elastic solids obey Hooke's law. Viscous liquids are modelled with a dashpot and elastic solids with a spring. Hence, viscoelastic material can be modelled with a combination of dashpots and springs, and is called physical modelling. Placing a dashpot and spring in series is called the Maxwell model, and in parallel, it is called the Voigt model or Voigt model (Brinson & Brinson, 2015). The Maxwell model is used to model viscoelastic liquids, and the Voigt model is used to model viscoelastic solids, as shown in fig. 6.1. The Voigt model predicts creep more realistically than the Maxwell model as the strain approaches a constant in infinite time. The Maxwell model predicts stress relaxation more realistically compared to the Voigt model (Lakes, 1999, p. 24).

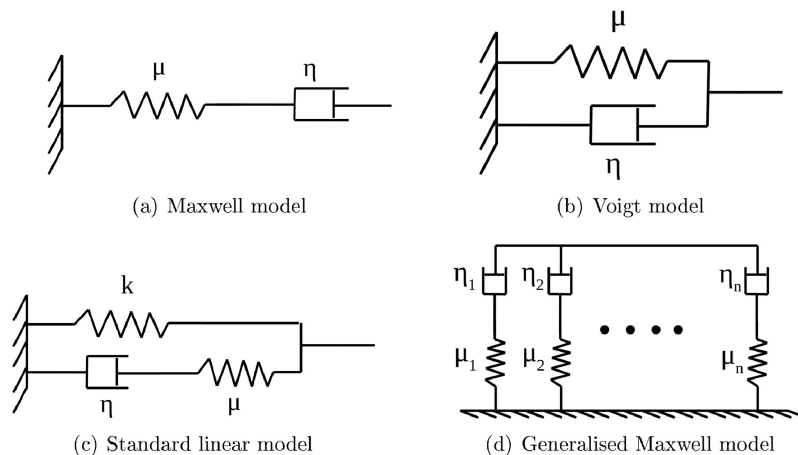


Figure 6.1: Static and dynamic representation of spring rate (Mukhopadhyay et al., 2019)

Expanding the Maxwell or Voigt model leads to a three-element model or a so-called Standard linear solid (SLS) or Zener model. Experimental evidence shows a distribution of relaxation times that are discrete or continuous. Therefore, models that are based on experimental data use multiple Maxwell models in parallel to reduce the model error. This is also called the Generalised Maxwell Model (GMM) (Riande,

Díaz-Calleja, Prolongo, Masegosa & Salom, 2000). The negative effect of adding more Maxwell models together is the resulting more complex model with more parameters to fit or estimate.

6.1.1 Maxwell Model

One of the simplest methods to describing the behaviour of viscoelastic material is the Maxwell model. The model consists of a spring with modulus E , and a dashpot with viscosity η , which are placed in series. This Maxwell element describes a first order differential equation of the stress and strain. The representation of the Maxwell model is shown in fig. 6.2 and the general solution is given in eq. (6.1).



Figure 6.2: Maxwell model (Schreurs, 2012)

$$\epsilon = \epsilon_E + \epsilon_\eta \quad \rightarrow \quad \dot{\epsilon} = \dot{\epsilon}_E + \dot{\epsilon}_\eta = \frac{\dot{\sigma}}{E} + \frac{\sigma}{\eta} \quad (6.1)$$

For step excitations of stress and strain, the differential equation of the Maxwell model are solved as shown in eq. (6.2). Here, the Heaviside function $H(t, 0)$ and creep function $D(t)$ are implemented.

$$\begin{aligned} \text{stress step} & : \quad \sigma(t) = \sigma_0 H(t, 0) \quad \rightarrow \quad \dot{\sigma}(t) = \sigma_0 \delta(t, 0) \quad \rightarrow \quad \text{creep} \\ & \quad \dot{\epsilon}(t) = \frac{\sigma_0}{E} \delta(t, 0) + \frac{\sigma_0}{\eta} \\ & \quad \epsilon(t) = \frac{\sigma_0}{E} H(t, 0) + \frac{\sigma_0}{\eta} t = \sigma_0 \left[\frac{1}{\eta} \left(t + \frac{\eta}{E} \right) \right] = \sigma_0 D(t) \\ \text{strain step} & : \quad \epsilon(t) = \epsilon_0 H(t, 0) \quad \rightarrow \quad \dot{\epsilon}(t) = \epsilon_0 \delta(t, 0) \quad \rightarrow \quad \text{relaxation} \\ & \quad \sigma(t) = \epsilon_0 E e^{-\frac{E}{\eta} t} = \epsilon_0 E e^{-\frac{t}{\tau_m}} = \epsilon_0 E(t) \end{aligned} \quad (6.2)$$

6.1.2 Voigt model

The Voigt model contains the same components as the Maxwell model, yet ordered in a parallel construction, as shown in fig. 6.3. The Voigt model is sometimes referred to as the Kelvin-Voigt model (Brinson & Brinson, 2015).

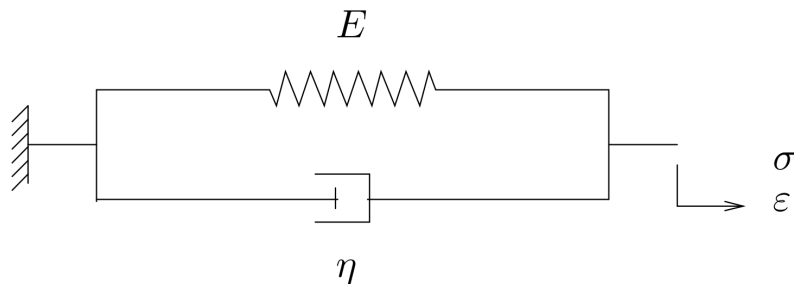


Figure 6.3: Voigt model (Schreurs, 2012)

$$\sigma = \sigma_E + \sigma_\eta = E\epsilon + \eta\dot{\epsilon} \quad (6.3)$$

As mentioned, the Voigt model is a viscoelastic solid model, meaning that the strain response to a step excitation of stress describes viscoelastic behaviour, characterised by the time constant $\tau = \frac{\eta}{E}$ [s].

$$\sigma(t) = \sigma_0 H(t, 0) \quad \rightarrow \quad \dot{\sigma}(t) = \sigma_0 \delta(t, 0) \quad \rightarrow \quad \text{creep} \quad (6.4)$$

$$\left. \begin{aligned} \eta \dot{\varepsilon}(t) + E\varepsilon(t) &= \sigma(t) = \sigma_0 H(t, 0) \\ \varepsilon(t) &= \varepsilon_H(t) + \varepsilon_P = C e^{-\frac{E}{\eta}t} + \frac{\sigma_0}{E} \\ \varepsilon(t=0) &= 0 \end{aligned} \right\} \rightarrow C = -\frac{\sigma_0}{E} \quad (6.5)$$

$$\varepsilon(t) = \frac{\sigma_0}{E} \left[1 - e^{-\frac{E}{\eta}t} \right] = \sigma_0 D(t)$$

A stepwise strain excitation leads to infinite stress.

$$\begin{aligned} \varepsilon(t) &= \varepsilon_0 H(t, 0) \quad \rightarrow \quad \dot{\varepsilon}(t) = \varepsilon_0 \delta(t, 0) \quad \rightarrow \quad \text{relaxation} \\ \sigma(t) &= E\varepsilon(t) + \eta \dot{\varepsilon}(t) \\ \sigma(t) &= E\varepsilon_0 + \eta \varepsilon_0 \delta(t, 0) = \varepsilon_0 [E + \eta \delta(t, 0)] = \infty \end{aligned} \quad (6.6)$$

The Maxwell and Voigt models are the basis for a large group of models that add components to approach a certain type of elastomer more accurately. The addition of friction components enable the simulation of hysteresis as described by Lion (1997). With the generalised models, a larger quantity of Maxwell or Voigt models are placed in parallel or series respectively. By using parameter estimation, the generalised model is fitted to the measurement data (Baz, 2019). Note that these models only include one dimension and are only capable to model one particular aspect of viscoelastic materials. Therefore, a more suitable approach to model the magnitude of the influence of independent variables on the dependent variable is discussed in the following section.

6.2 Linear Regression Model

For the measurements that are performed in the test setup, the main interest is to model the influence of certain parameters such as temperature, frequency or amplitude on the vibration isolator deflection caused by the thrust force. This with the assumption the behaviour is approachable with a linear regression model.

The estimation of parameters is performed by a cost function that are optimised for various estimators. Three different models for the uncertainties in θ and v are considered, namely:

- Bayesian model:
 - 1) θ is a vector of random variables with probability density $p(\theta)$.
 - 2) v is a random vector with probability density $p(v)$.
- Fisher model:
 - 1) θ is a vector of unknown constant parameters.
 - 2) v is a random vector with probability density $p(v)$.
- Least-squares model:
 - 1) θ is a vector of unknown constant parameters.
 - 2) v is a random vector of measurement noise.

For the Bayesian model, the probability densities $p(\theta)$ and $p(v)$ are assumed to be known a priori. The conditional density of parameter vector θ , given the observation z , designated by $p(\theta | z)$, is sometimes called the a posteriori probability density.

An estimator for the Fisher model is based on the estimation theory, using the concept of a likelihood function as described by Fisher (1997)

$$\mathbb{L}(z; \theta) = p(z | \theta)$$

Because θ is now assumed to be a vector of unknown constants, and not a random variable, the probability density function $p(\theta)$ is not defined, and Bayes's rule does not hold.

The most common estimator for the Fisher model is the maximum likelihood (ML) estimator, which is equal to the value of θ that maximises $\mathbb{L}(z; \theta)$ for given z .

According to Morelli and Klein (2016), no uncertainty models for θ and v are used for specifying the form of the least-squares model, i.e., there are no probability statements concerning θ and v . An estimate for the least-squares model can be obtained by the reasoning that, given z , the "best" estimate of θ comes from minimising the weighted sum of squared differences between the measured outputs and the model outputs,

$$J(\theta) = \frac{1}{2}(z - H\theta)^T R^{-1}(z - H\theta)$$

where R^{-1} is now a positive definite weighting matrix, chosen by judgement. Optimisation of the preceding $J(\theta)$ leads to the well-known weighted least-squares (WLS) estimator. In the special case where $R = I$, the ordinary least-squares (OLS) estimator is obtained, with the cost function

$$J(\theta) = \frac{1}{2}(z - H\theta)^T (z - H\theta)$$

Considering the entire set of measured data $z(i), i = 1, 2, \dots, N$, the OLS estimator for a scalar measurement is obtained by minimising

$$J(\theta) = \frac{1}{2} \sum_{i=1}^N [z(i) - h(i, \theta)]^2$$

6.2.1 Define a Linear Regression Model

For this experiment, the effect of certain parameter changes on the deflection caused by the thrust force needs to be modelled. It is assumed that the engine operation region can be approached with a linear regression model.

The linear regression model that best fits a sequence of measurements y is defined as follows:

$$y = A(x) \cdot \theta + \varepsilon$$

Where

$$\begin{aligned} y &= \text{the } N \times 1 \text{ measurement vector} \\ A(x) &= \text{the } N \times n \text{ regression matrix} \\ x &= \text{the } m \times 1 \text{ state vector} \\ \theta &= \text{the } n \times 1 \text{ parameter vector} \\ \varepsilon &= \text{the } N \times 1 \text{ model residual vector} \end{aligned}$$

The most widely used regression matrix is the polynomial structure. in that case $p_m(x(n))$ are ordinary polynomials in terms of x :

$$A(x) = \begin{bmatrix} 1 & x_i(1) & x_i^2(1) & \cdots & x_i^n(1)x_j^m(1) & \cdots & x_k^M(1) \\ 1 & x_i(2) & x_i^2(2) & \cdots & x_i^n(2)x_j^m(2) & \cdots & x_k^M(2) \\ \vdots & \vdots & \vdots & \vdots & \vdots & \vdots & \vdots \\ 1 & x_i(N) & x_i^2(N) & \cdots & x_i^n(N)x_j^m(N) & \cdots & x_k^M(N) \end{bmatrix}$$

Note that cross-terms are required in multivariate models. For the regression model, a polynomial model structure is a suitable choice to start with. The structure of $A(x)\theta$ is as follows:

$$A(x) \cdot \theta = \theta_0 + \theta_1 x + \theta_2 x^2$$

Where $\theta_0, \theta_1, \theta_2$ are the unknown model parameters. The linear regression model now is:

$$y = \begin{bmatrix} 1 & x & x^2 \end{bmatrix} \cdot \begin{bmatrix} \theta_0 \\ \theta_1 \\ \theta_2 \end{bmatrix} + \varepsilon$$

With the linear regression residual ε given as:

$$\varepsilon = y - A(x) \cdot \theta$$

and the linear regression estimator $\hat{\theta}$ given as:

$$\begin{aligned} \hat{\theta} &= \arg \min J(y - A(x) \cdot \theta) \\ &= \arg \min J(\varepsilon) \end{aligned}$$

Here J is a cost function that is used to minimise the error of a model with respect to the data. This function sums all error values ε for all values of x in a given set of parameters θ . Some examples of cost functions are:

$$J(x, \theta) = \sum_{i=1}^N \varepsilon_i = \sum_{i=1}^N y_i - A(x_i) \cdot \theta, \quad (\text{linear})$$

$$J(x, \theta) = \sum_{i=1}^N \varepsilon_i^2 = \sum_{i=1}^N (y_i - A(x_i) \cdot \theta)^2, \quad (\text{quadratic})$$

$$J(x, \theta) = \sum_{i=1}^N |\varepsilon_i| = \sum_{i=1}^N |y_i - A(x_i) \cdot \theta|, \quad (\text{absolute value})$$

$$J(x, \theta) = \sum_{i=1}^N W_{ii} \varepsilon_i^2 = \sum_{i=1}^N (y_i - A(x_i) \cdot \theta) \cdot W \cdot (y_i - A(x_i) \cdot \theta), \quad (\text{Weighted quadratic})$$

Note that a linear cost function is useless, as positive and negative errors can even each other out.

Least Squares Estimator Instead of minimising the errors directly, it is also possible to minimise the squares of the errors. To construct the least squares estimator or sometimes referred to as Ordinary Least Squares (OLS), the convex quadratic cost function is used as basis:

$$J(x, \theta) = \sum_{i=1}^N \varepsilon_i^2 = \sum_{i=1}^N (y_i - A(x_i) \cdot \theta)^2$$

Using matrix notation, this becomes:

$$J(x, \theta) = \varepsilon^T \varepsilon = (y - A(x) \cdot \theta)^T (y - A(x) \cdot \theta)$$

The least squares estimator is the solution to the optimisation problem

$$\hat{\theta} = \arg \min \varepsilon^T \varepsilon$$

This convex cost function has a minimum when

$$\frac{\partial J(x, \theta)}{\partial \theta} = \frac{\partial \varepsilon^T \varepsilon}{\partial \theta} = 0$$

The partial derivative with respect to θ of the quadratic cost function is:

$$\begin{aligned} \frac{\partial \varepsilon^T \varepsilon}{\partial \theta} &= 2\varepsilon^T \frac{\partial \varepsilon}{\partial \theta} \\ &= 2(y - A(x) \cdot \theta)^T \cdot -A(x) = 0 \end{aligned}$$

By introducing $\hat{\theta}$ as the particular value for θ , the cost function is minimised. Dividing this equation by -2 results in the following equation:

$$(y - A(x) \cdot \hat{\theta})^T \cdot A(x) = 0$$

Transposing this results in:

$$A^T(x)(y - A(x) \cdot \hat{\theta}) = 0$$

Expanding the term in brackets and isolating $\hat{\theta}$ gives:

$$\hat{\theta} = \left(A^T(x) \cdot A(x) \right)^{-1} A^T(x) \cdot y$$

Which is the Ordinary Least Squares (OLS) estimator for $\hat{\theta}$. According to Paoletta (2019), $\hat{\theta}_{OLS}$ has the smallest variance among all linear unbiased estimators; this result is often referred to as the Gauss–Markov Theorem, and expressed as saying that $\hat{\theta}_{OLS}$ is the best linear unbiased estimator, or BLUE. And can be proved accordingly.

For an unbiased estimator, the following must hold:

$$B\{\hat{\theta}\} = E\{\hat{\theta}\} - \theta = 0$$

with $B\{\hat{\theta}\}$ the estimator bias, and with θ the true parameter that is being estimated.

By writing the estimated parameters in terms of true parameters and residuals, the bias of the estimated parameters can be checked.

$$\begin{aligned} \hat{\theta}_{OLS} &= \left(A^T(x) \cdot A(x) \right)^{-1} A^T(x) \cdot y \\ &= \left(A^T(x) \cdot A(x) \right)^{-1} A^T(x) \cdot (A(x)\theta + \varepsilon) \\ &= \left(A^T(x) \cdot A(x) \right)^{-1} A^T(x)A(x) \cdot \theta + \left(A^T(x) \cdot A(x) \right)^{-1} A^T(x) \cdot \varepsilon \\ &= \theta + \left(A^T(x) \cdot A(x) \right)^{-1} A^T(x) \cdot \varepsilon \end{aligned}$$

Taking the expectancy of left and right hand terms results in:

$$E\{\hat{\theta}_{OLS}\} = E\{\theta\} + \left(A^T(x) \cdot A(x) \right)^{-1} A^T(x) \cdot E\{\varepsilon\}$$

This clearly indicates an unbiased estimator if $E\{\hat{\theta}_{OLS}\} = E\{\theta\}$ which implies $E\{\varepsilon\} = 0$. Hence, all least squares estimators assume $E\{\varepsilon\} = 0$.

Besides the OLS estimation method, several other methods like Generalised Least Squares (GLS) or Maximum Likely Estimation (MLE) are suited to estimate the parameters of the polynomial model.

6.3 Conclusion

Several methods to model the behaviour of the vibration isolator of the Cessna model 550 are discussed. The physical models, using various combinations of spring damper systems to model certain characteristics in one dimension. For this research however, the main interest is the influence of a vibration outside the vibration plane, thus more than one dimension. To expand on the model dimensions, a linear regression model approach is considered. This enables the modelling of multiple independent variables on the dependent variable.

Since there is no prior knowledge about the behaviour of the vibration isolator, a broad approach is chosen which is to be refined throughout the modelling process. All with the assumption that the model is approachable with a static linear regression model. If not, the scope needs to be expanded to dynamic models.

Chapter 7

Problem Formulation

Direct measurement in-flight thrust is considered infeasible due to the complexity of the mounting structure. This counts for the commercial aircraft engines, however, a part of the general aviation uses a simpler engine mounting construction which allows for the measurement of the vibration isolator.

The currently used methods relate engine flow parameters during flight to the performances in a test cell. The use of a test cell is an expensive undertaking and the deterioration of the engine is not accounted for. Using the vibration isolator deflection as a thrust measure costs a fraction of the previously mentioned method. This master thesis research aims to lay the foundation for a new and cost efficient method of constructing engine models. This by determining how suitable the engine vibration isolators are for this purpose.

7.1 Research Question

The main research question states:

How can the jet engine vibration isolator deformation be used to estimate the thrust force?

Where this research mostly focuses on the actual engine vibration isolator. If the outcome of this research is positive, subsequent research on the PH-LAB can be performed to validate the claims. The later phases two and three of testing the system on the aircraft reaches the size of a PhD research.

To answer the main question, several sub-questions are imposed to break up the large sum of work. By answering each individual sub-question, the answer to the main question will develop over the span of the research. The sub-questions are as follows:

1. How can a vibration isolator be modelled?
 - What are the current methods of modelling vibration isolators?
 - How is the construction of the model performed?
 - What are the real life constrains for modelling viscoelastic materials?
 - How can the model be verified and validated?
 - Is the model reproducible?
2. What are the experiment setup requirements?
 - What are the engine vibration characteristics?
 - How can the test frame be used in both, test setup and aircraft engine?
 - What are the sensor requirements?

Hypothesis

The research questions form a framework that helps to answer the main question. The theoretical research questions will be answered in the literature study. While the remaining questions require experiments, which will be performed during the master thesis research. The verification and validation of the resulting model is as important as the construction of the model. Therefore, some experiments will be performed in at least two independent runs, where the results can be compared for dissimilarities.

7.2 Research Objective

The specific research objective for the problem formulated in the previous section is stated as follows:

To achieve a validated mathematical jet engine vibration isolator model with the purpose of estimating the thrust magnitude during flight by using a test setup that simulates the environment that the isolator experiences during flight.

7.3 Research Scope

The research of using the vibration isolator deformation as a measure for thrust is divided into three phases. The first phase involves the construction of a dynamic model of the vibration isolators and concluding if the vibration isolators bear the right characteristics for this purpose. The second phase is preparing the whole test setup for static engine tests and perform static engine test runs to validate the first phase. The third phase consists of making the test setup airworthy which includes certification, once this is performed, test flights are required.

The main objective of this thesis research is phase one and determine the feasibility of using the deformation of the vibration isolator to determine the applied load, in this case the jet engine thrust. To determine the feasibility of the measurement method, the consistency of the stiffness of the vibration isolator is an important factor. The stiffness of the vibration isolator is the dependent variable where, for example, vibration frequency, and amplitude or temperature are the independent variables. As mentioned, the research is focused on the PH-LAB. Therefore, the vibration isolators of the Cessna model 550 are used for the experiments.

Within the scope of research:

- Design and manufacture test setup frames that can be used on both the test machine and PH-LAB
- Perform experiments on the influence of vibration, preload, and temperature
- Generate dynamic vibration isolator model of either the top or bottom isolator

Outside the scope of the research:

- Static engine runs for the engine model
- Generation of engine model
- Test flights

7.4 Research Necessities

In order to start with the experiments, a vibration isolator is required. It is assumed, the PH-LAB crew will order a new engine vibration isolator for this purpose. Without this isolator, this master thesis research cannot be performed. Furthermore, it is assumed that a test bench in the aircraft hall can be used for testing the vibration isolator. The research group which operates the aircraft hall expected no problems to use the MTS-831 test machine in the period of February and March.

7.5 Research Assumptions

For this master thesis research, several assumptions are made regarding the material properties and the experiment setup. The ageing of the viscoelastic material is assumed to not influence the experiment results. This, because the experiments are performed over a time span of weeks and the isolators are in general used well over a decade.

It is assumed that the vibration isolators are the only load-paths for thrust to transfer between engine and airframe. The pylon-cowling seal is a fabric and restricts the transfer of thrust, while tubing and cabling is designed to not transfer thrust to the airframe.

Due to the circular shape of the vibration isolator, it is assumed that the model dimensions can be reduced to axial and radial.

The engine vibration in the forward direction is assumed to be negligible, as the engine vibrations are generated by the unbalance of the rotating components and the forward direction is perpendicular to the plane of rotation.

Chapter 8

Conclusion

This literature study considers the development of an in-flight thrust measurement device. This measurement device is possibly the key to accurate and cost-efficient mathematical model generation of aircraft jet engines. The new method of measuring the missing aircraft model input, thrust, is performed by measuring the aircraft engine vibration isolator deformation.

In order to measure the thrust in flight in this fashion, an accurate model of the vibration isolator is required. The characteristics of the vibration isolator are influenced by independent parameters such as vibration frequency and amplitude or temperature. By performing experiments that encompass these independent parameters, better mathematical models of aircraft can be constructed. It follows that better simulators, more accurate aircraft handling predictions and a higher safety during experiments can be assured.

In this thesis, the mathematical model of the vibration isolator of the Pratt & Whitney Canada Inc. JT15D-4 will be constructed. This is the jet engine installed on the PH-LAB, a Cessna Citation II model 550 which is the intended test platform. The mathematical model of the vibration isolators is constructed by performing experiments on the elastomer testing machine in the aircraft hall at the TU Delft. These experiments outline the influence of each independent parameter and the correlation between the independent parameters. These results can be combined into a mathematical model that describes the behaviour of the vibration isolator in a broad range of conditions. The results answer the following main research question:

How can the jet engine vibration isolator deformation be used to estimate the thrust force?

A conclusion can be formed by answering the sub-questions on which is elaborated in the previous chapter. And, by analysing the characteristics of the vibration isolator and the isolator model that are formed by the experimental data. The model should be accurate and, most importantly, consistently reproducible.

The literature study covers a wide variety of research fields, yet all fields coincide with the need for mathematical models. In this example, the aircraft flight dynamics model requires a better thrust input, this can be solved with a better aircraft engine model. For this, a model of the engine vibration isolator is required, which is in the viscoelastic material research field. Combining such a variety of research topics can be challenging, yet also very educational.

Part II

Thesis

Chapter 9

Introduction

In this chapter, more information can be found on the case which is studied in this research. More information about the problem statement and the context of the problem can be found in section 9.1. The approach to determine the characteristics, together with the challenges that arise with the approach, are presented in section 9.2. The contribution of this research to science is clarified in section 9.3. The research objectives and the reasoning behind the objectives can be found in section 9.4.

9.1 Context and Problem Statement

The concept of using the vibration isolator as a thrust sensor is a newfound approach. In order to determine if the vibration isolator is a suited object to use as a thrust sensor, a characterisation of the object is required. For this characterisation, different environmental and operational conditions of the vibration isolator are simulated to measure the influence on the deflection. Several conditions like temperature, weight, vibrations and thrust force are varied throughout the measurements to determine the influence.

A variety of approaches are available to evaluate the concept feasibility. In the first approach, the experiments are performed on the aircraft to allow for the most realistic setup. The downside of this approach is the lack of controllability over the environmental conditions. Furthermore, mechanical system adjustments require certification by the governing authorities, and consequently take up a long time. The second approach utilises a jet engine in a separate engine mounting rig, which requires no certification. Even so, no full control over the environmental and operational conditions is available. The last approach analyses the vibration isolator in laboratory conditions to have full control over the environmental and operational conditions. Moreover, the construction of a laboratory setup with experiments is feasible within the given timespan of a graduation.

For this research, an elastomeric test machine is used to provide full control over each dependent variable and determine the influence of each parameter. For the experiments, a biaxial test machine is required, as thrust and engine weight are excited perpendicularly. This requires the design and manufacturing of an additional setup. The goal is to determine if the material properties of an engine vibration isolator are adequate to function as a thrust sensor. Knowing the relative dependency on varying operational or environmental conditions outlines the applicability of the concept. Additionally, identification experiments are performed to capture the system dynamics and generate a single input, single output thrust model.

9.2 Approach and Challenges

Since the application of the vibration isolator is intended differently than this research proposes, little about the characteristics that influence the deflection in flight direction has been researched. Therefore, a wide approach that investigate the influence of several parameters is required. Then the importance or influence of each parameter is determined during the experiments. The most suitable approach is using an elastomeric test machine. The aircraft hall is equipped with such a machine and was available for testing. This device, however, only tests in one dimension. This approach includes the following steps:

1. Obtain a vibration isolator
2. Build a setup that simulates the thrust force
3. Build a setup that measures the deflection due to the thrust force

4. Perform the characterisation experiments to determine the parameter dependency
5. Perform the identification experiments to capture the dynamic behaviour
6. Generate a mathematical model based on the identification data

The experimental results answer the following question:

How can the engine vibration isolator be used to predict in-flight thrust?

9.3 Contributions

The in-flight thrust is interesting for several areas of aerospace research and development. The first field of research is aircraft system identification. To perform system identification of a dynamic system, all input and output parameters must be known and for aircraft, the thrust input parameter is not precisely defined.

The second field of research is aerodynamics, in which the lift-to-drag ratio is one of the main design factors. It should be noted that thrust equals drag in steady forward flight and if the thrust is measured, the lift-to-drag ratio is directly determined. Additionally, the effect of in-flight configuration changes and setup adjustments on the total drag can be measured.

The third and final field of research is engine development, where access to an in-flight thrust reading reduces the amount of engine removal and installations in the development phase. This in turn facilitates the monitoring of low-frequency engine degradation or high-frequency engine stall and surge characteristics.

9.4 Research Objective

The goal of this research is to determine if the engine vibration isolator of the Cessna model 550 can be used to determine the in-flight thrust. An actual vibration isolator of the Cessna model 550 is used as a test object to determine if the characteristics are suited for this purpose. and the research objective is stated as follows:

To achieve a validated mathematical jet engine vibration isolator model with the purpose of estimating the thrust magnitude during flight by using a test setup that simulates the environment that the isolator experiences during flight.

Chapter 10

Experiment Setup

This chapter discusses the different components of the experiment setup and the functioning of each component. The chapter is added to create a deeper understanding of the approach and potential limitations of the test system. Converting a one-dimensional test system into a two-dimensional test system is accompanied by some assumptions and simplifications. Furthermore, the construction details are of importance to ensure the reproducibility of the experiments.

The first section discusses the elastomeric test machine which is located in the aircraft hall of the TU Delft. Following, the thrust force simulation is discussed, including construction and functioning. Subsequently, the different adaptors with their according purposes are discussed.

10.1 Elastomer Test System

This section discusses the elastomer test system that is used to simulate the engine vibrations. The system is manufactured by MTS, which is a leading global supplier of test systems. This particular system is optimised to characterise elastomeric materials using an electronically steered hydraulic cylinder that can simulate vibrations up to 550 Hz. The test machine is equipped with a ThermoTron temperature control chamber to control the temperature of the experiment specimen.



Figure 10.1: MTS Elastomer Test System 831

The MTS test system is equipped with several connections to mount test specimens, of which one is the standard M20 connection. This connection allows for the mounting of the manufactured adaptors for the vibration isolator. On the lower connection side, a 10 kN load cell is mounted. On the top side, the hydraulic cylinder of the MTS test bench is located. This hydraulic cylinder also contains an LVDT, which measures the translational displacement. Note that this LVDT is inconvenienced with measuring both the deflection of the test specimen and the strain of the cylinder rod and adaptors. In between the cylinder and the load cell, the test specimen is fixated.

10.1.1 MTS Software

The MTS test system contains several software packages, each developed for different purposes. One of the software packages is the dynamic characterisation software, which enables the user to build programs that sweep through frequencies, amplitudes, or load levels in different nesting levels. Allowing the user to specify a point cloud of measurement points where the three axes are the following variables: frequency, amplitude, and preload.

Retrieving data Two types of data acquisition are possible. The first is a simple continuous recording of predefined sensors at a certain sampling frequency. The second has the option to record the average value of certain channels over a predefined period of time. This approach allows for recording the peak-peak values during this measurement time to estimate the variation during the measurement. The last approach is used to perform a variety of measurements over the wide spectrum of frequency, amplitude, and preload.

To ensure that the measured data points are not influenced by the dynamic response of a setup change. A resting period or so-called dwell is added in the program. The first type is a static dwell, which allows the creep and stress relaxation to settle and not influence further measurements. For the static dwell, a time period of 30 minutes is used. The second type is a dynamic dwell, which is a period of time at which the frequency, amplitude, and load level are maintained at a constant level before starting the measurement. This prevents any dynamic effects from influencing the measurements.

The average values of the measurement time are evaluated for consistency and, if consistent enough, placed in the measurement file. At high damping regions with low amplitude, the measurements tend to get rejected due to the larger noise during the measurement.

Measurement data The measurements are written in a file structure which is separated by test day and experiment number for that day. In a separate lablog, the experiment purpose and experiment parameters are noted together with any observations or abnormalities. The MTS software allows for both continuous measurements and averaged measurements at the same instance. Both are placed in the assigned experiment run folder. Additionally, Fourier analyses of each measurement period are generated and placed in a separate file within the specimen folder. The Fourier transforms are used to investigate eigenfrequencies in the experiment setup.

10.2 Thrust Force Simulation

The main vibration direction of the engine is radial and thus perpendicular to the thrust direction. To simultaneously generate the vibrations and simulate a thrust force, an additional dimension is required on the test machine. This extra dimension is added with a custom-made hydraulic system.

With the dimensions of the vibration isolator, provided by Textron Aviation, a 3D model of the isolator is generated. With this three-dimensional model, the adaptors for the experiments are designed. With the design, it was important that the induced forced did not influence the measured force in the perpendicular direction. Meaning that the thrust force must be contained in a closed system and no forces can "leak". Therefore, no physical connections or support besides the connection to the MTS load cell and cylinder are constructed.

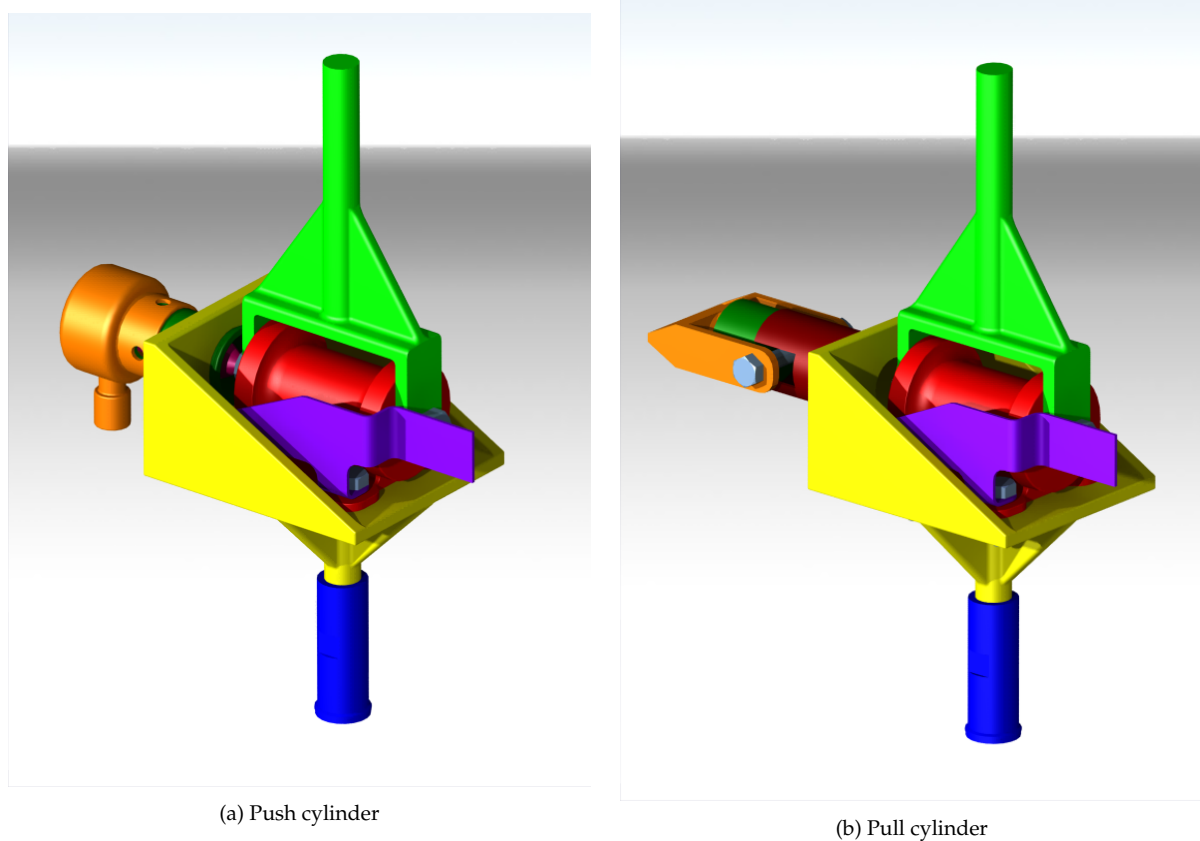


Figure 10.2: Thrust simulation setup designs

Figure 10.2 shows two of several designs to simulate the thrust force in an isolated condition. The different parts are distinguishable by colour. The main component, the vibration isolator, is the cylindrical shaped part (red). The vibration isolator is mounted on the base plate (yellow) by four bolts. The base plate routes the force that is placed on the vibration isolator back to the cylinder to achieve a closed system. In order to measure the deflection that is caused by the simulated thrust force, a sensor mount (purple) is mounted under the attachment bolts of the vibration isolator. The sensor mount is designed such that it can be used directly on the research aircraft. The M20 adaptor (blue) enables the mounting of the system to the MTS clamp connection. A similar adaptor is attached to the fork, which is left out of the image for clarity. The vibrations that are generated by the MTS machine are transferred into the vibration isolator via the fork (light green) which is clamped over the isolator and fastened with the isolator mounting bolt.

To simulate the thrust force, several concept designs are created. Figure 10.2a shows the push cylinder concept where the piston rod is pointed towards the vibration isolator. This design is aborted as it would restrict the perpendicular vibrations generated by the MTS machine. The pulling cylinder concepts as shown in fig. 10.2b is more complex, though stable in nature, and allows for a rotation point between the cylinder and the pull rod which is connected to the isolator mounting bolt.

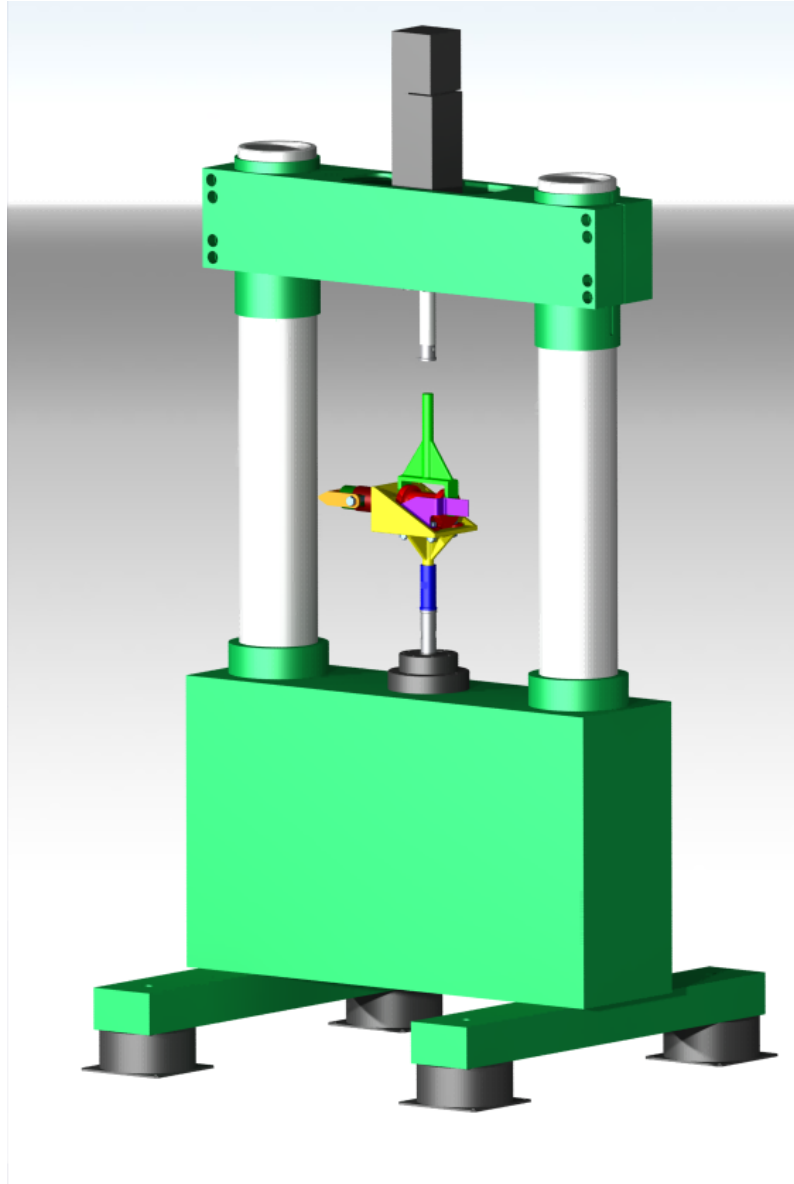


Figure 10.3: MTS Elastomer Test System 831 with adaptors and test object

The final design of the experiment setup is shown in fig. 10.3. Around the experiment setup, an oven is placed to control the temperature of the test object. This oven is equipped with three feedthrough holes, one in both the top and bottom and one in the right-hand wall. The initial design would place the cylinder through the hole in the sidewall, however, this hole appeared to be out of plane with the holes in the top and bottom of the oven. Therefore, the design is altered, and the thrust cylinder is placed through the door of the oven.

10.2.1 Hydraulic Cylinder

During the search for a suitable hydraulic cylinder to use in the experiment setup, a cylinder with a ball joint was found. In this setup, the ball joint is placed at the cylinder base, resulting in a large rotating length. A large rotation length results in a lower angular displacement of the force on the vibration isolator. Note that the hydraulic cylinder is connected to the vibrating input of the experiment setup. This is important to rule out the influence of the inertia of the cylinder on the MTS load cell readout. In order to prepare the cylinder for use, a sandblast treatment followed by a length adjustment as seen in fig. 10.4 was required. The cylinder rod end was grinded to a cone shape, this allows the rod to align with the centre of the vibration isolator mounting bolt.

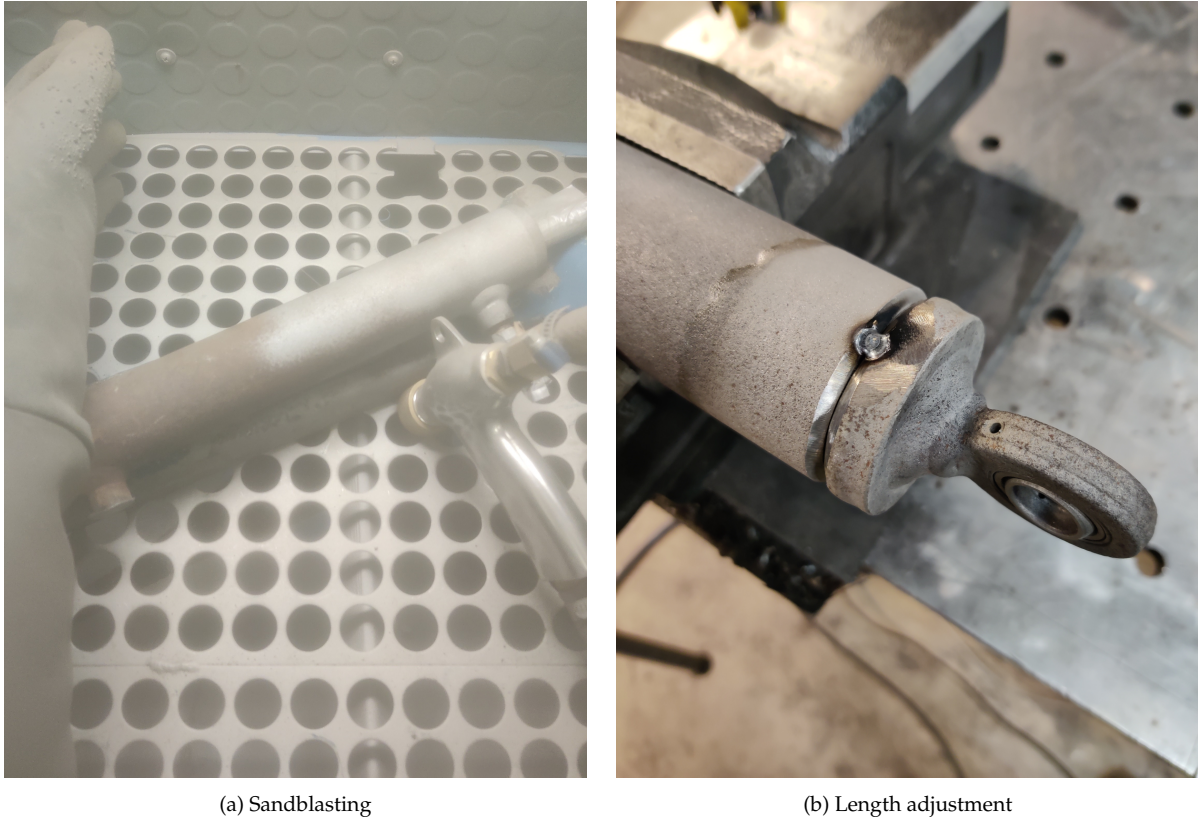


Figure 10.4: Cylinder preparation

The maximum force a JT15D-4 engine produces is approximately 2500 lbs of thrust force according to Pratt & Whitney (1975). This translates to a maximum thrust force of 11 kN per engine. This force is divided over two engine vibration isolators, resulting in a maximum constant load of 5.5 kN per isolator. A hydraulic cylinder or a linear hydraulic motor transfers oil pressure into a unidirectional force. Knowing that the diameter of the hydraulic cylinder plunger is 40 mm, the required maximum pressure is calculated as follows:

$$F = \frac{P\pi D^2}{4} \quad (10.1)$$

$$P = \frac{4F}{\pi D^2}$$

$$P = \frac{4 \cdot 5500}{\pi \cdot 40^2} \quad (10.2)$$

$$P = 4.4 \frac{N}{mm^2} = 44 \text{ bars}$$

To generate a constant pressure of 44 bars, several systems are explored. The first hydraulic system is powered by an electrical hydraulic pump with a flow reduction valve. This resulted in overheating problems due to the large flow of the available hydraulic pump. The second hydraulic system contained a manual pump in combination with a 3-way pressure reducing valve. This hydraulic system was found infeasible, as the leak volume of the 3-way pressure reducing valve drained the high-pressure accumulator faster than anticipated. The final hydraulic system contains a 2-way pressure reducing valve with a maximum set value of 60 bars in combination with accumulators. The difference between the 2-way and 3-way valve is that a 2-way valve only increases the pressure on the out port to a set value, where a 3-way valve also reduces the pressure on the outport if necessary. For the experiment setup, no large increases in pressure are expected on the outport of the 2-way valve, as the hydraulic cylinder is not expected to have a large stroke due to the induced vibrations. The hydraulic scheme of the used system is found in fig. 10.5

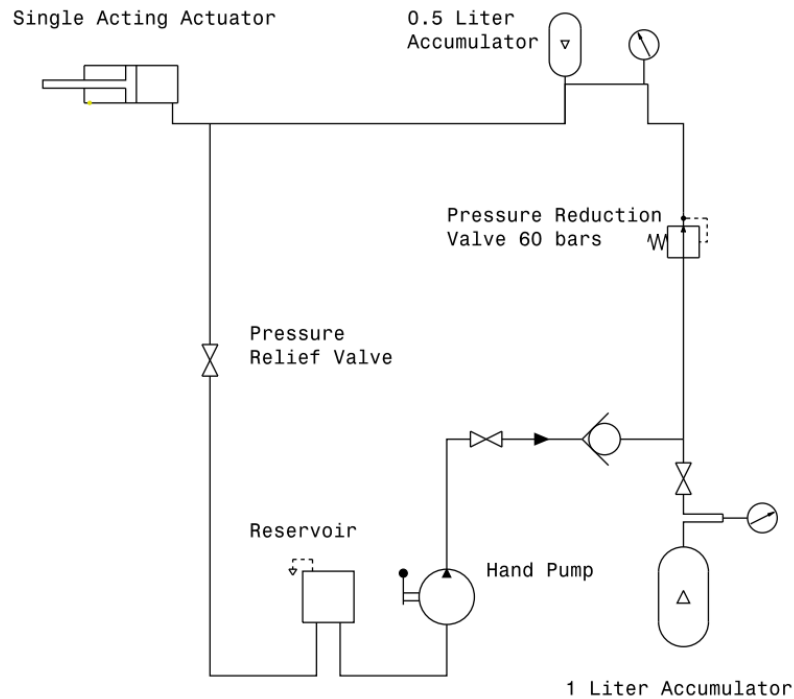


Figure 10.5: Hydraulic scheme of experiment setup

The hand pump of the hydraulic system includes a one-litre oil reservoir. Since the accumulators contain a larger volume than the reservoir, the high-pressure accumulator is equipped with a shut-off valve to prevent it from draining when the system pressure is relieved. The hand pump was initially connected directly to the check valve. This caused a measurable pressure drop over the time span of days. Therefore, an extra shut-off valve is placed before the check valve. With the hand pump, the high-pressure accumulator is charged, with this high pressure and the pressure reducing valve, the pressure on the actuator side is constant. Experiments showed that the pressure reducing valve is actually not required, as the system does not leak. This excludes any regulation errors the pressure reducing valve introduced. With all components sorted, a stand was built to mount the components as shown in fig. 10.6. Partly due to the fact that accumulators require a specific mounting position, and partly for the aesthetics and usability of the system.



Figure 10.6: Hydraulic components stand construction

With the correct cylinder and pressure control system, the following step is to determine the exact force that is provided by the hydraulic cylinder. Three feasible options are considered, of which the first option is an off the shelf load cell that is placed between the hydraulic cylinder and the engine vibration isolator. The benefit of this method is the ease of installation, the downside however is the large sideward accelerations and the associated forces. Load cells tend to be sensitive to sideward forces and vibrations, resulting in decreasing accuracy or malfunction (Kopczynski, 2011). The second option exploits the fact that the force is linearly related to the hydraulic oil pressure. To reach the intended accuracy, this option was found to be unnecessarily expensive. The third and last option makes use of the material properties of the hydraulic cylinder rod. By placing strain gauges on the rod, the strain of the material is measured. For metals, this strain is linearly proportional to the applied force at low stresses, according to Smallman and Bishop (1999). To compensate for the temperature changes, a Wheatstone bridge, containing four strain gauges, is implemented (Wheeler & Ganji, 2009). This bridge is composed of Kyowa KFGS-5-120-C1-11 strain gauges, where two gauges are placed parallel to the force direction and two perpendicular to the force direction, this compensates for material expansion due to temperature changes. The Wheatstone bridge is connected to a Peekel Picas amplifier system via a 9-pins D-sub connector. The required output voltage of the amplifier system is ± 10 Volt, which is required to match the analogue input voltage of the MTS system. In the calibration test bench, the correct Peekel settings and force-voltage relations are determined. This calibration test bench is a 10 kN Zwick-Roell's static test bench, which adjusts the table height or applied force using electrically driven ball-spindles, and is shown in fig. 10.7. The ball-spindle adjustment allows for a more stable and controlled measurement compared to the hydraulic steered MTS test bench.

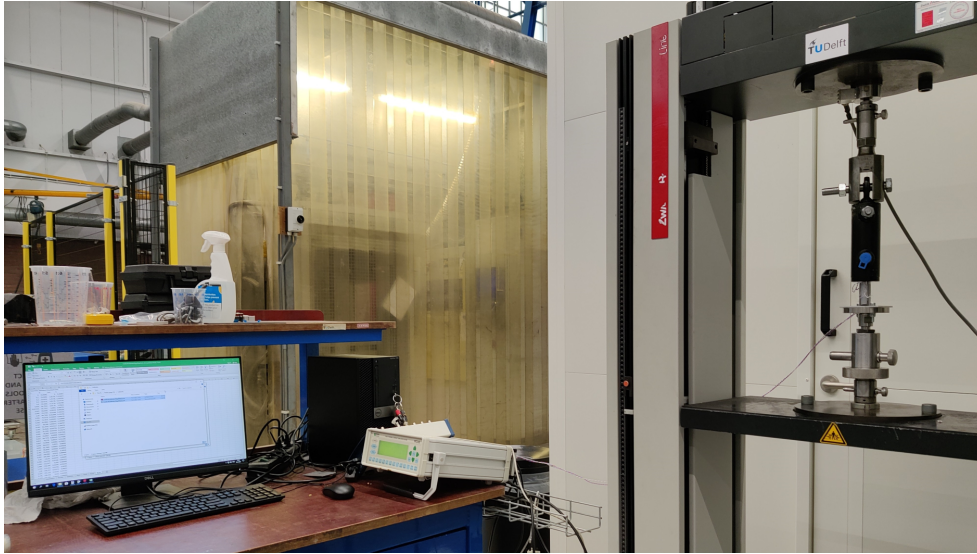


Figure 10.7: Zwick-Roell's cylinder calibration setup

The calibration program consisted of triangular-shaped force cycles with an incline of 1 kN per ten seconds. The calibration program cycles three times between -100 N and -4 kN , with a plateau of two seconds between each segment. Using the force and voltage data of the calibration cycle, the linear relation is determined. Each volt difference, measured over the strain-gauge bridge, corresponds to 1108 N with a root mean square error of 57 N . This force over voltage ratio is used to determine the force provided by the hydraulic cylinder during the experiments.

10.2.2 Adaptors

The adaptors are manufactured by exporting the 3D models to Drawing Exchange Format (DXF) files, which are loaded to a CNC plasma sheet metal cutting machine. This resulted in 8 mm thick sheet metal components. Welding these individual components together resulted in the adaptors to mount the vibration isolator. The 8 mm thickness is sufficient to prevent undesired deformation in the adaptor.

Two different base plate mounts are constructed. The first base plate allows for horizontal mounting of the vibration isolator, and is shown in fig. 10.8. In the horizontal position, the thrust is simulated with the additional hydraulic cylinder. The second base plate allows for vertical mounting in the MTS machine and determine the dynamic characteristics in the thrust direction. The vertical mounting construction is shown in fig. 10.9 where it is placed in the oven.

During the first experiment run, it appeared that the MTS hydraulic cylinder rod was stiffer than expected. Meaning that an application of simulated thrust force by the secondary hydraulic cylinder on a stiff fork adaptor would damage the MTS cylinder seals. Also, the thrust force input would partially flow through the MTS machine and cause a readout error. For this reason, an extra fork shaped adapted is manufactured that allows for horizontal movement. This fork contains a sliding member which eliminates the force flow through the MTS cylinder rod as shown in fig. 10.10.



Figure 10.8: Horizontal mounting



Figure 10.9: Vertical mounting



Figure 10.10: Fork adaptors

10.3 Deformation Measurement

The thrust force which is generated by the aircraft engine is transferred to the airframe via the engine vibration isolators. The previous section discussed the setup to simulate the engine thrust force. This section focuses on the measurement of the deformation of the engine vibration isolator, caused by this simulated thrust force. For the measurement of the deformation of the vibration isolator, it is important to understand that the vibration isolator consists of two metal components with a silicon rubber lining in between. The vibration isolator mounting plate is mounted on the JT15D-4 engine with four bolts. The isolator is connected to the airframe by a single bolt that clamps the isolator in the forward mount. The

two end plates of the isolator are connected with a metal tube. This allows for a deformation measurement that is not at the side of the force application.

A selection of possible sensors is considered to measure the deformation. The sensor is required to be highly temperature and vibration resistant. The Linear Variable Differential Transformer (LVDT) sensor was found most suitable. The most suitable and available LVDT for this application in the laboratory is the 7DCDT-250, a Hewlett Packard Direct Current Linear Variable Differential Transformer (DC LVDT). The difference between direct and alternating current LVDT sensors, is the location of the electronics for the signal conditioning. For a DC LVDT, the signal processing is performed by an external instrument. Using a DC LVDT has the advantage of a larger temperature and vibration operation range, as no electronics are exposed. The only electronics in the sensor is a built-in carrier oscillator and phase-sensitive demodulator. These components allow for an extremely high resolution of up to $0.001 \mu\text{m}$, zero hysteresis, a non-linearity of $\pm 0.5\%$ over the total stroke, and an operation temperature range of -45°C to 120°C (Robb, 1965).

The LVDT sensor is mounted on a custom designed bracket with consideration of potential airworthiness certification. The bracket is mounted on the engine without any structural changes required, as it is mounted with the same bolts that mount the vibration isolator. Since the bracket uses two of the four bolts, it can be mounted with the engine installed. Figure 10.11 shows the CAD model (purple) and the setup of an LVDT calibration run. During the LVDT calibration run, the vibration isolator is removed to mount the LVDT up side down.

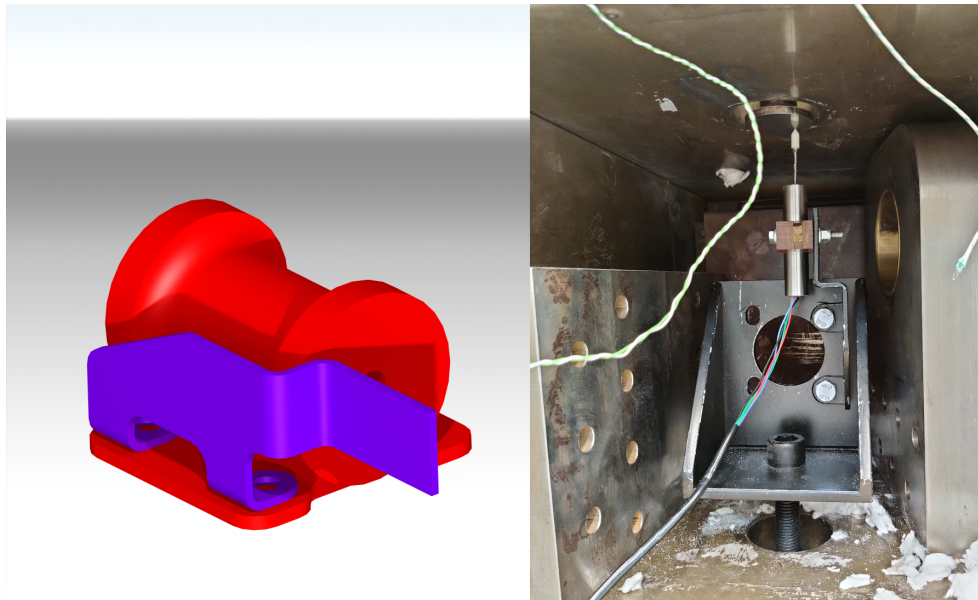


Figure 10.11: LVDT bracket design (left) and experiment setup (right)

10.4 Conclusion

This chapter discussed the design process and considerations of the construction that adds an extra simulation dimension to the MTS-831 elastomeric test machine. This is necessary to simultaneously reproduce the engine vibrations and the engine thrust force. The engine vibrations and engine thrust are perpendicular because the main engine vibrations are caused by unbalance of the engine rotors, resulting in radial vibrations, while the thrust force is in axial direction.

The simulated thrust force measurement is performed with a Wheatstone-bridge and the corresponding deformation is measured with an LVDT. Calibrating the sensors allows for accurate measurements during the experiments.

To isolate the thrust force and prevent force leakage to the MTS machine, an adaptor with a sliding member is constructed. This allows for accurate and unconstrained vibration isolator deformation by the thrust force. The mounting bracket of the LVDT is custom designed with consideration of potential

airworthiness certification. The bracket is mounted with the same bolts as the engine vibration isolator and allows for mounting with the engine installed.

Chapter 11

Experiments

This chapter discusses the two different types of experiments that are performed on the vibration isolator. Starting with the characterisation experiments, which are performed to determine the influence of environmental and operational conditions on the stress-strain curve in the thrust direction. This is necessary to determine if the vibration isolator bears the right characteristics to be used as a thrust sensor. The last type of experiments are the identification experiments, these are performed to model the vibration isolator in the thrust direction under constant environmental and operational conditions. For each experiment, certain assumptions and simplifications are made to enable to perform the experiments at a TU Delft facility and reduce the required experiment duration. These assumptions or simplifications are discussed throughout this chapter.

11.1 Characterisation Experiments

These experiments are constructed to determine the influence of the environmental and operational conditions; frequency, amplitude, engine weight, and temperature on the isolator deflection that is caused by the thrust force. The influence of each individual parameter is investigated, assuming that two parameters without influence also do not influence the results when combined.

For each experiment, a program is written which specifies the experiment conditions and the order in which the different parameters are adjusted. Parameters that are not controlled by the MTS software are the temperature of the environmental test chamber and the simulated thrust force. The environmental test chamber is controlled by a separate temperature controller which only permits constant temperatures, and the control of the simulated thrust force is performed manually using the custom-made hydraulic setup.

11.1.1 Frequency

Frequency is the first independent variable, meaning it is a suspect of influencing the thrust force-deflection curve. To measure this influence, a constant thrust force is applied to the horizontally mounted vibration isolator for a period of time. This allows to capture the creep or stress relaxation dynamical behaviour. After which the experiment program is started, this program loops through the predefined frequencies which are either linear steps, logarithmic steps or a selection of prime numbers. The prime numbers are used to ensure no tones are measured multiple times. The highest frequency the jet engine produces is 525 Hz and for the simulations, up to 540 Hz is used to have a margin.

For the frequency experiments, several assumptions are necessary as the testing capabilities are limited. The first assumption concerns the angle of vibration application. It is assumed that the angle at which the vibration is applied, in the plane perpendicular to the force, does not influence the results. Mainly because the vibration isolator has a symmetrical shape in the plane perpendicular to the thrust force. The second assumption states that the reduction of the vibration dimension to one degree does not influence the measurement results. The MTS experiment setup only permits inline vibration shapes, and not the circular path a rotating device produces. The third assumption allows the vibration of the rotating components to be approximated with sinusoidal wave shapes. This follows from the reduction of dimensions. Lastly, it is assumed that the superposition of two engine vibrations does not result in a change of characteristics.

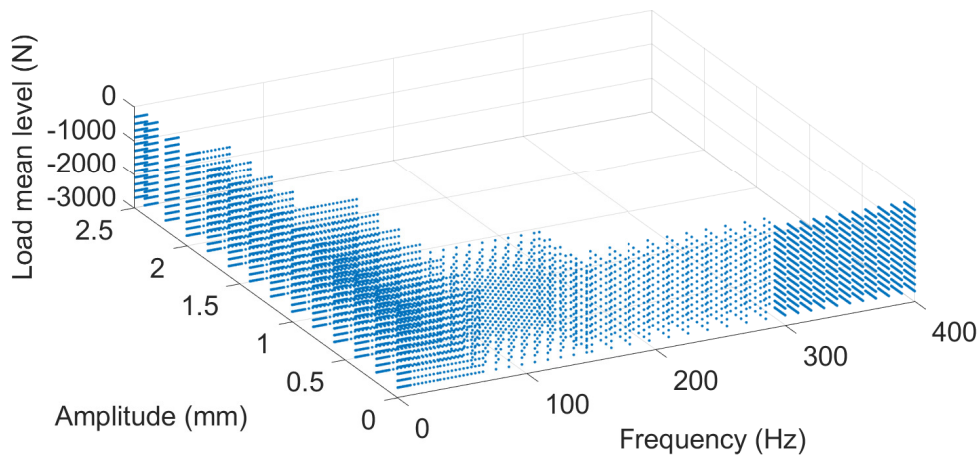


Figure 11.1: Measurement points in experiment program

11.1.2 Amplitude

The amplitude of a vibration is closely related to the frequency in terms of vibration acceleration. The acceleration of a vibration is linearly related to the amplitude and quadratically to the frequency of the vibration. To reach the target frequencies with sensible excitation, the amplitude of the vibration is the main control parameter. Exciting the system at 10 Hz with a 2 mm amplitude produces sensible vibrations. Increasing the frequency to 500 Hz with the same amplitude would break the machine, specimen and/or the adaptors. An example of the measurement points for a typical characterisation experiment is provided in fig. 11.1, which shows the required decrease of amplitude with increasing frequency.

For a jet engine, the frequency and amplitude of the vibration change simultaneously. Unlike the MTS test machine, where the software only permits stepwise adjustments of the frequency or amplitude. To investigate if the order of application of frequency or amplitude changes influences the measured deflection, the nesting level of frequency and amplitude are changed throughout the experiment.

N

11.1.3 Mean Load

With mean load or sometimes called preload, the supporting force of the engine mass is simulated. For a steady straight flight, this is expected to be relatively constant. However, the main goal is to perform test flight manoeuvres which result in varying accelerations and therefore varying engine weights. The simulated weight force is superimposed with the simulated vibrations. Hence, the name mean load.

The MTS test machine is able to steer the mean load based on force or displacement. The difference is the measurement location. Force steered uses the output of the dynamic system as input for the control input and displacement uses the input of the dynamic system as input for the controller and is therefore more accurate and less noisy.

The mean load is adjusted in linear steps subsequent to each frequency sweep. As the specimen is subjected to creep, the load is maintained at a constant value for 30 minutes before the following frequency sweep is started. The dynamic characteristics of the load force are interesting if non-steady flight measurements are performed. If a measurement is performed during flight manoeuvres, the weight of the engine is not constant and is dependent on the directional acceleration.

For the experiments with varying mean load, two assumptions are imposed. Firstly, it is assumed that the angle between the mean load or preload and the mounting plate of the vibration isolator has no influence on the measurement results. This assumption is imposed since the vibration isolator is cylindrically shaped. Secondly, it is assumed that aligning the preload and the vibration does not influence the measurement results. This assumption is required to reproduce both, the engine vibrations, and the mean load with the same hydraulic cylinder. Without this assumption, a third dimension is required in the test setup.

11.2 Temperature experiments

Temperature tends to have an influence on the characteristics of the material. To measure the influence of varying temperatures, several experiments are performed. In the horizontal mounting position, a frequency and amplitude experiment is performed at various constant temperatures to see the influence on the deformation. A constant temperature is required, as the varying temperature induces heat flux into the system, resulting in unpredictable expansions and contractions in the adaptors. Apart from this, the vibration isolator is mounted on the engine oil reservoir, and is exposed to a constant, elevated temperature.

For the vertical experiments, the oven is equipped with several large metal blocks which are heated over a day. At a stable temperature, the LVDT is set to zero and the oven is switched off. The heated metal blocks act as thermodynamic capacitors and ensure a slow and steady decrease in temperature. By measuring the LVDT offset after the experiment, the metal expansion is calculated.

11.3 Identification Experiments

Mounting the vibration isolator in the vertical adaptor allows for characterisation of the dynamic behaviour in the thrust direction. The deflection in thrust direction shows the characteristics of a hysteresis. This is expected as the damping material is viscoelastic.

The first experiment is performed by looping through the mean load in steps of 500 *N*, where the force and displacement are constantly measured with 100 *Hz*. No additional vibrations are imposed on the mean load. This approach provides information about steps of 500 *N* in either direction. To improve the measurement approach, a random set of numbers with values between the lowest and highest expected thrust force are used as input. This ensures a large variety of step sizes and directions in the complete thrust range. By holding the force constant for several minutes, the settling characteristics or material creep are measured.

Further experiments are performed with sinusoidal shaped input waves to determine the dynamics of the vibration isolator with an unconventional shape. These experiments are used for model validation.

11.4 Conclusion

Two types of experiments are performed, characterisation and identification experiments. The first type of experiment is constructed to determine the environmental and operational conditions. To measure the influence of these environmental and operational conditions, the experiments are constructed such that only one parameter is excited or altered at a time. This allows to determine the influence of this individual parameter under the implied conditions.

Most of the characterisation experiments are performed in a horizontally mounted position. Because in the horizontally mounted experiment construction, the vibrations can be simulated at the same time as the thrust force. Only the temperature experiments are performed in the vertical mounting position. The identification experiments are all performed in the vertically mounted position, as this permits the use of the MTS test machine to simulate the thrust forces.

For the frequency experiments, it is assumed that the angle of the vibration is perpendicular to the thrust force. This reduction of dimension is assumed to not influence the results of this research. Similar assumptions are imposed for the mean load, as the dimension reduction is required to perform the experiments.

Chapter 12

Experiment Results

In this chapter, the results of the experiments are debated within particular the expected and unexpected results. The structure of the experiment results is the same as in chapter 11. The first section discusses the characterisation experiments where frequency and amplitude are combined in section 12.1.1. And, the influence of varying engine weight is discussed, followed by the influence of varying temperatures. The second section discusses the identification experiment results.

12.1 Characterisation Experiments

This approach is mainly used to determine the influence of the independent variables frequency, amplitude and mean load on isolator deformation. The influence of each individual parameter is investigated, assuming that two parameters without influence also do not influence the results when combined.

12.1.1 Vibrations

A vibration is a certain wave shape that, in general, has an amplitude and frequency. These parameters are closely related and therefore investigated in one test approach.

To show the influence of varying frequency and amplitude, experiments are performed with a constant thrust force and temperature. Figure 12.1 shows the influence of varying frequency, which is constructed by measuring the average deformation over a period of 60 seconds, where the largest dynamic amplitude of the LVDT is $2\mu m$. Each frequency sweep is performed with an increased amplitude varying from 0.02 to 0.04 mm. The mean load level in the showed figure is 6 kN at a temperature of 40 °C. No correlation between the frequency or amplitude changes and the measured deformation is noticed. At lower simulated thrust levels, a slightly larger noise level is found, which is again not visibly correlated with frequency or amplitude. Moreover, no influence of the nesting order of the frequency and amplitude variable is observed.

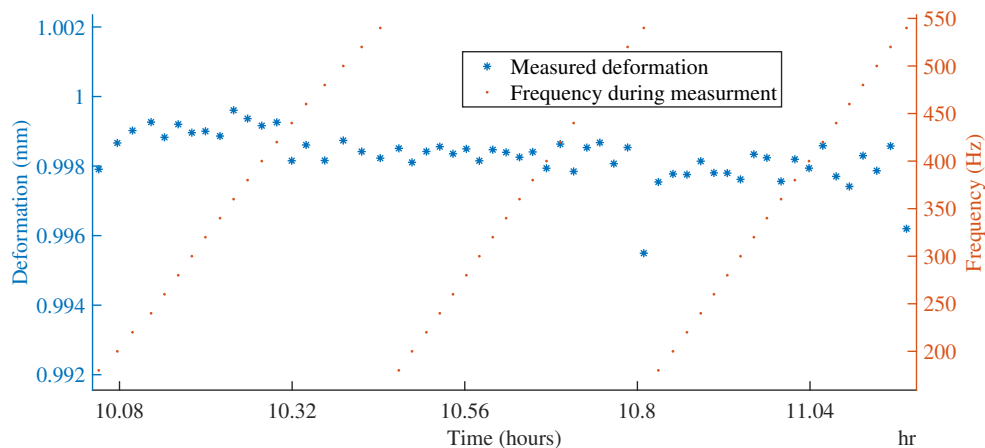


Figure 12.1: Influence of varying frequency and amplitude on the isolator deformation.

In the literature, it is found that the vibrations influence the stiffness of viscoelastic material in the direction of the vibration (Gent, 2012; Ward & Sweeney, 2004; Tanner, 2000). In this case, the stiffness is measured in a perpendicular plane and appears to be uninfluenced. For the concept of exploiting the vibration isolator as a thrust measurement device, this result is favourable. This reduces the complexity of the model with a large amount, as vibrations with the same frequency and amplitude do not necessarily have the same energy or acceleration and therefore are hard to correlate.

Sensors are sensitive to eigenfrequencies, which increase the noise and reduce the accuracy at certain frequencies. To investigate the influence of the vibration frequency on the sensors, a Fourier transform is calculated of the 60 seconds, which is used to calculate the mean values of the sensors. With this Fourier transform, which is recorded at 4000 Hz, the energy per frequency is determined.

Two approaches are used, the first test approach uses linear frequency steps, the second approach uses a random selection of prime numbers which are located in the frequency range. The number of measured frequencies per experiment is the same to enable a comparison of the measurements.

Load cell For the hydraulic cylinder load cell, the energy is located at the excitement frequency and according overtones. This is expected as the cylinder rod has a vibration dependent loading which is caused by the inertia of the cylinder. No high peaks at repeating frequencies are found, suggesting no excessive vibration takes place at eigenfrequencies.

The Fourier transforms of the prime numbers show similar results. One clear difference is the shape of the peaks of the excitation frequencies. The peaks that are observed in the prime number frequency excitations are wider spread in the frequency axis. This is caused by the nature of the Fourier transform as the frequency is reconstructed with only integer multiples of the lowest frequency that fits in the sample size. Since a prime number is per definition not a multiple of any lower integer, the frequency is reconstructed less accurate.

LVDT The frequency response of the LVDT only shows low energy frequency responses at frequency independent modes. The mode with the largest magnitude is observed at 250 Hz, other modes are observed at 700, 1200 and 1400 Hz. Since these modes are independent of the input frequency, natural frequencies are suspect of the observed response. Since the energy at these frequencies is low, it is assumed not to influence measurements. The fact that no energy is found at the excitation frequency indicates that the LVDT is mounted perpendicular to the vibration motion. The use of prime number excitation frequencies leads to no measurable difference on the thrust deformation, when compared to the linear stepped frequency.

12.1.2 Mean load

The mean load force simulates the engine weight during flight and is superimposed on the simulated engine vibrations. Figure 12.2 depicts an experiment where the mean load is applied. Note that the mean load, or engine weight, is perpendicular to the thrust force.

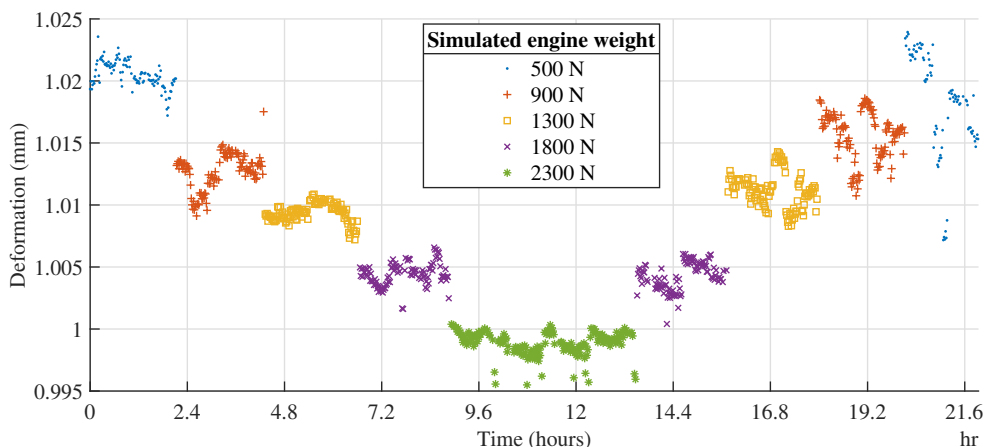


Figure 12.2: Shows the influence of varying mean load levels.

The influence of the varying mean load on the deformation, caused by a constant thrust force, is shown in fig. 12.2. In this figure, each colour represents a different mean load. A clear stepwise pattern is caused by the varying preload and affects the trust deformation reading with two hundredth of a millimetre. Increasing the mean load with 500 N results in a reduction of measured deformation of about $5\mu\text{m}$. This corresponds to a thrust measurement error of about 30 N at a maximum thrust force of 6 kN. As an example, a flight condition that results in twice the gravitational acceleration, causes a maximum measurement error of 1.6% when compared to a steady forward flight.

Figure 12.3 shows the simulated thrust force throughout the experiment. The increase of in the first few measurements is expected to be caused by a settling of the hydraulic cylinder seal force. Besides this initial increase, the thrust force is relatively constant. The previous section discussed the energy found at the excitation frequency of the Fourier transform. Which explains the slight variation of the measurements with varying frequencies. Each measurement point is an average of a 60 second recording, during which, all parameters are constant. The maximum variation of each sensor, during this period of time, is recorded. For the LVDT, the average of the maximum variation is $0.0746\mu\text{m}$, with a maximum variation of $1.1\mu\text{m}$ over the 21 hours of measurements. The variation of the load cell measurement is 27.02 N on average, with a maximum variation of 118 N. It is noticeable that the dynamic variation is strongly correlated to the applied frequency, and corresponds to the performed Fourier analysis on the sensor data.

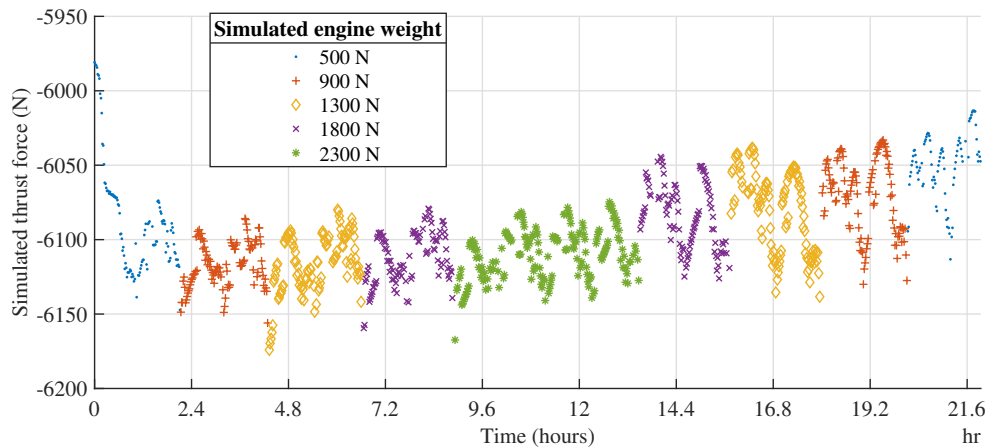


Figure 12.3: The simulated thrust force at various frequencies, amplitudes and mean loads.

12.2 Temperature

The LVDT measuring the position of the MTS cylinder is positioned outside the temperature control chamber. This results in a measurement offset, as the metal that connects the experiment specimen with the MTS machine contracts as the temperature decreases. Figure 12.4 displays the experiment with decreasing temperature and the influence of the contracting metal. The forces are the same for each cycle.

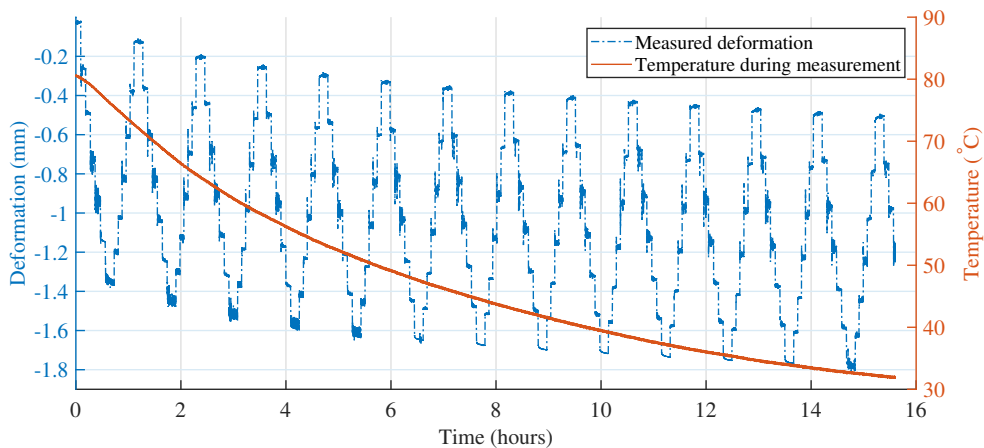


Figure 12.4: Temperature influence on measured deformation

By measuring the temperature and position difference at zero newtons, before, and after the experiment, the thermal expansion per degree Celsius is determined. Since the temperature flux is low, it is assumed that the expansion can be compensated with a linear function of 0.0095 mm per degree Celsius. Correcting the data with this linear relation results in fig. 12.5.

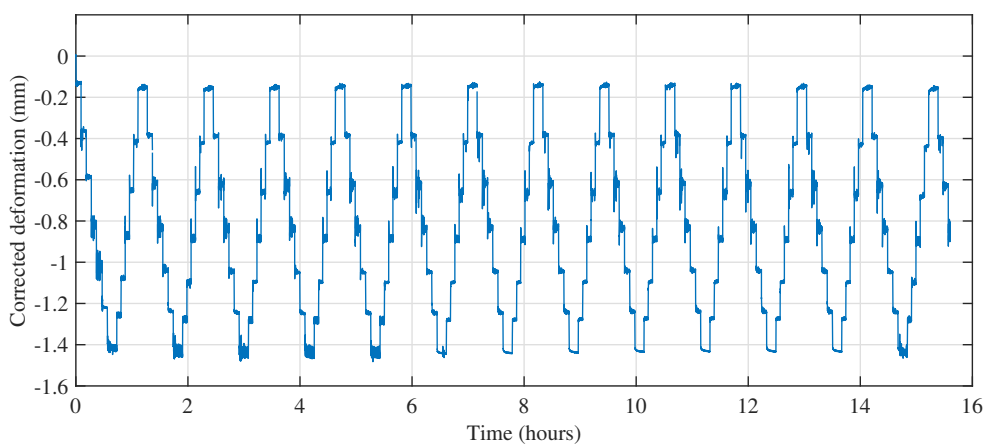


Figure 12.5: Linearly compensated deformation

The temperature influence on the characteristics is best observed in a force-deformation plot. Figure 12.6 depicts the force-deformation characteristics of the first and last full cycle. An important observation is the shape of the force-deformation curve, which is the same at different temperatures. This indicates that temperature variations have no measurable influence on the magnitude of deformation caused by the same force. The main reason for this is the material used in the vibration isolator, which is silicon rubber. This material is known for stable mechanical properties at varying temperatures. A further observation is a hysteresis, even though each step is static for ten minutes. This hysteresis is caused by the internal friction of the viscoelastic material.

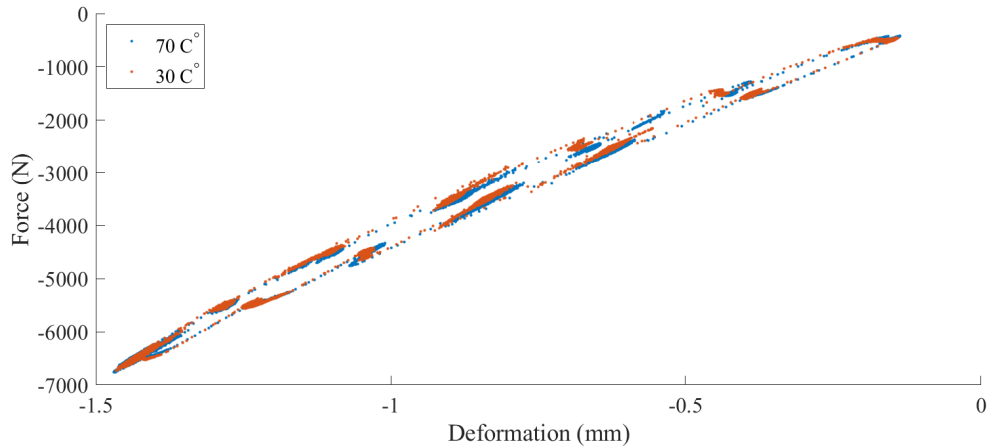


Figure 12.6: Engine vibration isolator characteristics at different temperatures

It is noticeable that the values that are found in this figure do not match the values found in figs. 12.2 and 12.3. This is caused by the fact that the LVDT of the MTS test machine is located in the hydraulic cylinder and therefore includes the strain of the adaptor, cylinder rod and the connections in between. This results in a larger strain reading when compared to the LVDT that measures the deformation of the isolator directly.

12.3 Identification Experiments

For the identification experiments, a test setup is used that facilitates vertical mounting of the vibration isolator. As a result, the thrust force can be simulated by the MTS test machine. The identification experiments are performed to capture the dynamic behaviour of throttle inputs that are expected during test flights. Overall, the throttle is adjusted in stepwise fashion. For this reason, the identification experiments are performed similarly. To map the hysteresis as realistic as possible, an experiment that steps through random values in the thrust range. This creates a map that covers the largest part of the hysteresis. Note that during the identification experiments, no additional engine vibration or preloads are simulated as the isolator is mounted vertically.

Additional experiments measure the response to slow sinusoidal shaped input waves, as shown in fig. 12.7. These unconventional shapes are used to evaluate the system dynamic response of the models that are constructed using the random step input data.

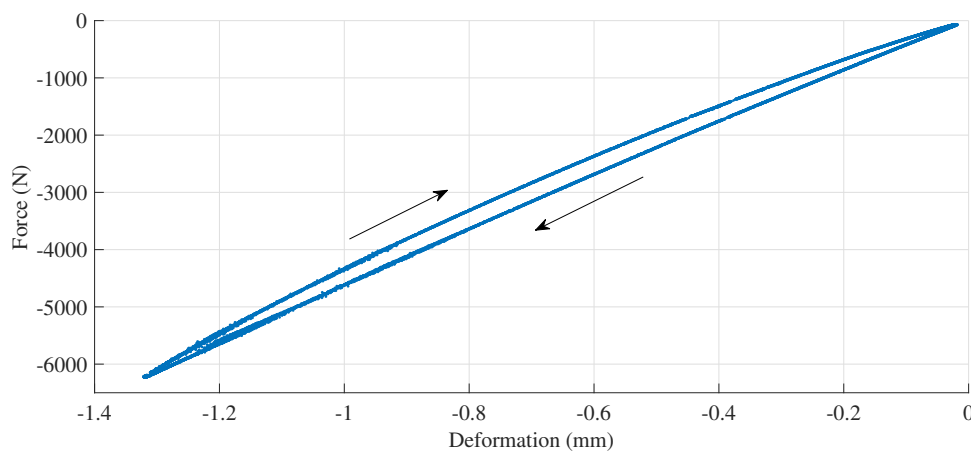


Figure 12.7: Force-deformation curve for sine input

12.4 Conclusion

With the characterisation experiments, it was found that the engine vibrations perpendicular to the thrust do not influence the magnitude of the measured deformation. This result is favourable for the concept of measuring thrust, as it reduces the complexity of the model.

During flight manoeuvres, the weight of the engine is not constant and is related to the directional accelerations. The mean load or simulated weight of the engine is found to have a measurable influence on the measured deformation of the vibration isolator due to the thrust force. It was found that each 500 *N* increase of engine weight, reduces the measured deformation with 5 μm , which corresponds to 30 *N* at maximum thrust force.

Temperature is known to influence the stiffness of general viscoelastic material. Therefore, an experiment is performed that evaluates the characteristics of the vibration isolator at different temperatures. The displacement sensor of this experiment is placed outside the temperature control chamber, and therefore the measurement includes the thermal material expansion and contraction of the components within the temperature control chamber. By linearly compensating for the measured expansion and temperature difference, it was found that the isolator characteristics are not influenced by temperature variations within the operational range. This is explained by the fact that for the damping material in the vibration isolator, a silicone rubber is used. The mechanical properties of silicone rubber are remarkably stable at varying temperatures.

The identification experiments are performed to be used as input for the thrust model generation. The aim of this model is to relate the measured deformation to the input force.

Chapter 13

Model Construction

This chapter elaborates on the different approaches to construct a model of the test object. A common approach to model elastomeric objects is defining the material properties using Dynamic Mechanical Analysis (DMA) in combination with the object geometry, which is the basis for a Finite Element Analysis (FEA) approach as described by Menard and Menard (2020); Sjöberg and Kari (2003); Sepe (1998). For this research, however, the interest is only a small, very specific part of the elastomeric characteristics. Namely, the deformation in one direction caused by a certain force. Furthermore, for real-time application method of thrust prediction, a system identification approach is much better than a finite element method (Zanette, 2016).

The first model approach is the physical modelling, resulting in so called white box models, and are based on Newton's and Hook's law. The second approach uses linear regression to fit a given curve structure to a set of input-output data. The third approach assumes the system can be modelled as an LTI system. The fourth and final approach is to assume a nonlinear dynamic model structure in the form of the Hammerstein or Wiener model, depending on the order of the linear dynamic and nonlinear static blocks

13.1 Physical Models

As mentioned in section 4.2.1, rubber like materials bear properties of both viscous liquids and elastic solids. Where ideal viscous liquids obey Newton's law and ideal linear elastic solids obey Hooke's law. Viscous liquids are modelled with a dashpot and elastic solids with a spring. Hence, viscoelastic material is modelled with a combination of dashpots and springs. Modelling and simulating systems that consist of real physical components such as springs and dashpots is called physical modelling. This approach results in a model where all parameters have a physical meaning, a so-called white-box model.

Placing a dashpot and spring in series is called the Maxwell model, and in parallel, it is called the Voigt model or Kelvin-Voigt model (Brinson & Brinson, 2015). The Maxwell model is used to model viscoelastic liquids and the Voigt model is used to model viscoelastic solids and are shown in fig. 13.1. The Voigt model predicts creep more realistically than the Maxwell model as the strain approaches a constant in infinite time. The Maxwell model predicts stress relaxation more realistically compared to the Voigt model (Lakes, 1999, p. 24).

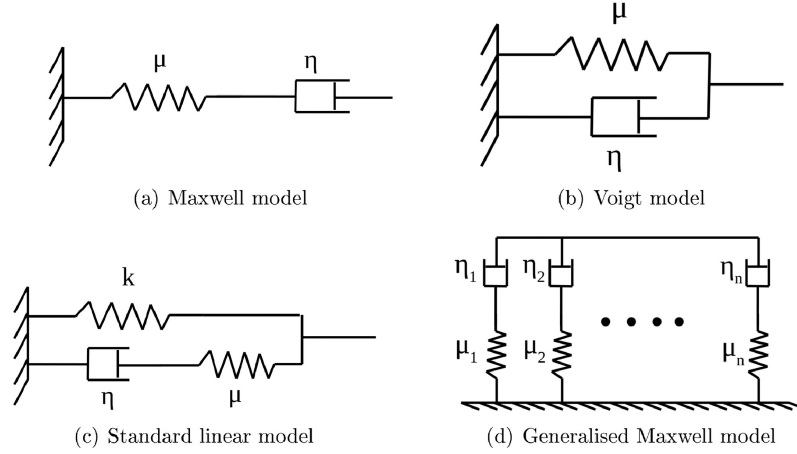


Figure 13.1: Static and dynamic representation of spring rate (Mukhopadhyay et al., 2019)

Expanding the Maxwell or Voigt model leads to a three-element model or a so-called Standard Linear Solid (SLS) or Zener model. Experimental evidence shows a distribution of relaxation times that are discrete or continuous. Therefore, models that are based on experimental data use multiple Maxwell models in parallel to reduce the model error. This is also called the Generalised Maxwell Model (GMM) (Riande et al., 2000). The negative effect of adding more Maxwell models together is the resulting complex model with more parameters to estimate.

13.1.1 Maxwell Model

One of the simplest methods to describing the behaviour of viscoelastic material is the Maxwell model. The model consists of a spring with modulus E and a dashpot with viscosity η , which are placed in series. This Maxwell element describes a first-order differential equation of the stress and strain. The representation of the Maxwell model is shown in fig. 13.2, and the general solution is given in eq. (13.1).



Figure 13.2: Maxwell model (Schreurs, 2012)

$$\varepsilon = \varepsilon_E + \varepsilon_\eta \quad \rightarrow \quad \dot{\varepsilon} = \dot{\varepsilon}_E + \dot{\varepsilon}_\eta = \frac{\dot{\sigma}}{E} + \frac{\sigma}{\eta} \quad (13.1)$$

For step excitations of stress and strain, the differential equation of the Maxwell model is solved as shown in eq. (13.2). Here, the Heaviside function $H(t,0)$ and creep function $D(t)$ are implemented.

$$\begin{aligned} \text{stress step} \quad : \quad \sigma(t) &= \sigma_0 H(t,0) \quad \rightarrow \quad \dot{\sigma}(t) = \sigma_0 \delta(t,0) \quad \rightarrow \quad \text{creep} \\ \dot{\varepsilon}(t) &= \frac{\sigma_0}{E} \delta(t,0) + \frac{\sigma_0}{\eta} \\ \varepsilon(t) &= \frac{\sigma_0}{E} H(t,0) + \frac{\sigma_0}{\eta} t = \sigma_0 \left[\frac{1}{\eta} \left(t + \frac{\eta}{E} \right) \right] = \sigma_0 D(t) \end{aligned} \quad (13.2)$$

$$\begin{aligned} \text{strain step} \quad : \quad \varepsilon(t) &= \varepsilon_0 H(t,0) \quad \rightarrow \quad \dot{\varepsilon}(t) = \varepsilon_0 \delta(t,0) \quad \rightarrow \quad \text{relaxation} \\ \sigma(t) &= \varepsilon_0 E e^{-\frac{E}{\eta} t} = \varepsilon_0 E e^{-\frac{t}{\tau_m}} = \varepsilon_0 E(t) \end{aligned} \quad (13.3)$$

13.1.2 Kelvin-Voigt Model

The Kelvin-Voigt model contains the same components as the Maxwell model, yet ordered in a parallel construction, as shown in fig. 13.3.

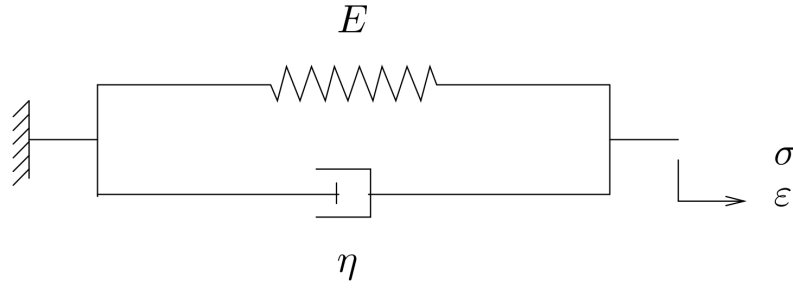


Figure 13.3: Kelvin-Voigt model (Schreurs, 2012)

$$\sigma = \sigma_E + \sigma_\eta = E\varepsilon + \eta\dot{\varepsilon} \quad (13.4)$$

As mentioned, the Kelvin-Voigt model is a viscoelastic solid model, meaning that the strain response to a step excitation of stress describes viscoelastic behaviour, characterised by the time constant $\tau = \frac{\eta}{E}$ [s].

$$\sigma(t) = \sigma_0 H(t, 0) \quad \rightarrow \quad \dot{\sigma}(t) = \sigma_0 \delta(t, 0) \quad \rightarrow \quad \text{creep} \quad (13.5)$$

$$\left. \begin{aligned} \eta\dot{\varepsilon}(t) + E\varepsilon(t) &= \sigma(t) = \sigma_0 H(t, 0) \\ \varepsilon(t) &= \varepsilon_H(t) + \varepsilon_P = C e^{-\frac{E}{\eta}t} + \frac{\sigma_0}{E} \\ \varepsilon(t=0) &= 0 \end{aligned} \right\} \rightarrow C = -\frac{\sigma_0}{E} \quad (13.6)$$

$$\varepsilon(t) = \frac{\sigma_0}{E} \left[1 - e^{-\frac{E}{\eta}t} \right] = \sigma_0 D(t)$$

A stepwise strain excitation leads to infinite stress.

$$\begin{aligned} \varepsilon(t) &= \varepsilon_0 H(t, 0) \quad \rightarrow \quad \dot{\varepsilon}(t) = \varepsilon_0 \delta(t, 0) \quad \rightarrow \quad \text{relaxation} \\ \sigma(t) &= E\varepsilon(t) + \eta\dot{\varepsilon}(t) \\ \sigma(t) &= E\varepsilon_0 + \eta\varepsilon_0 \delta(t, 0) = \varepsilon_0 [E + \eta\delta(t, 0)] = \infty \end{aligned} \quad (13.7)$$

The Maxwell and Kelvin-Voigt models are the basis for a large group of models that add components to approach a certain type of elastomer more accurately. The addition of friction components enables the simulation of the hysteresis as described by Lion (1997). With the generalised models, a larger quantity of Maxwell or Kelvin-Voigt models are placed in parallel or series, respectively. By using parameter estimation, the generalised model is fitted to the measurement data (Baz, 2019). Note that these models only include one dimension and are only capable to model one particular aspect of viscoelastic materials. Therefore, a more suitable approach to model the magnitude of the independent variables on the dependent variable is discussed in the following section.

13.2 Static Nonlinear Models

One of the simplest modelling approaches is fitting a line function through the given data set. By adjusting the parameters of the line function, the line is shaped till it fits the data with the least sum of squares. Similarly, it is possible to fit the data to a linear line. Common are the polynomial, power, or exponential functions to approximate static nonlinear systems.

According to Morelli and Klein (2016), no uncertainty models for θ and v are used for specifying the form of the least-squares model, i.e., there are no probability statements concerning θ and v . An estimate for the least-squares model can be obtained by the reasoning that, given z , the "best" estimate of θ comes from minimising the weighted sum of squared differences between the measured outputs and the model outputs:

$$J(\theta) = \frac{1}{2} (z - H\theta)^T R^{-1} (z - H\theta) \quad (13.8)$$

where \mathbf{R}^{-1} is now a positive definite weighting matrix, chosen by judgement. Optimisation of the preceding $J(\boldsymbol{\theta})$ leads to the well-known Weighted Least Squares (WLS) estimator. In the special case where $\mathbf{R} = \mathbf{I}$, the Ordinary Least Squares (OLS) estimator is obtained, with cost function:

$$J(\boldsymbol{\theta}) = \frac{1}{2}(\mathbf{z} - \mathbf{H}\boldsymbol{\theta})^T(\mathbf{z} - \mathbf{H}\boldsymbol{\theta}) \quad (13.9)$$

Considering the entire set of measured data $\mathbf{z}(i), i = 1, 2, \dots, N$, the OLS estimator for a scalar measurement is obtained by minimising:

$$J(\boldsymbol{\theta}) = \frac{1}{2} \sum_{i=1}^N [z(i) - \mathbf{h}(i, \boldsymbol{\theta})]^2 \quad (13.10)$$

13.2.1 Define a Linear Regression Model

For this experiment, the effect of certain parameter changes on the deflection caused by the thrust force needs to be modelled. A static approach is exploited before more complex dynamic models are investigated.

The linear regression model that best fits a sequence of measurements y is defined as follows:

$$y = A(x) \cdot \boldsymbol{\theta} + \varepsilon \quad (13.11)$$

where

$$\begin{aligned} y &= \text{the } N \times 1 \text{ measurement vector} \\ A(x) &= \text{the } N \times n \text{ regression matrix} \\ x &= \text{the } m \times 1 \text{ state vector} \\ \boldsymbol{\theta} &= \text{the } n \times 1 \text{ parameter vector} \\ \varepsilon &= \text{the } N \times 1 \text{ model residual vector} \end{aligned} \quad (13.12)$$

The most widely used regression matrix is the polynomial structure. In that case $p_m(x(n))$ are ordinary polynomials in terms of x :

$$A(x) = \begin{bmatrix} 1 & x_i(1) & x_i^2(1) & \cdots & x_i^n(1)x_j^m(1) & \cdots & x_k^M(1) \\ 1 & x_i(2) & x_i^2(2) & \cdots & x_i^n(2)x_j^m(2) & \cdots & x_k^M(2) \\ \vdots & \vdots & \vdots & \vdots & \vdots & \vdots & \vdots \\ 1 & x_i(N) & x_i^2(N) & \cdots & x_i^n(N)x_j^m(N) & \cdots & x_k^M(N) \end{bmatrix} \quad (13.13)$$

Note that cross-terms are required in multivariate models. For the regression model, a polynomial model structure is a suitable choice to start with. The structure of $A(x)\boldsymbol{\theta}$ is as follows:

$$A(x) \cdot \boldsymbol{\theta} = \theta_0 + \theta_1 x + \theta_2 x^2 \quad (13.14)$$

where $\theta_0, \theta_1, \theta_2$ are the unknown model parameters. The linear regression model now is:

$$y = [1 \quad x \quad x^2] \cdot \begin{bmatrix} \theta_0 \\ \theta_1 \\ \theta_2 \end{bmatrix} + \varepsilon \quad (13.15)$$

with the linear regression residual ε given as:

$$\varepsilon = y - A(x) \cdot \boldsymbol{\theta} \quad (13.16)$$

and the linear regression estimator $\hat{\boldsymbol{\theta}}$ given as:

$$\begin{aligned} \hat{\boldsymbol{\theta}} &= \arg \min J(y - A(x) \cdot \boldsymbol{\theta}) \\ &= \arg \min J(\varepsilon) \end{aligned} \quad (13.17)$$

Here J is a cost function which is used to minimise the error of a model with respect to the data. This function sums all error values ε for all values of x in a given set of parameters θ . Some examples of cost functions are:

$$\begin{aligned}
 J(x, \theta) &= \sum_{i=1}^N \varepsilon_i = \sum_{i=1}^N y_i - A(x_i) \cdot \theta, & (\text{linear}) \\
 J(x, \theta) &= \sum_{i=1}^N \varepsilon_i^2 = \sum_{i=1}^N (y_i - A(x_i) \cdot \theta)^2, & (\text{quadratic}) \\
 J(x, \theta) &= \sum_{i=1}^N |\varepsilon_i| = \sum_{i=1}^N |y_i - A(x_i) \cdot \theta|, & (\text{absolute value}) \\
 J(x, \theta) &= \sum_{i=1}^N W_{ii} \varepsilon_i^2 = \sum_{i=1}^N (y_i - A(x_i) \cdot \theta) \cdot W \cdot (y_i - A(x_i) \cdot \theta), & (\text{Weighted quadratic})
 \end{aligned} \tag{13.18}$$

Note that a linear cost function is useless, as positive and negative errors can even each other out.

Least Squares Estimator Instead of minimising the errors directly, it is also possible to minimise the squares of the errors. To construct the least squares estimator or sometimes referred to as Ordinary Least Squares (OLS), the convex quadratic cost function is used as basis:

$$J(x, \theta) = \sum_{i=1}^N \varepsilon_i^2 = \sum_{i=1}^N (y_i - A(x_i) \cdot \theta)^2 \tag{13.19}$$

Using matrix notation, this becomes:

$$J(x, \theta) = \varepsilon^T \varepsilon = (y - A(x) \cdot \theta)^T (y - A(x) \cdot \theta) \tag{13.20}$$

The least squares estimator is the solution to the optimisation problem:

$$\hat{\theta} = \arg \min \varepsilon^T \varepsilon \tag{13.21}$$

This convex cost function has a minimum when:

$$\frac{\partial J(x, \theta)}{\partial \theta} = \frac{\partial \varepsilon^T \varepsilon}{\partial \theta} = 0 \tag{13.22}$$

The partial derivative with respect to θ of the quadratic cost function is:

$$\begin{aligned}
 \frac{\partial \varepsilon^T \varepsilon}{\partial \theta} &= 2\varepsilon^T \frac{\partial \varepsilon}{\partial \theta} \\
 &= 2(y - A(x) \cdot \theta)^T \cdot -A(x) = 0
 \end{aligned} \tag{13.23}$$

By introducing $\hat{\theta}$ as the particular value for θ , the cost function is minimised. Dividing this equation by -2 results in the following equation:

$$(y - A(x) \cdot \hat{\theta})^T \cdot A(x) = 0 \tag{13.24}$$

Transposing this, results in:

$$A^T(x)(y - A(x) \cdot \hat{\theta}) = 0 \tag{13.25}$$

Expanding the term in brackets and isolating $\hat{\theta}$ gives:

$$\hat{\theta} = \left(A^T(x) \cdot A(x) \right)^{-1} A^T(x) \cdot y \tag{13.26}$$

Which is the Ordinary Least Squares (OLS) estimator for $\hat{\theta}$. According to Paoletta (2019), $\hat{\theta}_{OLS}$ has the smallest variance among all linear unbiased estimators; this result is often referred to as the Gauss–Markov

Theorem and expressed as saying that $\hat{\theta}_{OLS}$ is the best linear unbiased estimator, or BLUE. And can be proved accordingly.

For an unbiased estimator, the following must hold:

$$B\{\hat{\theta}\} = E(\hat{\theta}) - \theta = 0 \quad (13.27)$$

with $B\{\hat{\theta}\}$ as the estimator bias, and with θ as the true parameter.

By writing the estimated parameters in terms of true parameters and residuals, the bias of the estimated parameters can be checked:

$$\begin{aligned} \hat{\theta}_{OLS} &= \left(A^T(x) \cdot A(x) \right)^{-1} A^T(x) \cdot y \\ &= \left(A^T(x) \cdot A(x) \right)^{-1} A^T(x) \cdot (A(x)\theta + \varepsilon) \\ &= \left(A^T(x) \cdot A(x) \right)^{-1} A^T(x)A(x) \cdot \theta + \left(A^T(x) \cdot A(x) \right)^{-1} A^T(x) \cdot \varepsilon \\ &= \theta + \left(A^T(x) \cdot A(x) \right)^{-1} A^T(x) \cdot \varepsilon \end{aligned} \quad (13.28)$$

Taking the expectancy of left and right hand terms results in:

$$E\{\hat{\theta}_{OLS}\} = E\{\theta\} + \left(A^T(x) \cdot A(x) \right)^{-1} A^T(x) \cdot E\{\varepsilon\} \quad (13.29)$$

This clearly indicates an unbiased estimator if $E\{\hat{\theta}_{OLS}\} = E\{\theta\}$ which implies $E\{\varepsilon\} = 0$. Hence, all least squares estimators assume $E\{\varepsilon\} = 0$.

Besides the OLS estimation method, several other methods like Generalised Least Squares (GLS) or Maximum Likely Estimation (MLE) are suited to estimate the parameters of the polynomial model. The resulting model is a purely static, third order polynomial that fits the stress-strain curve with the least squared error. No dynamic behaviour is included in this model. Hence, no time input is required.

13.3 Linear Dynamic Models

This section discusses the dynamic linear models within particular the time-series models. Linear dynamic systems are systems whose outputs depend linearly on their inputs. Two main model structures are used in the transfer-function approach, namely the common equation error model structure and the output error model structure.

13.3.1 Equation Error Model

One of the simplest input-output relations is obtained by the following linear difference equation:

$$\begin{aligned} y(k) + f_1y(k-1) + \dots + f_{n_u}y(t-n_f) \\ = b_1u(k-1) + \dots + b_{n_b}u(t-n_b) + e(k) \end{aligned} \quad (13.30)$$

The name *equation error model* comes from the white noise term $e(k)$ that enters the difference equation as a direct error (Keesman, 2011). The to be estimated parameters are in this case:

$$\theta = \square^T \quad (13.31)$$

By introducing:

$$F(q) = 1 + f_1q^{-1} + \dots + f_{n_u}q^{-n_f} \quad (13.32)$$

and:

$$B(q) = b_1q^{-1} + \dots + b_{n_b}q^{-n_b} \quad (13.33)$$

it is found that:

$$G(q, \theta) = \frac{B(q)}{F(q)}, \quad H(q, \theta) = \frac{1}{F(q)} \quad (13.34)$$

correspond with the general model equation:

$$y(k) = G(q, \theta)u(k) + H(q, \theta)e(k) \quad (13.35)$$

The model presented here is called an ARX model. Where autoregression part $F(q)y(k)$ makes the AR and the extra input $B(q)u(k)$ (commonly called exogenous in econometrics) the X of the abbreviation (Ljung, 1999). The notation q which denotes the forward shift operator is rather confusing, as it would intuitively be q^{-1} . The denotation is chosen to be in formal agreement with z-transform and Fourier-transform expressions (Ljung, 1999, p 25).

The disadvantage of ARX models is the lack of freedom in describing the properties of the disturbance term. By describing the white noise as a moving average $C(q)$, flexibility is added to the model and gives:

$$\begin{aligned} y(k) + f_1y(k-1) + \dots + f_{n_f}y(t-n_f) &= b_1u(k-1) + \dots \\ &+ b_{n_b}u(t-n_b) + e(k) + c_1e(k-1) + \dots + c_{n_c}e(t-n_c) \end{aligned} \quad (13.36)$$

with:

$$C(q) = 1 + c_1q^{-1} + \dots + c_{n_c}q^{-n_c} \quad (13.37)$$

it is rewritten as:

$$F(q)y(k) = B(q)u(k) + C(q)e(k) \quad (13.38)$$

which clearly corresponds to the general model equation eq. (13.35) with:

$$G(q, \theta) = \frac{B(q)}{A(q)}, \quad H(q, \theta) = \frac{C(q)}{F(q)} \quad (13.39)$$

with:

$$\theta = [f_1 \dots f_{n_f} b_1 \dots b_{n_b} c_1 \dots c_{n_c}]^T \quad (13.40)$$

This is the so called ARMAX model with MA for moving average part $C(q)e(k)$.

13.3.2 Output Error Model

Output-error (OE) models differ from the equation error models as it is assumed that the noise is added to the output and has no interference with the estimation process. This allows for a more realistic model and often perform better than equation error models (Nelles, 2021). Because the noise is not included in the system dynamics $\frac{1}{F(q)}$, the model is nonlinear in the parameters resulting in a pseudo-linear model which is harder to estimate.

Ljung supposes that the relation of the input and undisturbed output w can be written as a linear equation and, the disturbances is white measurement noise, the input output relation is as follows:

$$\begin{aligned} w(k) + f_1w(k-1) + \dots + f_{n_f}w(t-n_f) \\ = b_1u(k-1) + \dots + b_{n_b}u(t-n_b) \end{aligned} \quad (13.41)$$

and:

$$y(k) = w(k) + e(k) \quad (13.42)$$

with:

$$F(q) = 1 + f_1q^{-1} + \dots + f_{n_f}q^{-n_f} \quad (13.43)$$

$$B(q) = 1 + b_1q^{-1} + \dots + b_{n_b}q^{-n_b} \quad (13.44)$$

The model reduces to:

$$y(k) = \frac{B(q)}{F(q)}u(k) + e(k) \quad (13.45)$$

The to be determined parameter vector is:

$$\theta = [b_1 \quad b_2 \dots b_{n_b} f_1 \quad f_2 \dots f_{n_f}]^T \quad (13.46)$$

Since $w(k)$ in eq. (13.41) is never observed, it should carry an index θ , as it is constructed from u using eq. (13.42). Which results in:

$$\begin{aligned} w(t, \theta) + f_1 w(t-1, \theta) + \dots + f_{n_f} w(t-n_f, \theta) \\ = b_1 u(k-1) + \dots + b_{n_b} u(t-n_b) \end{aligned} \quad (13.47)$$

comparing this with general model description:

$$y(k) = G(q, \theta)u(k) + H(q, \theta)e(k) \quad (13.48)$$

it is found that $H(q \cdot \theta) = 1$, resulting in the natural predictor where $\hat{y}(t | \theta)$ is constructed from past inputs only:

$$\hat{y}(t | \theta) = \frac{B(q)}{F(q)}u(k) = w(t, \theta) \quad (13.49)$$

Using vector

$$\varphi(t, \theta) = [u(k-1) \dots u(t-n_b) - w(t-1, \theta) \dots - w(t-n_f, \theta)]^T \quad (13.50)$$

Which is rewritten as

$$\hat{y}(t | \theta) = \varphi^T(t, \theta)\theta \quad (13.51)$$

which is similar to linear regression. However, the equation itself is no linear regression, due to the nonlinear effect of θ in the vector $\varphi(t, \theta)$. Hence, it is called pseudolinear regression. Note that the output error model predictor is unstable if $F(q)$ polynomial is unstable. Therefore it is not possible to model an unstable process with any output error model.

A natural development of the output error model is to include the modelling of the output error properties. This is called the Box-Jenkins (BJ) model structure.

13.4 Nonlinear Models

If both the linear dynamic model and static nonlinear model do not yield satisfactory performances, nonlinear dynamic models are a natural next step. The first approach is an expansion of the linear dynamic autoregression models using the Kolmogorov-Gabor approach. This is followed by the block-orientated approach which combines a static nonlinear model and a linear dynamic output error model. A static nonlinear model can fit a nonlinear function through a data set, on the other hand, it can also fit the nonlinear data to a linear function. Using a static nonlinear model to generate "linear data" allows a dynamic linear model to estimate the system dynamics.

The Kolmogorov-Gabor models apply generalised polynomial models to the representation of nonlinear dynamic systems (Nelles, 2021; Janczak, 2004).

$$y(n) = f(u(n-1), \dots, u(n-n_b), y(n-1), \dots, y(n-na)) + \varepsilon(n) \quad (13.52)$$

resulting in:

$$\begin{aligned} y(n) = a_0 + \sum_{i_1=1}^{nab} a_{i_1} x_{i_1}(n) + \sum_{i_1=1}^{nab} \sum_{i_2=1}^{i_1} a_{i_1 i_2} x_{i_1}(n) x_{i_2}(n) \\ + \dots + \sum_{i_1=1}^{nab} \sum_{i_2=1}^{i_1} \dots \sum_{i_{l-1}=1}^{i_{l-2}} a_{i_1 i_2 \dots i_l} x_{i_1}(n) x_{i_2}(n) \dots x_{i_l}(n) + \varepsilon(n) \end{aligned} \quad (13.53)$$

where $nab = na + nb$,

$$x_j(n) = \begin{cases} u(n-j) & \text{if } 1 \leq j \leq nb \\ y(n-j+nb) & \text{if } nb < j \leq nab. \end{cases} \quad (13.54)$$

The number of parameters M in eq. (13.53) increases strongly as nab or l grow:

$$M = \frac{(l+nab)!}{l!nab!} \quad (13.55)$$

The large model complexity of the Kolmogorov-Gabor model restricts its practical applicability and leads to reduced polynomial models containing only selected terms of eq. (13.53)(Janczak, 2004). Note that eq. (13.53) has the nonlinear autoregressive with exogenous input (NARX) structure. The other nonlinear variants of previously mentioned structures such as NARX, NARMAX and NBJ are obtained via a relevant redefinition of $x_j(n)$. With these models, some limitations arise for processes with non-unique nonlinearities such as hysteresis and backlash, where internal non-measurable states play a decisive role and partly for processes with non-invertible nonlinearities (Nelles, 2021).

Combining a static nonlinear model as discussed in section 13.2, and a linear dynamic model as discussed in section 13.3 results in the so called Hammerstein and Wiener models. Where the first one was introduced by and named after the German mathematician Hammerstein (1930). This model places a static nonlinear model before the dynamic linear model, as shown in fig. 13.4. A permutation of the static nonlinear and linear dynamic model results in the Wiener system, which is named after the MIT professor Wiener and Teichmann (1959). Hammerstein and Wiener models allow for high accuracy approximations of nonlinear dynamic models (S. Boyd & Chua, 1985)

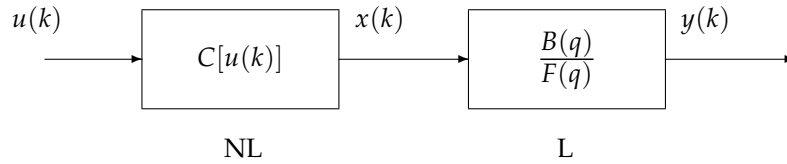


Figure 13.4: Hammerstein model

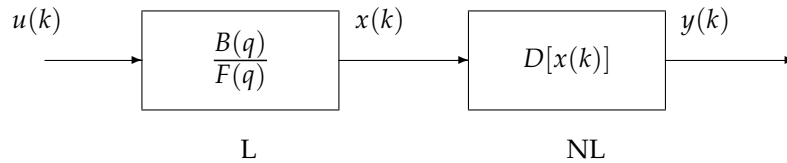


Figure 13.5: Wiener model

Combining a Hammerstein and a Wiener model respectively results in the so called Hammerstein-Wiener model and is shown in fig. 13.6. Inverting the order of the models naturally leads to the so called Wiener-Hammerstein model structure, and is shown in (fig. 13.7). These model structures allow for better modelling when both actuator and sensor nonlinearities are present (Er-Wei Bai, 2010).

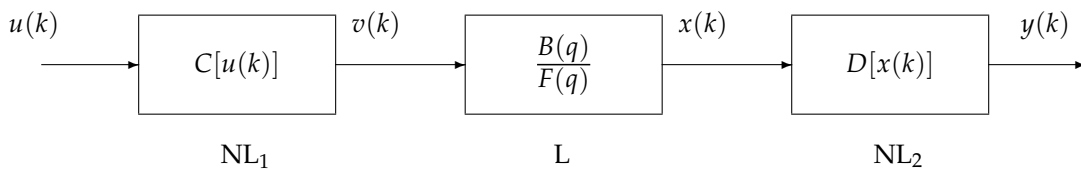


Figure 13.6: Hammerstein-Wiener model

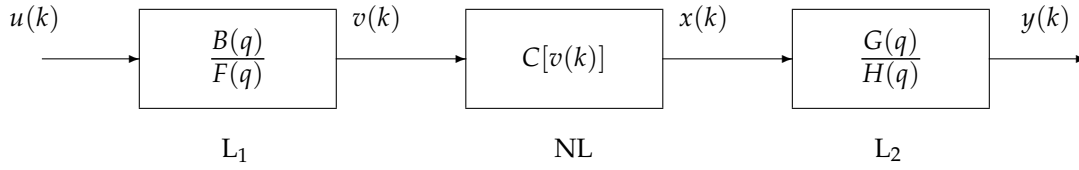


Figure 13.7: Wiener-Hammerstein model

13.4.1 Decomposition of Block-oriented Nonlinear Systems

For a better understanding of the mathematical approach to combine static nonlinear and dynamic linear models, this section is created. Starting with the Hammerstein and Wiener models, followed by the Hammerstein-Wiener model in combination with a piecewise-linear nonlinearity approximation.

Hammerstein System The Hammerstein system is a cascade connection of a nonlinear static subsystem

$$x(k) = C[u(k)] \quad (13.56)$$

where $u(k)$ are the inputs and $x(k)$ are the outputs and $C[\cdot]$ is the nonlinear static block mapping as shown in fig. 13.4. The following linear dynamic subsystem is described by:

$$y(k) = \frac{B(q)}{F(q)}x(k) \quad (13.57)$$

where

$$\begin{aligned} F(q) &= f_1q^{-1} + \dots + f_mq^{-m} \\ B(q) &= b_1q^{-1} + \dots + b_nq^{-n} \end{aligned} \quad (13.58)$$

and $x(k)$ and $y(k)$ are the inputs and outputs, respectively, and q^{-d} represents the pure time delay of the system. Now the Hammerstein system output equation is written as

$$y(k) = B(q)x(k) - F(q)y(k). \quad (13.59)$$

In the next step the key term separation principle is used (Vörös, 1995, 1997a). Meaning that two mappings α and β with the domain X will exist for the mapping g such that in the additive case:

$$g(x) = \alpha(x) + \beta(x) \quad (13.60)$$

while in the multiplicative case:

$$g(x) = \alpha(x) \cdot \beta(x) \quad (13.61)$$

for every $x \in X$. Note that in the case of analytic mappings such decomposition forms always exist (Er-Wei Bai, 2010). Using the key term separation principle, separating the term containing variable $x(k)$ gives:

$$y(k) = b_1x(k) + [B(q) - b_1]x(k) - F(q)y(k) \quad (13.62)$$

substituting eq. (13.56) only for the key term gives:

$$y(k) = C[u(k)] + [B(q) - 1]x(k) - F(q)y(k) \quad (13.63)$$

assuming $b_1 = 1$. If the nonlinear static function is multiplied by a non-zero real constant and the linear dynamic part is divided by the same constant, the input-output behaviour is unchanged. By choosing the parametrisation $C[\cdot]$ such that the system is linear in parameters, the output equation has separable parameters and the equation becomes linear in parameters and nonlinear in variables. Different types of nonlinearities are available, i.e. polynomial, discontinuous, multisegment piecewise linear. The parameters are then solved as quasi-linear by iterative methods with internal variable estimations.

Wiener System Similarly, the Wiener system is decomposed. The Wiener system is a cascade connection of a linear dynamic subsystem

$$x(k) = B(q)u(k) - F(q)x(k) \quad (13.64)$$

with the inputs $u(k)$ and the outputs $x(k)$, where $F(q)$ and $B(q)$ are given by eq. (13.58), followed by a nonlinear static subsystem:

$$y(k) = D[x(k)] \quad (13.65)$$

where $x(k)$ is the input and $y(k)$ is the output as shown in fig. 13.5. Separating the key term gives:

$$y(k) = d_1x(k) + D[x(k)] \quad (13.66)$$

With the assumption that $d_1 = 1$, eq. (13.64) is half-substituted for the key term which gives:

$$y(k) = B(q)u(k) - F(q)x(k) + D[x(k)] \quad (13.67)$$

Choosing the parametrisation for $D[.]$ being linear in parameters, the Wiener system is described by the output equation, which is again linear in all the separate parameters and nonlinear in variables. The output nonlinearities can be described similarly to the Hammerstein system.

Hammerstein-Wiener System The Hammerstein-Wiener system is a cascade connection of a static nonlinear input block (NL_1), a linear dynamic system (LS) and a static nonlinear output block (NL_2). The first block is described as:

$$v(k) = C[u(k)] \quad (13.68)$$

here, $u(k)$ is the input, $v(k)$ is the output, and $C[.]$ is the nonlinear static block mapping as shown in fig. 13.6. The linear block difference equation is given as:

$$x(k) = B(q)v(k) - F(q)x(k) \quad (13.69)$$

here, $v(k)$ is the input and $u(k)$ is the output. $F(q)$ and $B(q)$ are scalar polynomials in the forward shift operator q

$$\begin{aligned} F(q) &= f_1q^{-1} + \dots + f_mq^{-m} \\ B(q) &= b_1q^{-1} + \dots + b_nq^{-n} \end{aligned} \quad (13.70)$$

The second nonlinear static block (NL_2) is described as

$$y(k) = D[x(k)] \quad (13.71)$$

The system input $u(k)$ and output $y(k)$ are measurable and the internal variables $v(k)$ and $x(k)$ are not measurable. To reduce the nonlinearity of the system and allow for parameter estimation, a serial decomposition is used to derive a simpler form of the system description. This is the key term separation principle, applied multiple times within a compound mapping (Vörös, 1995, 1997b, 2005). Note that in the case of analytic mappings such decomposition forms always exist (Er-Wei Bai, 2010). The decomposition of the second nonlinear block (NL_2) is formulated as

$$y(k) = d_1x(k) + D[x(k)] \quad (13.72)$$

with a separated internal variable $x(k)$, the linear dynamic lock equation is written as

$$x(k) = b_1v(k-1) + [B(q) - b_1]v(k-1) - F(q)x(k) \quad (13.73)$$

with the internal variable $v(k-1)$ separated. Completing the serial decomposition results in the following output equation of the Hammerstein-Wiener system

$$y(k) = d_1 \{b_1C[u(k-1)] + [B(q) - b_1]v(k-1) - F(q)x(k)\} + D[x(k)] \quad (13.74)$$

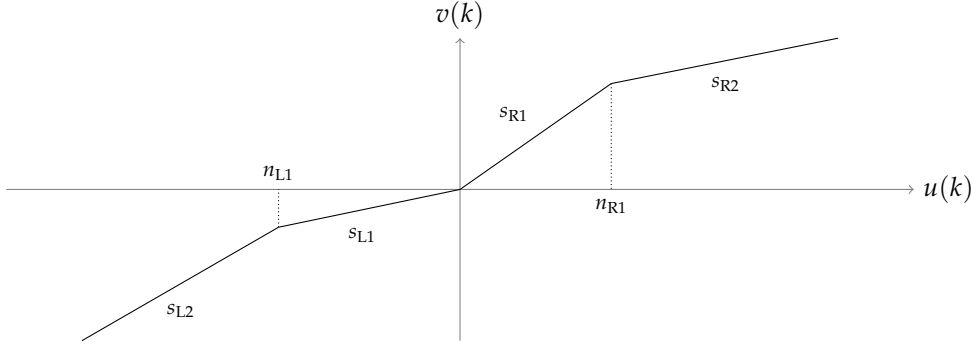


Figure 13.8: Four segment piecewise-linear nonlinearity model representation of the first nonlinear block NL_1

13.4.2 Piecewise-linear

To model the nonlinearity of the static nonlinear blocks NL_1 and NL_2 , several approaches are possible. For the engine vibration isolator which is used for the experiments, a 3th order polynomial sufficed. However, to pursue a generic model, a piecewise-linear nonlinearity approximation is implemented, which allows for a more robust and future proof approach. Since the model is purposed for a practical application, the adaption of a piecewise-linear approach is implemented to allow for modelling of backlash or discontinuities that for example are caused by play in the mounting system (Vörös, 2003, 2001, 1997b).

A piecewise-linear approach divides the input range into a predefined amount of segments, in which the nonlinearity is approximated with a linear function. Increasing the amount of segments results in a higher resolution of the system nonlinearity representation.

In the pursuit of a parsimonious model, piecewise-quadratic systems are not implemented, since piecewise-linear systems analyse smooth nonlinear dynamics with arbitrary accuracy (Rantzer, 2000). Furthermore, the piecewise-linear approach includes capabilities to model backlash or discontinuities that for example are caused by play in the mounting system (Vörös, 2003, 2001, 1997b).

In a four segment piecewise-linear static block NL_1 as shown in fig. 13.8, the output $v(k)$ is described as:

$$v(k) = \begin{cases} s_{R1}u(k) & \text{if } 0 \leq u(k) \leq n_{R1} \\ s_{R2}[u(k) - n_{R1}] + s_{R1}n_{R1} & \text{if } u(k) > n_{R1} \end{cases} \quad (13.75)$$

$$v(k) = \begin{cases} s_{L1}u(k) & \text{if } n_{L1} \leq u(k) < 0 \\ s_{L2}[u(k) - n_{L1}] + s_{L1}n_{L1} & \text{if } u(k) < n_{L1} \end{cases}$$

where $|s_{R1}| < \infty, |s_{R2}| < \infty$ are the corresponding segment slopes and $0 \leq n_{R1} < \infty$ is the constant for the positive inputs of the first nonlinear block, $|s_{L1}| < \infty, |s_{L2}| < \infty$ are the corresponding segment slopes and $-\infty < n_{L1} < 0$ is the constant for the negative inputs of the first nonlinear block (Vörös, 2002).

Introducing two new variables:

$$\begin{aligned} g_1(k) &= g_1[u(k)] = (s_{R2} - s_{R1}) h[n_{R1} - u(k)] \\ g_2(k) &= g_2[u(k)] = (s_{L2} - s_{L1}) h[u(k) - n_{L1}] \end{aligned} \quad (13.76)$$

To switch between two linear segments, the switching function $h(t)$, or more precisely $h[u(t)]$, is defined as follows (Vörös, 2003):

$$h(k) = h[u(k)] = \begin{cases} 0, & \text{if } u(k) \geq 0 \\ 1, & \text{if } u(k) < 0 \end{cases} \quad (13.77)$$

which allows eq. (13.75) to be rewritten in the following input/output for:

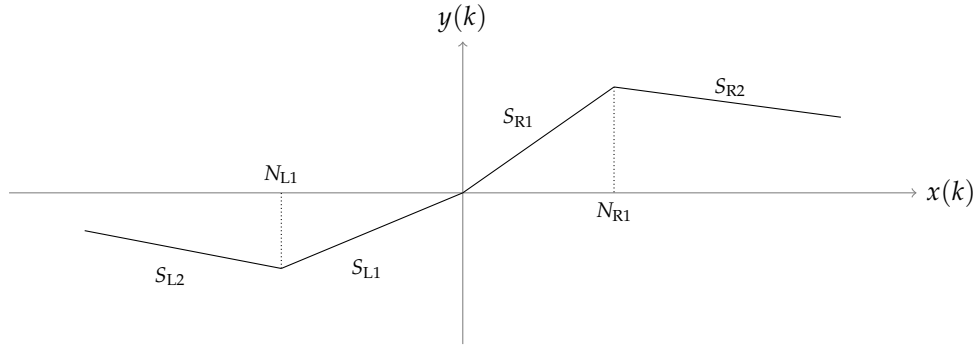


Figure 13.9: Four segment piecewise-linear nonlinearity model representation of the second nonlinear block NL_2

$$v(k) = s_{R1}h[-u(k)]u(k) + [u(k) - n_{R1}]g_1(k) + s_{L1}h[u(k)]u(k) + [u(k) - n_{L1}]g_2(k) \quad (13.78)$$

To allow for parameter estimation, a serial decomposition the two key terms $u(k)g_1(k)$ and $u(k)g_2(k)$ is used to derive a simpler form of the system description. By half-substituting into eq. (13.76), the decomposed output equation for the first nonlinear static block is found:

$$v(k) = s_{R1}h[-u(k)]u(k) + (s_{R2} - s_{R1})h[n_{R1} - u(k)]u(k) - n_{R1}g_1(k) + s_{L1}h[u(k)]u(k) + (s_{L2} - s_{L1})h[u(k) - n_{L1}]u(k) - n_{L1}g_2(k) \quad (13.79)$$

Figure 13.9 shows the second piecewise-linear block, which is comparable to NL_1 , only the segment nodes and slopes are denoted with capital letters to differentiate the formulas. Naturally, the input of the second nonlinear block uses the unknown linear dynamic system output $x(k)$. The output $y(k)$ of the second nonlinear block (NL_2) is described as:

$$y(k) = \begin{cases} S_{R1}x(k) & \text{if } 0 \leq x(k) \leq N_{R1} \\ S_{R2}[x(k) - N_{R1}] + S_{R1}N_{R1} & \text{if } x(k) > N_{R1} \end{cases} \quad (13.80)$$

$$y(k) = \begin{cases} S_{L1}x(k) & \text{if } N_{L1} \leq x(k) < 0 \\ S_{L2}[x(k) - N_{L1}] + S_{L1}N_{L1} & \text{if } x(k) < N_{L1} \end{cases}$$

where $|S_{R1}| < \infty, |S_{R2}| < \infty$ are the corresponding segment slopes and $0 \leq N_{R1} < \infty$ is the constant for the positive inputs of $N2$, $|S_{L1}| < \infty, |S_{L2}| < \infty$ are the corresponding segment slopes and $-\infty < N_{L1} < 0$ is the constant for the negative inputs of the second nonlinear static block. An overview of the discussed system layout is found in fig. 13.6.

By describing the first segment on the right-hand side and the left-hand side of the origin leads to the following form is found:

$$y(k) = S_{R1}x(k) + (S_{L1} - S_{R1})h[x(k)]x(k) + [x(k) - N_{R1}]G_1(k) + [x(k) - N_{L1}]G_2(k) \quad (13.81)$$

with the internal variables defined as:

$$\begin{aligned} G_1(k) &= G_1[x(k)] = (S_{R2} - S_{R1}) h [N_{R1} - x(k)] \\ G_2(k) &= G_2[x(k)] = (S_{L2} - S_{L1}) h [x(k) - N_{L1}]. \end{aligned} \quad (13.82)$$

Again applying the parallel decomposition rule as described in (Er-Wei Bai, 2010)(Vörös, 1999), the following output equation for the second nonlinear static block is found:

$$\begin{aligned} y(k) &= S_{R1}x(k) + (S_{L1} - S_{R1}) h[x(k)]x(k) \\ &\quad + (S_{R2} - S_{R1}) h [N_{R1} - x(k)] x(k) - N_{R1}G_1(k) \\ &\quad + (S_{L2} - S_{L1}) h [x(k) - N_{L1}] x(k) - N_{L1}G_2(k) \end{aligned} \quad (13.83)$$

By incorporating eq. (13.79) and eq. (13.83) into eq. (13.74) and choosing $S_{R1} = 1$, the half-substitution of eq. (13.73) into eq. (13.83) for the first term only gives:

$$\begin{aligned} y(k) &= b_1v(k-1) + \sum_{i=2}^m b_iv(t-i) + \sum_{j=1}^n f_jx(t-j) \\ &\quad + (S_{L1} - 1) h[x(k)]x(k) \\ &\quad + (S_{R2} - 1) h [N_{R1} - x(k)] x(k) - N_{R1}G_1(k) \\ &\quad + (S_{L2} - S_{L1}) h [x(k) - N_{L1}] x(k) - N_{L1}G_2(k) \end{aligned} \quad (13.84)$$

By choosing $b_1 = 1$ the half-substitution of eq. (13.79) into eq. (13.84) for the first term results in the following Hammerstein-Wiener system output equation:

$$\begin{aligned} y(k) &= s_{R1}h[-u(k-1)]u(k-1) \\ &\quad + (s_{R2} - s_{R1}) h [n_{R1} - u(k-1)] u(k-1) \\ &\quad - n_{R1}g_1(k-1) + s_{L1}h[u(k-1)]u(k-1) \\ &\quad + (s_{L2} - s_{L1}) h [u(k-1) - n_{L1}] u(k-1) \\ &\quad - n_{L1}g_2(k-1) + \sum_{i=2}^m b_iv(t-i) - \sum_{j=1}^n f_jx(t-j) \\ &\quad + (S_{L1} - 1) h[x(k)]x(k) - N_{R1}G_1(k) \\ &\quad + (S_{R2} - 1) h [N_{R1} - x(k)] x(k) \\ &\quad + (S_{L2} - S_{L1}) h [x(k) - N_{L1}] x(k) - N_{L1}G_2(k) \end{aligned} \quad (13.85)$$

All estimation parameters are separated in this equation, hence the proposed form of the Hammerstein-Wiener system description as it contains the least possible number of parameters to be estimated.

By defining the data vector as:

$$\begin{aligned} \varphi^T(k) &= \{h[-u(k-1)]u(k-1), \\ &\quad h [n_{R1} - u(k-1)] u(k-1), -g_1(k-1), \\ &\quad h[u(k-1)]u(k-1), h [u(k-1) - n_{L1}] u(k-1), \\ &\quad -g_2(k-1), \\ &\quad v(t-2), \dots, v(t-m), -x(k-1), \dots, \\ &\quad -x(t-n), h[x(k)]x(k), h [N_{R1} - x(k)] x(k), \\ &\quad -G_1(k), h [x(k) - N_{L1}] x(k), -G_2(k)\} \end{aligned} \quad (13.86)$$

and the parameter vector as:

$$\theta^T = [s_{R1}, s_{R2} - s_{R1}, n_{R1}, s_{L1}, s_{L2} - s_{L1}, \\ n_{L1}, b_2, \dots, b_m f_1, \dots, f_n, \\ s_{L1} - 1, s_{R2} - 1, N_{R1}, s_{L2} - s_{L1}, N_{L1}] \quad (13.87)$$

the Hammerstein-Wiener model with piecewise-linear nonlinearities can be written in the concise form:

$$y(k) = \varphi^T(k) \cdot \theta + e(k) \quad (13.88)$$

where $e(k)$ is an additive noise and the problem of model parameters estimation can be solved as a pseudo-linear estimation problem (Er-Wei Bai, 2010). In the parameter vector, the f_1, \dots, f_n and b_1, \dots, b_m refer to the parameters of the transfer function polynomials.

Generalising the piecewise-linear approach and allowing a finite amount of segments resulting in the so called multisegment piecewise-linear model is achieved by altering eqs. (13.75) and (13.76) and defining the following variables:

$$g_{1,i}(k) = (s_{R,i} - s_{R,i-1}) h [n_{R,i-1} - u(k)] \\ g_{2,j}(k) = (s_{L,j} - s_{L,j-1}) h [u(k) - n_{L,j-1}] \quad (13.89)$$

$i = 1, \dots, n_R$ and $j = 1, \dots, n_L$, where $|s_{R,i}| < \infty$ $|s_{L,j}| < \infty$ are the segment slopes, $0 \leq n_{R,i} < n_{R,i+1} < \infty$ are the constants that represent the positive inputs, and $-\infty < n_{L,j+1} < n_{L,j} \leq 0$ represent the negative inputs. The output equation for the general multisegment piecewise-linear characteristics are defined as follows:

$$x(k) = \sum_{i=1}^{n_R} \{ (s_{R,i} - s_{R,i-1}) h [n_{R,i-1} - u(k)] u(k) \\ - n_{R,i-1} g_{1,i}(k) \} \\ + \sum_{j=1}^{n_L} \{ (s_{L,j} - s_{L,j-1}) h [u(k) - n_{L,j-1}] u(k) \\ - n_{L,j-1} g_{2,j}(k) \} \quad (13.90)$$

where:

$$0 \leq n_{R,1} < n_{R,2} < \dots < n_{R,n_R} < \infty \\ -\infty < n_{L,n_L} < \dots < n_{L,2} < n_{L,1} \leq 0 \quad (13.91)$$

and $s_{R,0} = n_{R,0} = s_{L,0} = n_{L,0}$ to coincide and prevent discontinuities in zero. Now half-substituting eq. (13.90) into eq. (13.73) for the separated $x(k)$ gives the following multisegment piecewise-linear output equation:

$$y(k) = \sum_{i=1}^{n_R} \{ (s_{R,i} - s_{R,i-1}) h [n_{R,i-1} - u(k)] u(k) \\ - n_{R,i-1} g_{1,i}(k) \} \\ + \sum_{j=1}^{n_L} \{ (s_{L,j} - s_{L,j-1}) h [u(k) - n_{L,j-1}] u(k) \\ - n_{L,j-1} g_{2,j}(k) \} \\ + \sum_{i=1}^n b_i x(t-i) - \sum_{j=1}^m f_j y(t-j) \quad (13.92)$$

Resulting in a generalised and robust approach to estimate jet engine thrust by using a vibration isolator deformation in combination with a piecewise-linear nonlinear Hammerstein-Wiener model.

13.5 Conclusion

In this chapter, a variety of model approaches are discussed to estimate the generated thrust force based on the measured deflection of a Cessna model 550 vibration isolators. The first approach is physical modelling, which makes use of combining springs and dashpots. In this approach, each parameter has a physical meaning, which results in a so called white-box model. Increasing the number of physical components allows for a more accurate model, but results in more parameters to estimate.

The static nonlinear approach determines the fit of a predetermined function through the input-output data. Dynamic effects such as a hysteresis are neglected in this model. Since this is a static approach, no time data is required in this model. However, due to its simplicity, robustness and, calculation speed, this approach is a logical first approach.

For the linear dynamic modelling, there are two commonly used approaches, the equation error approach and the output error approach. The main difference is that for the equation error models, the white noise enters the difference equation as a direct error where the output error models add the noise at the output which is more realistic.

When both the static nonlinear and dynamic linear approaches do not yield satisfactory performances, nonlinear models are a natural next step. The nonlinear variants of the linear variants are modified using the Kolmogorov-Gabor structure. Another common approach is combining static nonlinear models and linear dynamic models. This is the so called block-oriented approach resulting in the Hammerstein and Wiener models. All models except the physical models allow for construction as a single input or multiple input model. Depending on the number of parameters that influence the deformation magnitude.

Chapter 14

Model Results

For the practical application of using a vibration isolator as a thrust sensor, the measured deflection is related to a thrust force using a mathematical model. This chapter discusses the performances of the models that are discussed in chapter 13. The first section discusses the measured model input and output. The second section covers the results of physical modelling by using spring and dashpot combinations. This is followed by a static nonlinear method that fits a predefined function through the data. The succeeding section discusses the linear dynamic models that approximate the behaviour with transfer function polynomials. The final section discusses the nonlinear dynamic models.

14.1 Model Parameters

A model has one or more inputs and one or more outputs, depending on the type of system. In chapter 12 it is concluded that the thrust force-deformation curve is not influenced by vibrations and temperature variations. Whereas, a varying engine weight was found to influence the thrust deformation-curve. Unfortunately, the test machine only allows for simulations in one dimension, and therefore it is not possible to include the mean load into the identification experiments. The resulting model is a so called single input - single output model (SISO) with the measured deflection as input and the force as output.

Figure 14.1 shows one hour of thrust force and deformation of an experiment. On the right hand side of the figure, the measured deformation is depicted, which is also the input for all models. The output of the model is then compared to the measured force. For this experiment, a vertical setup is exploited. The magnitudes of the simulated thrust force are random values between 400 N and 6.5 kN. The use of random values increases the variety of step sizes, directions and absolute values. Note the viscoelastic creep as the deformation slightly changes over time, while the simulated force is constant. No vibrations are added to the input force. All models are estimated using the first eight hours of this experiment and validated with the following 37 hours of measurement data. A full view of the validation data can be found in appendix A. Each force step remains constant for several minutes to include the low frequency responses, such as stress-relaxation.

The random step inputs are used to identify the system, as this represents the in-flight engine input most accurately. According to the research pilot of the TU Delft flying laboratory, the input is given in a stepwise fashion. Input shapes such as sine, triangle, or sawtooth are unheard of.

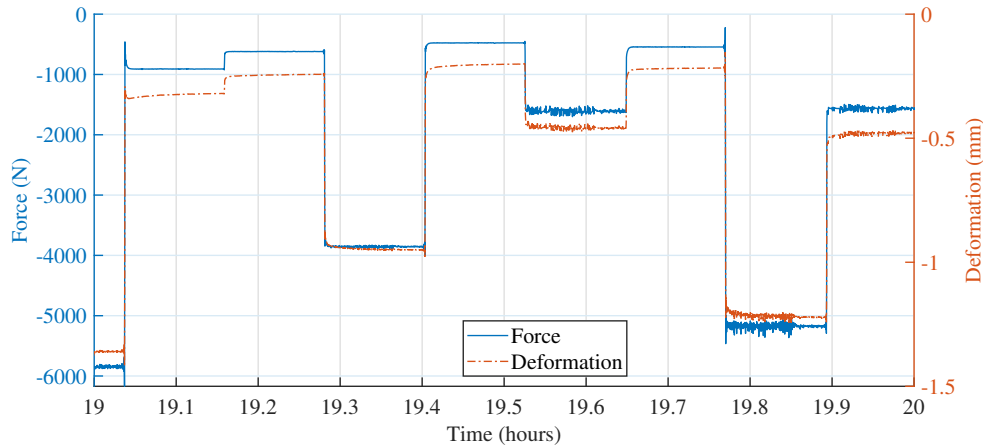


Figure 14.1: Simulated thrust force - deformation relation

14.2 Physical Models

Viscoelastic material behaviour is approachable using combinations of dashpots and springs. Using the MathWorks[®] Simscape[™] environment, a variety of spring and dashpot combinations are constructed with the aim to predict the thrust force based on the measured deflection. The benefit of using combinations of springs and dashpots is that the resulting model is a white model and is approximated with a differential equation. Furthermore, the components have physical meaning and values.

Using the basic model structures such as Maxwell or Kelvin-Voigt yielded poor performances with root mean square errors between 150 and 300 N. Note that the models are tuned by hand, as the environment does not include parameter estimation tools. Expanding the model with nonlinear springs and friction components improved the approximation marginally. Using a finite amount of Maxwell in parallel or Kelvin-Voigt models in series allows for an accurate approximation of a real system (Riande et al., 2000). However, the manual tuning of the individual components causes this approach to be a non-practical one and is therefore not further investigated.

14.3 Static Nonlinear Model

One of the simplest modelling approaches is fitting a line function through the given data set. Common methods are polynomial, power, exponential or spline fitting. These methods fit the line by adjusting the parameters of the line function, until the line fits the data with, for example, the least sum of squares. This method is static and therefore time-independent.

Figure 14.2 shows the performance of the ordinary least squares (OLS) third order polynomial fit on the estimation data. The dynamic component of the data is not modelled, as can be seen by the large error after each force step. The overall performance of the polynomial model on this data set is relatively good. The creep is not included in the model, as shown by the model error shape. The RMSE value on the validation data is 103 N. A clear advantage of the OLS approach is the calculation speed. Constructing the model and predicting the output of the validation data is performed in 0.7 seconds.

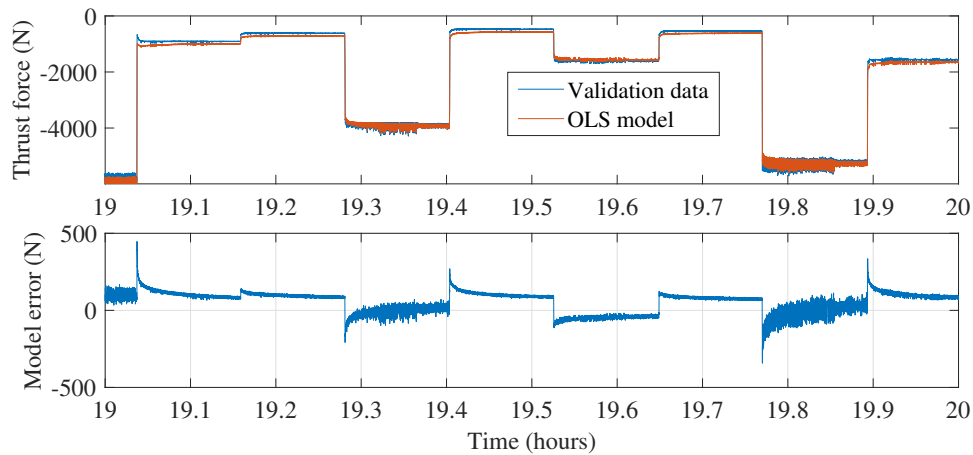


Figure 14.2: 3th order polynomial ordinary least squares static model

14.4 Linear Dynamic Models

In the previous section, a static approach is explored. This section discusses the results using a transfer function approach. This allows for the dynamic characterisation of a system. The first approach is the model error approach, which is followed by the output error models.

14.4.1 Equation Error Models

Two of the best known and widely used linear time series models are the ARX and ARMAX models, which are equation error models. The model performances on both the estimation and validation data are poor and often not below RMSE values of 300 N. Increasing the order of the estimation polynomial often results in better performances on the estimation data and worse performances on the validation data. Moreover, the model was found to become unstable more often with higher order estimation polynomials.

14.4.2 Output Error Models

A well performing linear dynamic model is the Output Error (OE) model. Output error models are characterised by a noise model that is independent of the deterministic process model and therefore do not contain the process dynamics (Nelles, 2021). Thus, the noise is assumed to influence the process output directly. The previously discussed equation error models focus on the noise model, and the input/output models aim to model the deterministic input.

Figure 14.3 shows the performance of the output error model on the validation data. Increased accuracy of the lower force magnitudes is observed, while an increased error at the larger force magnitudes is observed. For this particular model, the Levenberg-Marquardt least squares numerical search method is used for the iterative parameter estimation. A variety of numerical search methods are available, which render similar performance. The main difference is the required computation time. For this model and numerical search method, the required time to estimate the model and generate the output for the validation data is about 50 seconds. The overall performance is measured in RMSE which is 142 N for this model. This is a decrease in overall performance compared to the static nonlinear model. Note that the output error model performs well on the estimation of the dynamic parts of the model, as can be seen by the minimum peaks in the error at each step.

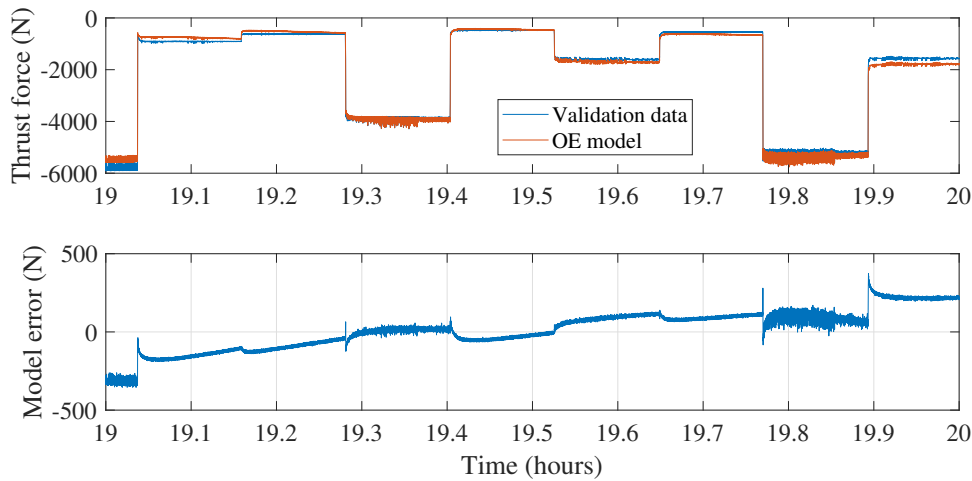


Figure 14.3: Output error model

The order of the estimation polynomial that represents the conventional transfer functions has a small influence on the direct model performance. Using a second order polynomial for both the numerator and denominator renders a RMSE value of 144 N on the validation data. Using a 6th order polynomial as numerator and 4th order polynomial as denominator results in an RMSE value of 143 N on the validation data. The transfer function of this model is described by equation 14.1. This is not a significant improvement, while the calculation time doubles to about 100 seconds. Up to the 20th order, no improvement is observed. This is an indicator that the estimation data is not linear and that nonlinear models should be considered. In combination with a static nonlinear block, the higher order polynomial transfer function does show improved model performances and are discussed in the following section.

$$\text{OE} : \hat{G}(q) = \frac{0.3440q^{-1} - 0.8570q^{-2} + 1.0000q^{-3} - 0.8210q^{-4} + 0.3480q^{-5} - 0.0150q^{-6}}{-2.4700q^{-1} + 2.7030q^{-2} - 1.9970q^{-3} + 0.7630q^{-4}} \quad (14.1)$$

14.5 Nonlinear Dynamic Models

Viscoelastic materials show a hysteresis on the stress-strain curve. This is per definition a nonlinear behaviour. In this chapter, nonlinear models are explored if better modelling behaviour is observed. Similar to the linear models show the nonlinear autoregression models poor and unstable estimation behaviour. The block-oriented nonlinear models which are composed of linear dynamic systems and nonlinear static elements show promising results.

In Matlab, the linear dynamic models in the Hammerstein-Wiener estimation function are required to be discrete-time linear models, with a deterministic process model which is independent of the noise model. The models fulfilling this requirement are input-output polynomial models of output-error structure, state-space models with no disturbance components or transfer functions models. The output error structure renders the best performances and is therefore used in combination with the nonlinear Hammerstein and Wiener models.

Combining a static nonlinear model with a linear dynamic model, in that order, results in the Hammerstein model. A third order polynomial static nonlinear model, as discussed in section 14.3, combined with a 6th order linear dynamic output error model, as discussed in section 14.4.2, results in a root mean squared error of 59 N on the validation data. A permutation of the static nonlinear model and the dynamic linear model, resulting in the Wiener model, renders a root mean square error of 61 N on the validation data. Any higher order, up to the twentieth order, yielded no improvement.

Since the model is purposed for a practical application, the adaption of a piecewise-linear approach is implemented to allow for modelling of backlash or discontinuities that for example are caused by play in the mounting system (Vörös, 2003, 2001, 1997b). The piecewise-linear approximation allows for a generic model, which facilitates a robust and future proof approach.

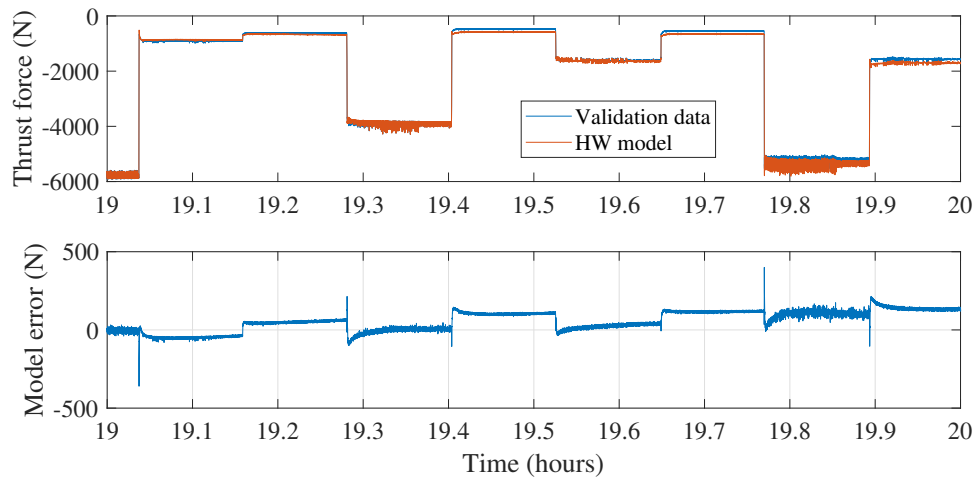


Figure 14.4: Hammerstein-Wiener model with 10 piecewise-linear input and output nodes.

A piecewise-linear approach divides the input range into a predefined number of segments, in which the nonlinearity is approximated with a linear function. Increasing the number of segments results in a higher resolution of the system nonlinearity representation. In the pursuit of a parsimonious model, piecewise-quadratic systems are not implemented, since piecewise-linear systems analyse smooth non-linear dynamics with arbitrary accuracy (Rantzer, 2000).

Implementing a ten segment piecewise-linear approximation of the system nonlinearity, combined with a sixth order polynomial output error model, yielded a root mean square error of 56 N on the validation data. If discontinuities are observed in the measurement data due to backlash or dead-zones, a higher number of segments is required. The estimation performance of the model is shown in fig. 14.4.

A root mean square error under 60 N suggests a model error under 1% of the maximum thrust force. The average of the absolute model error on 37 hours of validation data in the expected operation range ($> 2\text{ kN}$) is 1.1%. The accurate and widely implemented gas generator method achieves an accuracy of about 3% (Hughes, 1981; Del Mónico Monteiro et al., 2018). Note that the Hammerstein-Wiener model does not include sensor errors and uncertainty. The sensor that is used for the input measurements is an LVDT, which is highly accurate with low uncertainty.

are elaborated/described in section will be further explored/elaborated upon in section

14.6 Model comparison

The main differences between the implemented model approaches are found in this section. In order to gain an understanding of the model characteristics, a visualisation of each model output is depicted in fig. 14.5. In this graph, the characteristics of the three model approaches are depicted for the interest of comparison and not for practical use. A sinusoidal input shape is used to compare the different models structures, and highlight the deficiencies.

In the figure, the static nonlinear model is illustrated by the solid line. Since no dynamics are included, the compression stroke follows the exact same path as the rebound stroke. The linear dynamic model describes an angled ellipse shape where the force in the rebound stroke is noticeably lower at a given deformation. However, an ellipse has a linear eccentricity that is misaligned with the curved static nonlinear model. Combining the nonlinear static model and the linear dynamic model in the so called Hammerstein and Wiener models allows for *curved ellipses*, which describe the characteristics of the vibration isolator with high accuracy. The root mean square error of this model is 13 N and covers the reference data.

The Hammerstein-Wiener model, that is estimated on the random step in put data, displays a fast initial response to the step input, followed by a sluggish response. The initial fast response is required to model the viscous behaviour of the vibration isolator. The sluggish response represents the creep behaviour, and a so called internal friction hysteresis.

Model	RMSE (N)
Physical models	150
Static nonlinear	103
Dynamic linear	143
Hammerstein	59
Wiener	61
Hammerstein-Wiener	56
Piecewise-linear	

Table 14.1: Model performance on validation data.

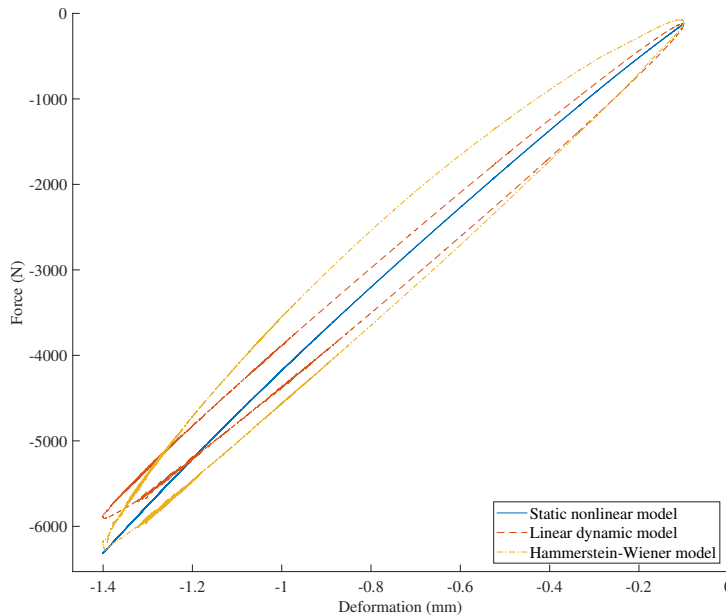


Figure 14.5: Comparison of model characteristics on sine wave input.

Since the material in the vibration isolator is silicone rubber, a viscoelastic solid, an internal friction is observed, causing energy dissipation. Consequently, no fully elastic return is observed, which is displayed as a hysteresis in the stress-strain curve. A 6th order output error model allows for a sluggish settling response, up to several hours, which approximates the internal friction hysteresis.

For future research, the implementation of a Bouc-Wen or Preisach block to the Hammerstein-Wiener block potentially increases the accuracy, as it models the internal friction phenomena (Guo, Mao & Zhou, 2015). These model extensions are not further investigated in the current research due to insufficient available time.

Knowing the model characteristics allows us to recognise these characteristics in the model errors. The model errors are depicted in one graph which is shown in fig. 14.6. The first few minutes of the error data shows a large error for the linear dynamic model. The force load at this moment is about 6 kN, which corresponds to a large error, as shown in fig. 14.5. Further observations show the large peaks in the static model at large thrust force steps, which is expected from a static model. The linear dynamic improves on the dynamic components, while the overall performance decreases when compared to the static nonlinear model. Combining the static nonlinear and dynamic linear model, resulting in the Hammerstein-Wiener model, provides the lowest model error. Reviewing model performance on the remaining hours of validation data is possible in appendix A.

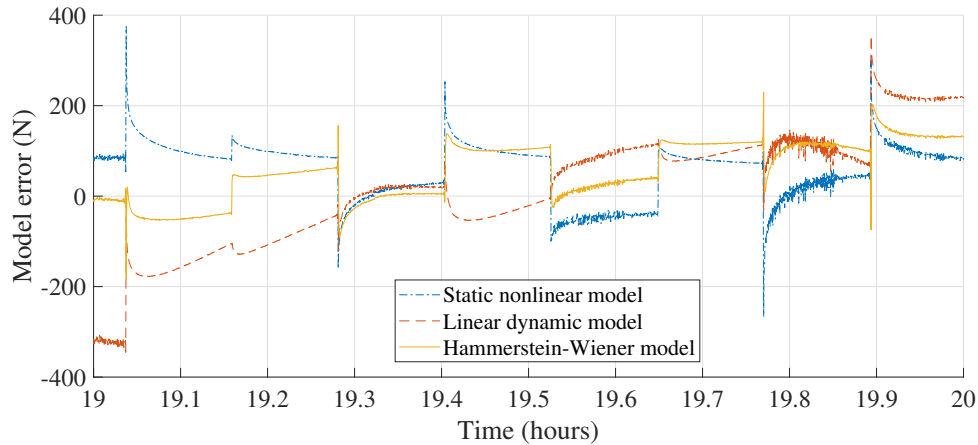


Figure 14.6: Model error comparison

14.7 Observations

To investigate the performance on dynamic measurement data, the model that estimated based on the random thrust force step experiment is used to predict the output of a 0.003 Hz sine wave (fig. 14.7). A clear sinusoidal shaped error is found, indicating insufficient modelling performances.

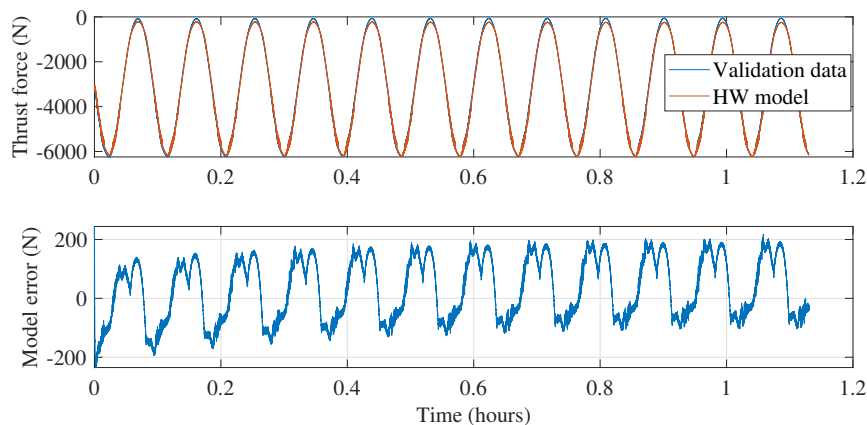


Figure 14.7: Hammerstein-Wiener model with sinusoidal thrust input

In the case that a model is estimated based on a single frequency sinus wave, the model performs exceptionally well on the validation data of the same frequency. By varying the frequency, the model error increases. This indicates that the dynamics of the vibration isolator are dependent on the rate of change of the applied force. This is in line with the expectations, as this is viscous behaviour. A general identification experiment approach is to perform frequency sweeps. This allows us to map the variation in dynamics with high accuracy. In the MTS test machine, the advanced dynamic characterisation software package is not available, and therefore, no continuous frequency sweeps can be performed. Besides this, only one dimension is computer controlled, and for identification experiments of all influential parameters, excitement of both the weight, and thrust force is required. To excite both parameters dynamically at the same time, a biaxial test machine is required.

Estimating a Hammerstein-Wiener model using a 0.003 Hz sinus wave data, shows a root mean square error of only 13 N on the validation data of the same frequency (fig. 14.8). A model that is estimated using the step input shows a root mean square error of 108 N . This indicates a deficiency in the dynamics that are captured in the step input experiments, and is a point of improvement for subsequent research. Once more, for these frequency sweep experiments, additional MTS controller software is required.

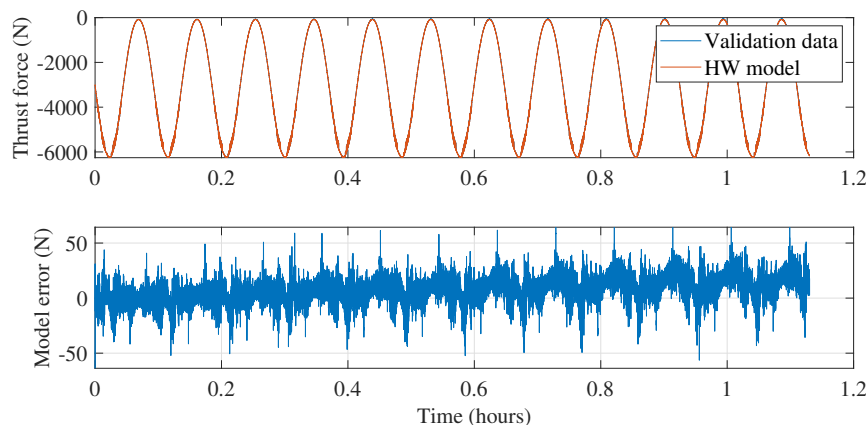


Figure 14.8: Hammerstein-Wiener model estimated with 0.003 Hz data

For a jet engine, however, the dynamic response is of less importance, since the throttle input is generally a stepwise input. Moreover, the maximum rate of change for a jet engine is limited by the engine spin up time, and dependent on the conditions, may take up to 8-13 seconds from idle to 95% rated take-off thrust for this particular engine (FAA, 2016; D. Boyd, 1990).

Considering the fact that the maximum rate of change is fixed per engine and is expected to be of a lower rate than the pilot adjustment rate, a model that is based on the step input data suffices for the intended application. In the case that one requires continuous throttle adjustments in flight, additional identification experiments are required. Note that it is possible to perform these experiments without removing the vibration isolators or engines from the aircraft (Chen, 2012).

One might wonder if the additional model complexity of the Hammerstein-Wiener model is justified given the simplicity of the static nonlinear model and the gained performance. Both models lead to thrust estimation, it is the application that determines which model would be the best suited. For the static nonlinear model, the largest error is observed in the first half a minute after a thrust step, and reduces gradually over the following minutes. For the Hammerstein-Wiener system, generally a one-second peak is observed after a thrust step input, followed by relatively stable and low error prediction of the thrust.

If one intends to adjust the throttle settings once every hour, a static model is expected to show adequate prediction performance, and the effort of implementing the Hammerstein-Wiener system should be avoided. If, on the other hand, parabolic test flights are part of the flight program, the Hammerstein-Wiener model highly recommended as the throttle is adjusted from full power, to idle, and back to full power in quick succession. Furthermore, the time to execute test flight manoeuvres is confined, and waiting up to ten minutes after each throttle adjustment to lower the thrust measurement error is not cost effective, or might not be feasible.

Apart from this, is a Hammerstein-Wiener model capable of capturing the engine transient response, which is an important parameter to monitor the engine condition and determine deteriorated performances (Grönstedt & Zhao, 2004). A research field that is dedicated to determine and model the jet engine transient response characteristics would benefit from a direct thrust reading (Athavale, Steinetz & Hendricks, 2001; Chang, 2009; Li, MacCallum & Pilidis, 2001).

14.8 Conclusion

This section discusses the observed differences between the investigated models. The physical models are able to estimate real physical models at high accuracy, under the condition that a finite amount of springs and dashpots are used. Using the Maxwell and Kelvin-Voigt model resulted in root mean square errors between 150 and 300 N. Besides the poor modelling results, the manual tuning of all the individual components is time consuming and not practical.

The static nonlinear approach estimates the parameters of a certain function such that it fits the data with the least square error. This approach is static and requires no time data, and each time point is independent of any other point in time. As the model is linear, it omits all dynamic effects. However, this approach is appealing for its simplicity, robustness, and fast calculation speeds.

The linear dynamic models are transfer function models and are split into equation error and output error models. Both are based on time series data. The equation error models showed poor and unstable model performances, with root mean square errors of about 300 N. The output error models showed stable and consistent results, with root mean square errors of about 142 N. Increasing the order of the transfer function resulted in no improvement, which indicates the presence of system nonlinearity.

Combining the static nonlinear model and the dynamic linear model respectively yields a nonlinear dynamic model or so-called Hammerstein model. This model renders a root mean square error of 59 N on the validation data. A permutation of the static nonlinear model and the dynamic linear model results in the Wiener model and renders a root mean square error of 61 N on the validation data.

In practice, discontinuities in the nonlinearity approximation such as backlash or dead-zones might appear. For this reason, a piecewise-linear nonlinearity approximation is implemented instead of a polynomial approximation. Combining a Hammerstein and Wiener model into a Hammerstein-Wiener model, and the piecewise-linear, yielded higher estimation performances when combined with the piecewise-linear approach. With this model, a 56 N root mean square error is observed on the step input validation data.

The prediction of the thrust model on experiments with sinusoidal thrust input showed deteriorated performance. This indicates that the dynamics behaviour of the vibration isolator is not captured precisely by the model. For the intended application, which is normal test flights, the thrust input is performed in steps, and accurate predictions are expected. If one intends to perform test flights with sinusoidal thrust inputs, this model lacks accuracy and identification experiments with frequency sweeps are required. These can be performed on either a biaxial test setup, an adjusted engine rig, or the actual aircraft with a static run. Performing these experiments with an actual engine provides, naturally, the best representation of the engine dynamics.

The consideration of implementing either the static nonlinear model or the Hammerstein-Wiener model depends on the planned type of test flights. For test flights during which the throttle is adjusted only once an hour, a static nonlinear model is expected to suffice. For test flights with more frequent throttle adjustments, a nonlinear dynamic approach is recommended.

Chapter 15

Conclusions

A novel method of low cost in-flight thrust measurement is presented. For aircraft with fuselage mounted engines, the engine thrust is transferred from the engine to the fuselage by solely two engine vibration isolators, which consist of silicone rubber and are designed to deform under load. In the pursuit to answer the question *"How can the jet engine vibration isolator deformation be used to estimate the thrust force?"*, a vibration isolator is acquired in order to perform the experiments. These experiments, which outline the dynamic characteristics, are performed on an MTS 831 test machine with an additional custom made system that simulates forces in a second dimension. The experiments are performed with the aim to determine the influence of independent variables on the dependent variable. The independent variables being temperature, engine vibration frequency, engine vibration amplitude and engine weight. The dependent variable being the deformation caused by a certain simulated thrust force. Note that the main engine vibrations act in the radial direction and the thrust in the axial direction with respect to the engine.

The characterisation experiments revealed an independence of the operation temperature and engine vibration, with the thrust force and deformation curve. The engine weight exhibited a measurable effect on the deformation at a constant thrust force. Given that the engine is exposed to double the gravitational acceleration, a maximum thrust measurement error of 1.6% is observed. The engine weight parameter is not utilised as an additional model parameter, because these experiments require a biaxial test machine.

For a practical application of using a vibration isolator as a thrust sensor, the measured deflection is related to a thrust force using a mathematical model. Several model structures are explored, starting with the physical models. These models are constructed using merely spring and dashpot combinations. Increasing the accuracy is achieved by increasing the physical components in the model. Increasing the number of components consequently increases the number of estimation parameters. This results in an impractical modelling approach. The second approach is an ordinary least squares approach that estimates the parameters of the polynomial fitting the data. This allows for estimating nonlinear static systems, however, falls short with regard to the system dynamics. An ordinary least square estimated third order polynomial showed a root mean square error of 103 N on the validation data that ranges up to 6.5 kN.

Using linear dynamic output error models resulted in a decrease in performance, as the root mean square error on the validation data is 142 N. It was found that increasing the order of the transfer function yielded no better results, indicating a system nonlinearity. Combining the static nonlinear model with the best performing linear dynamic model in that order results in the Hammerstein model, and renders a root mean square error of 59 N on the validation data. A permutation of the static nonlinear model and the dynamic linear model, resulting in the Wiener model, renders a root mean square error of 61 N on the validation data.

A logical evolution is combining these Hammerstein and Wiener models, resulting in the Hammerstein-Wiener model. Since the model is purposed for a practical application, a piecewise-linear approach is implemented to allow for modelling of backlash or discontinuities that, for example, are caused by play in the mounting system. Introducing the piecewise-linear approximation for the nonlinearity, reduced the root mean square error to 56 N.

By using a Hammerstein, Wiener or Hammerstein-Wiener model, the model root mean square error is found to be less than 1% of the maximum thrust load. In addition, the average of the absolute model error on the validation data in the expected operation range (> 2 kN) is 1.1 %.

The models are estimated using step wise simulated thrust inputs, as these are the type of inputs for test flights. If the output of a sinusoidal input is predicted with such a model, a deficiency is noticed in the approximation results. A sinusoidal shaped error is noticed, indicating an insufficient mapping of the system dynamics. To improve the dynamic response of the model, additional identification experiments with frequency sweeps are required on an appropriate test machine. For a practical use, no sinusoidal shaped thrust inputs are expected.

The additional complexity of a nonlinear dynamic model over a simplistic static model is justifiable by the application. The estimation error of a static nonlinear model is largest in the first minute after a thrust step input, and gradually reduces over the following minutes. The constructed Hammerstein-Wiener model shows an error of up to one second and settles at a relatively low, and constant error. If the frequency of the throttle input is once every hour, the effort of implementing a dynamic nonlinear model is not justified. For test flights with successive throttle inputs over a span of minutes, a dynamic nonlinear model is essential. Furthermore, the ten minutes downtime after each thrust input might not be cost efficient as the test flight time is confined.

The overall first impression of the principle is positive, and an implementation is realisable in the near future. To conclude, the presented cost effective method of direct thrust prediction is found highly feasible, and paves a way to support the system identification, aerodynamic research and accelerate the development of low emission, or hybrid fuel engines advancing the aviation industry and preparing for the future.

Chapter 16

Recommendations

This chapter discusses the potential for successive research and the approaches or items that are not included in the scope of this research. All steps in this research are performed to ensure the highest applicability of the proposed concept on the research aircraft.

The research is divided into three phases. The first phase is to determine if the vibration isolators are suited to be used as a thrust sensor, which is the main question of this thesis. The second phase is testing the concept on a jet engine which is mounted on a test stand. The laboratory aircraft department maintains close contact with the ROC of Tilburg, which is in possession of a Pratt&Whitney JT15D-4 engine, and the ROC of Tilburg is willing to collaborate on this second part of the research. The author of this thesis maintains close contacts with Jetsupport in Amsterdam and persuaded the company to provide the required consumables such as kerosene, engine oil, and hydraulic fluid.

The engine test stand materials are the only required costs. For this test stand, a swing, slide or rolling construction enables the possibility to relate the measured deflection to actual engine thrust with the corresponding vibrations and temperatures. This eliminates all the assumptions that are made for the simulation of the vibrations. It is required for the engine test stand to allow for the simulation of weight in multiple dimensions, since this is the parameter that influenced the thrust reading.

The third phase of the research comprises the implementation of the system on the PH-LAB flying laboratory. There are two options to perform a calibration of the engine vibration isolator, without it being necessary to remove any components. For the first method, a static engine run is performed, during which the aircraft is attached to a force gauge. This is a non standard procedure, as the aircraft brakes are generally applied during engine test runs. For the second method, a calibrated force is exerted on the engine to simulate thrust. This method is simplistic and might not render adequate results.

The implementation of the Bouc-Wen or the Preisach hysteresis model into the Hammerstein-Wiener could be considered in further studies. This would presumptively improve the estimation of the internal friction hysteresis, since the current model only approximates the hysteresis with a low frequency step response.

Additional identification experiments are required to capture the full system dynamic response. These experiments are mostly required if non-step throttle inputs are part of the test flight. For these identification experiments, frequency sweeps are required, which on the current test setup is not possible due to a missing controller software package. Moreover, for the simultaneous reproduction of both the thrust force and the engine weight, a biaxial test setup is required. Alternatively, the experiment setup of the second research phase is designed to perform these exact experiments. The resulting experiment data facilitates the construction of a multiple-input, single-output model. Further research is required to estimate the engine weight during flight manoeuvres, based on the measured accelerations and construction geometry.

Research into the ageing characteristics of the vibration isolator is beneficial for the practical application of the concept. Knowledge about the ageing characteristics allows the user to determine the required calibration interval, and possible required model corrections.

Combining the sensory data of two measurement methods is known as sensor fusion, and could be interesting for research into modelling the engine transient response.

Part III

Scientific Paper

In-Flight Jet Engine Thrust Prediction by Measuring the Engine Vibration Isolators Deformation

Robert Poppe

Abstract—Direct measurement of thrust in-flight is a missing element in aircraft system identification and, in addition, highly valuable for research in flight performance, aerodynamics, and the development of new aircraft. In this research, the applicability of using the engine vibration isolators as thrust sensors for fuselage mounted jet engines is examined. This is achieved by first performing characterisation experiments to determine the influences of environmental and operational conditions. And secondly by identification experiments which are used to construct a mathematical thrust model based on the measured deformation. The vibrations and temperature are found to not influence the stress-strain relation in the thrust direction. The varying engine weight caused a minor but measurable influence on the same relation. By constructing a Hammerstein-Wiener model, the average thrust estimation error is reduced to 1.1% within the operation range. This results in an accurate thrust estimation method at a fraction of what current methods cost.

Index Terms—In-flight direct thrust measurement, engine vibration isolator, Hammerstein-Wiener model, piecewise-linear nonlinearity

I. INTRODUCTION

DIRECT thrust measurements during flight were historically considered infeasible [1]. There are two known methods for direct thrust measurement. The first method is the *trunnion thrust* method, in which all body forces that act through the engine mounting trunnions are summed [2]–[4]. The second method is the *strain-gauge* method, which exploits the mounting construction [5]–[8] or the mounting pin [9], [10] deformation as a thrust indication. Both methods lead to complex and impractical systems [11] and result in thrust estimation accuracies ranging from 4% to 15%.

For this reason, the engine thrust is usually estimated by either the *brochure description* or *gas generator* method. The *brochure description* method relies upon the measured engine fuel flow and fan rotation speed, which are related to the performance sheets that are generally provided by the manufacturer [12], [13]. The *gas generator* method includes additional pressure, temperature, and mass flow sensors that are placed in the jet engine and calibrated in an altitude test facility, this increases the accuracy along with the total costs [1], [14]–[17]. Furthermore, the transient response of the turbine engine is not accurately modelled by the general *brochure description* or *gas generator* method [18]–[20].

The in-flight thrust is interesting for several areas of aerospace research and development. The first field of research is aircraft system identification. To perform system identification of a dynamic system, all input and output parameters must be known, and for aircraft, the thrust input parameter is not precisely defined [21], [22].

The second field of research is aerodynamics, in which the lift-to-drag ratio is one of the main design factors. It should be noted that thrust equals drag in steady forward flight and if the thrust is measured, the lift-to-drag ratio is directly determined. Additionally, the effect of in-flight configuration changes and setup adjustments on the total drag can be measured.

The third and final field of research is engine development, where access to an in-flight thrust reading reduces the amount of engine removal and installations in the development phase. This in turn facilitates the monitoring of low-frequency engine degradation or high-frequency engine stall and surge characteristics.

A. Proposed Method

For general aviation aircraft, it is common to have the engines mounted on the rear fuselage since the wings are mounted below the fuselage, leaving no space to install an engine below the wing. For aircraft with engines mounted to the rear fuselage, typically the mounting constructions are very similar and consist of one rear mount and two front mounts, which in fig. 1 are indicated with the letter A. The engine thrust is transferred to the fuselage via the two front vibration isolators. These vibration isolators consist of silicone rubber and hence can easily deform, which reduces the vibrations and acts as noise abatement. The thrust force that is generated by the engine also deforms these vibration isolators. Because no structural alterations are required, the expenses on certification are saved.

The trunnion thrust and strain-gauge methods measure the deformation of metal components in the engine mounts or pins. The benefit of using this approach is the linearity in stress-strain behaviour of the metal engine components. However, the material is strong and shows relatively low strain behaviour, which increases the sensitivity to thermal expansion and noise. Additionally, a practical hindrance arises regarding the placement of the signal conditioning apparatus of this analogue signal. Utilising the vibration isolators leads to much larger deformations at the cost of introducing nonlinear stress-strain behaviour. Moreover, the deformation of the vibration is independent of the airspeed and operation altitude, and as a consequence, no costly altitude test facilities are required.

This paper takes the first step to enable low cost in-flight thrust prediction by measuring the deformation of the vibration isolators. More precisely, the manuscript presents characterisation, identification and modelling of the vibration isolator in the form of various experiments. This paper is the first to exploit the engine vibration isolators to predict the

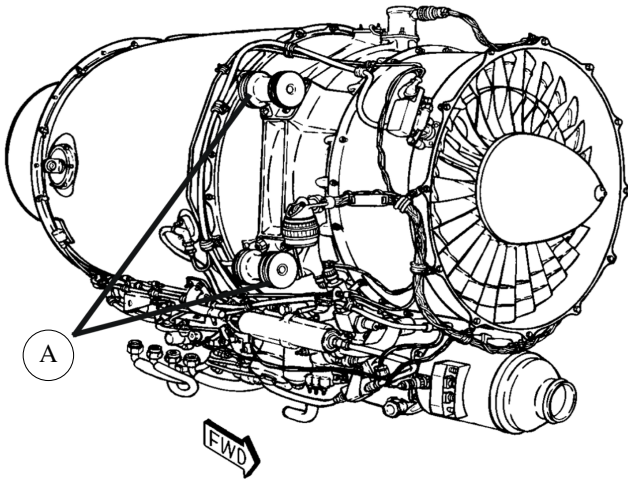


Fig. 1: Forward engine vibration isolators of the Cessna model 550. [23] The figure shows the mounting construction of a typical fuselage-mounted engine. This particular engine is shown as these vibration isolators are used for the experiments. The vibration isolators are indicated by the letter A.

in-flight thrust, to the best knowledge of the author. Starting with the characterisation experiments, which are performed to determine the influence of environmental and operational conditions on the stress-strain curve in the thrust direction. This is necessary to determine if the vibration isolator has the right characteristics to be used as a thrust sensor. The second type of experiments is the identification experiments, which are performed to model the vibration isolator in the thrust direction under constant environmental and operational conditions. This data is used to generate the mathematical models, allowing the user to translate vibration isolator deformation into thrust.

II. MODELS

The purpose of a mathematical model is to describe the system dynamics that is captured in the identification experiments. If the system dynamics are well described by the mathematical model, the system output is estimated accurately with only the measured system input. This section discusses a variety of approaches to estimate the engine thrust based on the measured vibration isolator deformation.

A mathematical model is estimated using a dataset obtained during an eight-hour run on the experimental facility, resulting in a total of $N = 2.9 \cdot 10^6$ samples. The validation is performed on a 37-hour dataset with $N_{val} = 13.4 \cdot 10^6$ samples, no overlap is used.

A. Physical models

The first model approach is the physical modelling, resulting in so called white box models, and are based on Newton's and Hook's law.

Ideal viscous liquids obey Newton's law and ideal linear elastic solids obey Hooke's law. Viscous liquids are modelled

with a dashpot and elastic solids with a spring. Hence, a viscoelastic material is modelled with a combination of dashpots and springs. Placing a dashpot and spring in series is called the Maxwell model, and in parallel it is called the Voigt model, which is sometimes referred to as the Kelvin-Voigt model [24]. The Maxwell model is used to model viscoelastic liquids and the Voigt model is used to model viscoelastic solids. The Voigt model predicts creep more realistically than the Maxwell model as the strain approaches a constant in infinite time. The Maxwell model predicts stress relaxation more realistically compared to the Voigt model [25]. By using dashpot and spring combinations, all parameters have an easy to understand and physical meaning, causing this to be a white-box model.

B. Static nonlinear model

The second approach uses linear regression to fit a given curve structure to a set of input-output data. In this case, the system is assumed to be static, implying that no material memory effects are present. The input-output mapping is allowed to be nonlinear, which enables modelling of the nonlinearity in the force-to-displacement behaviour observed in the vibration isolator.

C. Linear dynamic models

The third approach assumes the system can be modelled as an LTI system. Using a transfer function approach facilitates the modelling of the dynamics of linear systems. Using the equation error approach with ARX and ARMAX model structures, the estimation performances are found to be poor and often unstable. Better performance is achieved with the output error (OE) method. The output error model, as given in eq. (1), differs from the equation error model, as given in eq. (2), as the output error approach assumed that the noise $e(k)$ is added to the output and has no interference with the estimation process $\frac{1}{A(q)}$. This allows for a more realistic model, thus comprehend real systems better than equation error models [26]. Because the noise is not explicitly included in the system dynamics, the model is nonlinear in the parameters, resulting in a pseudo-linear model which is harder to estimate.

$$y(k) = \frac{B(q)}{F(q)}u(k) + e(k) \quad (1)$$

$$y(k) = \frac{B(q)}{A(q)}u(k) + \frac{1}{A(q)}e(k) \quad (2)$$

D. Nonlinear dynamic models

The fourth and final approach is to assume a nonlinear dynamic model structure in the form of the Hammerstein or Wiener model, depending on the order of the linear dynamic and nonlinear static blocks

In the Hammerstein model, the nonlinear static element come first, after which its output is driven through a linear dynamic system [27]. A permutation of the static nonlinear and linear dynamic model results in the Wiener system [28]. Hammerstein and Wiener models allow for high accuracy approximations of nonlinear dynamic models [29]

A series combination of a Hammerstein and a Wiener model immediately produces a new model structure called the Hammerstein–Wiener system, as is shown in fig. 2. Yielding a cascade connection of a static nonlinear input block (NL₁), a linear dynamic system (L) and a static nonlinear output block (NL₂).

The first block (NL₁) is described as:

$$v(k) = C[u(k)] \quad (3)$$

Here, $u(k)$ is the input, $v(k)$ is the output, and $C[\cdot]$ is the nonlinear static mapping of the system input. The linear block difference equation is given as:

$$x(k) = \frac{B(q)}{F(q)}v(k) + e(k) \quad (4)$$

Here, $v(k)$ is the input, $x(k)$ the output and $F(q)$ and $B(q)$ are output error model transfer function polynomials. q denotes the forward shift operator, i.e., $q^{-1}x(k) = x(k-1)$, and thus is the time domain counterpart of the $z = e^{j\omega}$ operator in the frequency domain [26]. To be in formal agreement with Z-transform and Fourier-transform expressions, q is chosen as argument of B rather than q^{-1} , even though it might seem counterintuitive [30]. $e(k)$ refers to white noise input. The transfer function polynomials are decomposed as follows:

$$\begin{aligned} F(q) &= f_1q^{-1} + \dots + f_mq^{-m} \\ B(q) &= b_1q^{-1} + \dots + b_nq^{-n} \end{aligned} \quad (5)$$

The second nonlinear static block (NL₂) is described as:

$$y(k) = D[x(k)] \quad (6)$$

The system input $u(k)$ and output $y(k)$ are measurable and the internal variables $v(k)$ and $x(k)$ are not measurable. A direct substitution of eq. (3) into eq. (4) and then into eq. (6) would result in a highly nonlinear model in both the variables and parameters. This is not desirable if parameter estimation is used. To reduce the nonlinearity of the system and permit the use of parameter estimation, a serial decomposition is used to derive a simpler form of the system description. This is the key term separation principle, applied multiple times within a compound mapping [31]–[33]. Note that in the case of analytic mappings, such decomposition forms always exist [34].

The decomposition of the second nonlinear block (NL₂) is formulated as:

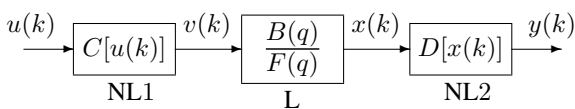


Fig. 2: Hammerstein-Wiener model.

$$y(k) = d_1x(k) + D[x(k)] \quad (7)$$

with a separated internal variable $x(k)$, the linear dynamic block equation is written as:

$$x(k) = b_1v(k-1) + [B(q) - b_1]v(k-1) - F(q)x(k) \quad (8)$$

with the internal variable $v(k-1)$ separated. Completing the serial decomposition results in the following output equation of the Hammerstein-Wiener system:

$$y(k) = d_1\{b_1C[u(k-1)] + [B(q) - b_1]v(k-1) - F(q)x(k)\} + D[x(k)] \quad (9)$$

To simplify the system and make the solution unique, parameters d_1 and b_1 are set to one.

E. Piecewise-linear

To model the nonlinearity of the static nonlinear blocks NL1 and NL2, several approaches are possible. For the engine vibration isolator, which is utilised for the experiments, a polynomial approach performed well. Since the model is purposed for a practical application, the adaption of a piecewise-linear approach is implemented to allow for modelling of backlash or discontinuities that for example are caused by play in the mounting system [32], [35], [36]. The piecewise-linear approximation allows for a generic model, which facilitates a robust and future proof approach.

A piecewise-linear approach divides the input range into a predefined number of segments, in which the nonlinearity is approximated with a linear function. Increasing the number of segments results in a higher resolution of the system nonlinearity representation.

In the pursuit of a parsimonious model, piecewise-quadratic systems are not implemented, since piecewise-linear systems analyse smooth nonlinear dynamics with arbitrary accuracy [37]. For comparison, the nonlinearity of the vibration isolator is accurately approximated with ten linear segments, which gives the impression of a smooth nonlinear relation. In an attempt to limit the equation size, a four segment piecewise-linear is adapted for the mathematical expressions. The output $v(k)$ of the four segment piecewise-linear static block NL1, as shown in fig. 3, is described as:

$$v(k) = \begin{cases} s_{R1}u(k) & \text{if } 0 \leq u(k) \leq n_{R1} \\ s_{R2}[u(k) - n_{R1}] + s_{R1}n_{R1} & \text{if } u(k) > n_{R1} \end{cases}$$

$$v(k) = \begin{cases} s_{L1}u(k) & \text{if } n_{L1} \leq u(k) < 0 \\ s_{L2}[u(k) - n_{L1}] + s_{L1}n_{L1} & \text{if } u(k) < n_{L1} \end{cases} \quad (10)$$

where $|s_{R1}| < \infty, |s_{R2}| < \infty$ are the corresponding segment slopes and $0 \leq n_{R1} < \infty$ is the constant for the positive input nodes of the first nonlinear block, $|s_{L1}| < \infty, |s_{L2}| < \infty$ are the corresponding segment slopes and $-\infty < n_{L1} < 0$ is the constant for the negative input nodes of the first nonlinear block [38].

To switch between two linear segments, the switching function $h(t)$, or more precisely $h[u(t)]$, is defined as follows [35]:

$$h(k) = h[u(k)] = \begin{cases} 0, & \text{if } u(k) \geq 0 \\ 1, & \text{if } u(k) < 0 \end{cases} \quad (11)$$

and by introducing two new variables:

$$\begin{aligned} g_1(k) &= g_1[u(k)] = (s_{R2} - s_{R1}) h[n_{R1} - u(k)] \\ g_2(k) &= g_2[u(k)] = (s_{L2} - s_{L1}) h[u(k) - n_{L1}] \end{aligned} \quad (12)$$

eq. (10) can be rewritten in the following input output form:

$$\begin{aligned} v(k) &= s_{R1} h[-u(k)]u(k) + [u(k) - n_{R1}] g_1(k) \\ &+ s_{L1} h[u(k)]u(k) + [u(k) - n_{L1}] g_2(k) \end{aligned} \quad (13)$$

To permit the use of parameter estimation, a serial decomposition of the two key terms $u(k)g_1(k)$ and $u(k)g_2(k)$ is used to derive a simpler form of the system description. By half-substituting into eq. (12), the decomposed output equation for the first nonlinear static block is found:

$$\begin{aligned} v(k) &= s_{R1} h[-u(k)]u(k) + (s_{R2} - s_{R1}) h[n_{R1} - u(k)] u(k) \\ &- n_{R1} g_1(k) \\ &+ s_{L1} h[u(k)]u(k) + (s_{L2} - s_{L1}) h[u(k) - n_{L1}] u(k) \\ &- n_{L1} g_2(k) \end{aligned} \quad (14)$$

The second piecewise-linear block is the same as NL1, only the segment nodes and slopes are denoted with capital letters, as depicted in fig. 4. Naturally, the input of the second nonlinear block uses the unknown linear dynamic system output $x(k)$. The output $y(k)$ of the second nonlinear block (NL2) is described as:

$$\begin{aligned} y(k) &= \begin{cases} S_{R1}x(k) & \text{if } 0 \leq x(k) \leq N_{R1} \\ S_{R2}[x(k) - N_{R1}] + S_{R1}N_{R1} & \text{if } x(k) > N_{R1} \end{cases} \\ y(k) &= \begin{cases} S_{L1}x(k) & \text{if } N_{L1} \leq x(k) < 0 \\ S_{L2}[x(k) - N_{L1}] + S_{L1}N_{L1} & \text{if } x(k) < N_{L1} \end{cases} \end{aligned} \quad (15)$$

where $|S_{R1}| < \infty, |S_{R2}| < \infty$ are the corresponding segment slopes and $0 \leq N_{R1} < \infty$ is the constant for the positive input nodes of NL2, $|S_{L1}| < \infty, |S_{L2}| < \infty$ are the

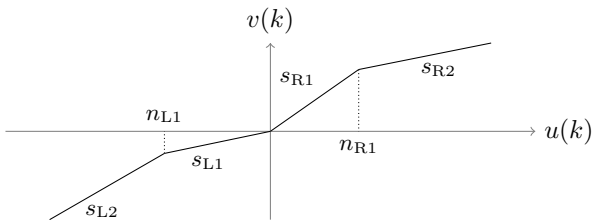


Fig. 3: Four segment piecewise-linear nonlinearity model representation of the first nonlinear block NL1

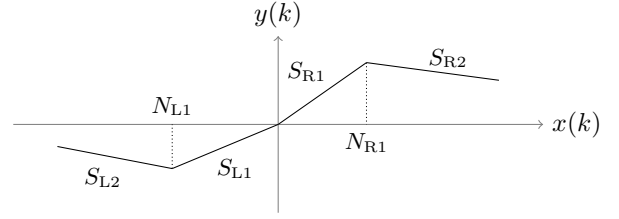


Fig. 4: Four segment piecewise-linear nonlinearity model representation of the second nonlinear block NL2

corresponding segment slopes and $-\infty < N_{L1} < 0$ is the constant for the negative input nodes of the second nonlinear static block.

Describing the first segment on the right-hand side and the left-hand side of the origin leads to the following form:

$$\begin{aligned} y(k) &= S_{R1}x(k) + (S_{L1} - S_{R1}) h[x(k)]x(k) \\ &+ [x(k) - N_{R1}] G_1(k) + [x(k) - N_{L1}] G_2(k) \end{aligned} \quad (16)$$

with the internal variables defined as:

$$\begin{aligned} G_1(k) &= G_1[x(k)] = (S_{R2} - S_{R1}) h[N_{R1} - x(k)] \\ G_2(k) &= G_2[x(k)] = (S_{L2} - S_{L1}) h[x(k) - N_{L1}]. \end{aligned} \quad (17)$$

Again applying the parallel decomposition rule as described in [34] [39], the following output equation for the second nonlinear static block is found:

$$\begin{aligned} y(k) &= S_{R1}x(k) + (S_{L1} - S_{R1}) h[x(k)]x(k) \\ &+ (S_{R2} - S_{R1}) h[N_{R1} - x(k)] x(k) - N_{R1} G_1(k) \\ &+ (S_{L2} - S_{L1}) h[x(k) - N_{L1}] x(k) - N_{L1} G_2(k) \end{aligned} \quad (18)$$

By incorporating eq. (14) and eq. (18) into eq. (9) and choosing $S_{R1} = 1$, the half-substitution of eq. (8) into eq. (18) for the first term only gives:

$$\begin{aligned} y(k) &= b_1 v(k-1) + \sum_{i=2}^m b_i v(t-i) + \sum_{j=1}^n f_j x(t-j) \\ &+ (S_{L1} - 1) h[x(k)]x(k) \\ &+ (S_{R2} - 1) h[N_{R1} - x(k)] x(k) - N_{R1} G_1(k) \\ &+ (S_{L2} - S_{L1}) h[x(k) - N_{L1}] x(k) - N_{L1} G_2(k) \end{aligned} \quad (19)$$

By choosing $b_1 = 1$ the half-substitution of eq. (14) into eq. (19) for the first term results in the following Hammerstein-Wiener system output equation:

$$\begin{aligned}
y(k) = & s_{R1}h[-u(k-1)]u(k-1) \\
& + (s_{R2} - s_{R1})h[n_{R1} - u(k-1)]u(k-1) \\
& - n_{R1}g_1(k-1) + s_{L1}h[u(k-1)]u(k-1) \\
& + (s_{L2} - s_{L1})h[u(k-1) - n_{L1}]u(k-1) \\
& - n_{L1}g_2(k-1) + \sum_{i=2}^m b_i v(t-i) - \sum_{j=1}^n f_j x(t-j) \\
& + (S_{L1} - 1)h[x(k)]x(k) - N_{R1}G_1(k) \\
& + (S_{R2} - 1)h[N_{R1} - x(k)]x(k) \\
& + (S_{L2} - S_{L1})h[x(k) - N_{L1}]x(k) - N_{L1}G_2(k)
\end{aligned} \tag{20}$$

All estimation parameters are separated in this equation, hence the proposed form of the Hammerstein-Wiener system description as it contains the least possible number of parameters to be estimated.

By defining the data vector as:

$$\begin{aligned}
\varphi^T(k) = & \{h[-u(k-1)]u(k-1), \\
& h[n_{R1} - u(k-1)]u(k-1), -g_1(k-1), \\
& h[u(k-1)]u(k-1), h[u(k-1) - n_{L1}]u(k-1), \\
& -g_2(k-1), \\
& v(k-2), \dots, v(t-m), -x(k-1), \dots, \\
& -x(t-n), h[x(k)]x(k), h[N_{R1} - x(k)]x(k), \\
& -G_1(k), h[x(k) - N_{L1}]x(k), -G_2(k)\}
\end{aligned} \tag{21}$$

and the parameter vector as:

$$\begin{aligned}
\theta^T = & [s_{R1}, s_{R2} - s_{R1}, n_{R1}, s_{L1}, s_{L2} - s_{L1}, \\
& n_{L1}, b_2, \dots, b_m, g_1, \dots, g_n, \\
& S_{L1} - 1, S_{R2} - 1, N_{R1}, S_{L2} - S_{L1}, N_{L1}]
\end{aligned} \tag{22}$$

the Hammerstein-Wiener model with piecewise-linear nonlinearities can be written in the concise form:

$$y(k) = \varphi^T(k) \cdot \theta + e(k) \tag{23}$$

where $e(k)$ is an additive noise and the problem of model parameters estimation can be solved as a pseudo-linear estimation problem [34]. In the parameter vector, the f_1, \dots, f_n and b_1, \dots, b_m refer to the parameters of the transfer function polynomials.

Generalising the piecewise-linear approach and allowing a finite amount of segments, result in the so called multisegment piecewise-linear model. This is achieved by altering eqs. (10) and (12) and defining the following variables:

$$\begin{aligned}
g_{1,i}(k) &= (s_{R,i} - s_{R,i-1})h[n_{R,i-1} - u(k)] \\
g_{2,j}(k) &= (s_{L,j} - s_{L,j-1})h[u(k) - n_{L,j-1}]
\end{aligned} \tag{24}$$

$i = 1, \dots, n_R$ and $j = 1, \dots, n_L$, where $|s_{R,i}| < \infty$ $|s_{L,j}| < \infty$ are the segment slopes, $0 \leq n_{R,i} < n_{R,i+1} < \infty$ are the constants that represent the positive inputs, and

$-\infty < n_{L,j+1} < n_{L,j} \leq 0$ represent the negative inputs. The output equation for the general multisegment piecewise-linear characteristics are defined as follows:

$$\begin{aligned}
x(k) = & \sum_{i=1}^{n_R} \{(s_{R,i} - s_{R,i-1})h[n_{R,i-1} - u(k)]u(k) \\
& - n_{R,i-1}g_{1,i}(k)\} \\
& + \sum_{j=1}^{n_L} \{(s_{L,j} - s_{L,j-1})h[u(k) - n_{L,j-1}]u(k) \\
& - n_{L,j-1}g_{2,j}(k)\}
\end{aligned} \tag{25}$$

where

$$\begin{aligned}
0 \leq n_{R,1} < n_{R,2} < \dots < n_{R,n_R} < \infty \\
-\infty < n_{L,n_L} < \dots < n_{L,2} < n_{L,1} \leq 0
\end{aligned} \tag{26}$$

and $s_{R,0} = n_{R,0} = s_{L,0} = n_{L,0}$ to coincide and prevent discontinuities in zero. Now half-substituting eq. (25) into eq. (8) for the separated $x(k)$ gives the following multisegment piecewise-linear output equation:

$$\begin{aligned}
y(k) = & \sum_{i=1}^{n_R} \{(s_{R,i} - s_{R,i-1})h[n_{R,i-1} - u(k)]u(k) \\
& - n_{R,i-1}g_{1,i}(k)\} \\
& + \sum_{j=1}^{n_L} \{(s_{L,j} - s_{L,j-1})h[u(k) - n_{L,j-1}]u(k) \\
& - n_{L,j-1}g_{2,j}(k)\} \\
& + \sum_{i=1}^n b_i x(k-i) - \sum_{j=1}^m f_j y(k-j)
\end{aligned} \tag{27}$$

III. EXPERIMENTS

In general, dimensions and material properties are key within the development of a mathematical model of a vibration isolator by using for example a finite element approach [40]–[42]. However, no material properties or exact specimen dimensions are known in this case. This prevents the use of purely numerical models and imposes the use of models that are based on experimentally obtained data.

Furthermore, for the real-time application method of thrust prediction, a system identification approach is preferable over a finite element method [43].

For practical applications of this concept, it is important to know the characteristics of the vibration isolator, and what influences these characteristics, before the identification process is initiated. Environmental or operational conditions potentially influence the characteristics and require compensation within the model, leading to an additional model input. Examples of these conditions are engine vibrations, varying engine weight and operating temperature.

The experiments are performed on a customised MTS-831 elastomer test system as shown in fig. 5. The MTS test

machine permits experiments in one dimension, However, for the experiments, two dimensions are required as the main engine vibrations are perpendicular to the thrust force direction. This extra dimension is custom made for this experiment and clamped into the MTS machine. The figure shows the vibration isolator (1) which is bolted to the lower adaptor (2) which is connected to the MTS load cell (7) using a thread to MTS connector (6). The additional cylinder (4) is used to simulate the thrust force in the experiments and contains a load cell to measure the exerted force. This cylinder is supported by the lower adaptor (2). The deformation due to this thrust force is measured using a linear variable differential transformer (LVDT) with a resolution of $0.001 \mu m$ and is mounted on bracket (5). The upper adaptor (3) is connected to the MTS hydraulic cylinder (8) using a connector (6). This cylinder is

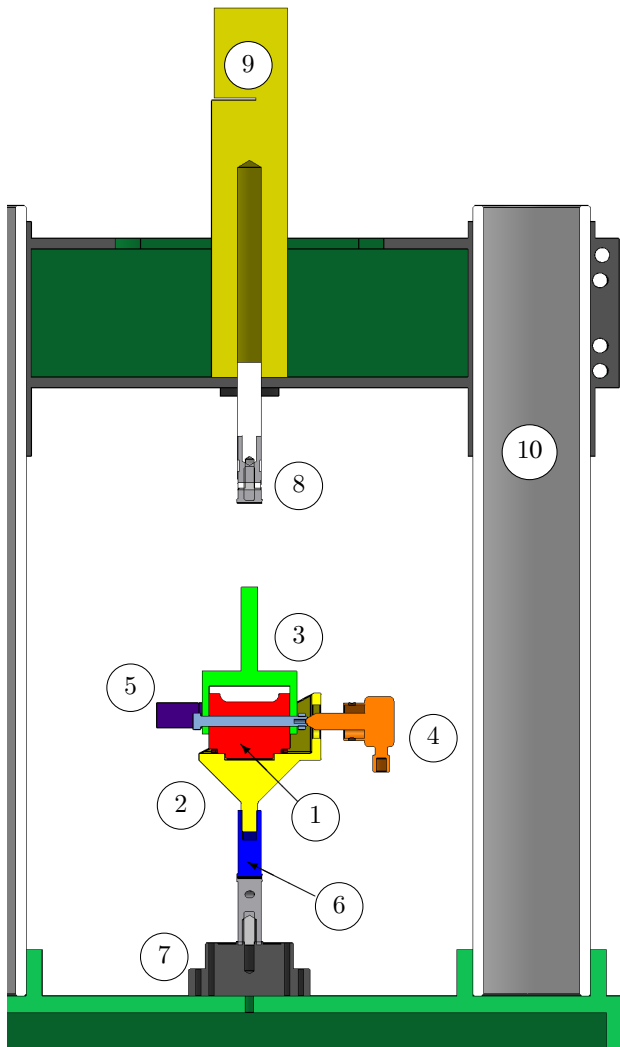


Fig. 5: Experiment setup cross section view. ① vibration isolator ② lower adaptor ③ upper adaptor ④ hydraulic cylinder ⑤ LVDT bracket ⑥ MTS connector ⑦ load cell ⑧ MTS hydraulic cylinder ⑨ MTS LVDT ⑩ MTS-831 elastomer test system.

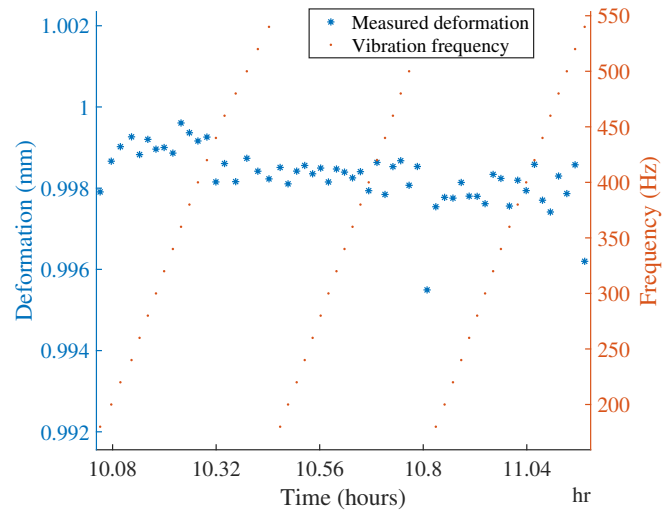


Fig. 6: Influence of frequency and amplitude on the measured deformation. In this graph, the mean deformation over a period of 60 seconds at various frequency and amplitude conditions is shown. Each frequency sweep is performed with an increased amplitude varying from 0.02 to 0.04 mm. The simulated engine weight and thrust force are constant. No correlation between the frequency or amplitude changes and the measured deformation is noticed.

electronically controlled and simulates the engine vibrations up to 550 Hz . The cylinder position is measured by the MTS LVDT (9). The MTS-831 test system (10) is combined with a Thermotron temperature control chamber, which is not shown in the cross-section view.

An additional experiment setup allows for an alternative mounting position of the vibration isolator, aligning the vibration isolator with the MTS hydraulic cylinder. This setup is used for the identification experiments and to determine the influence of temperature on the stress-strain curve in the thrust direction. The custom-made experiment programs are executed by the system controller looping through different frequencies, amplitudes, and preloads.

A. Characterisation experiments

These experiments are constructed to determine the influence of the environmental and operational conditions; frequency, amplitude, engine weight, and temperature on the isolator deformation that is caused by the thrust force. The influence of each individual parameter is investigated, assuming that two parameters without influence also do not influence the results when combined.

Using the MTS control software, the frequency and amplitude of the input vibration are programmed and controlled. In this same program, the simulated engine weight is controlled, which is superimposed on the vibrations. The engine weight is a function of the directional accelerations and, as a result of flight manoeuvres, is not constant. The temperature of the test setup is controlled by an external controller that only permits constant temperatures. The thrust force of the hydraulic cylinder (4) is controlled by a custom-made manual control system.

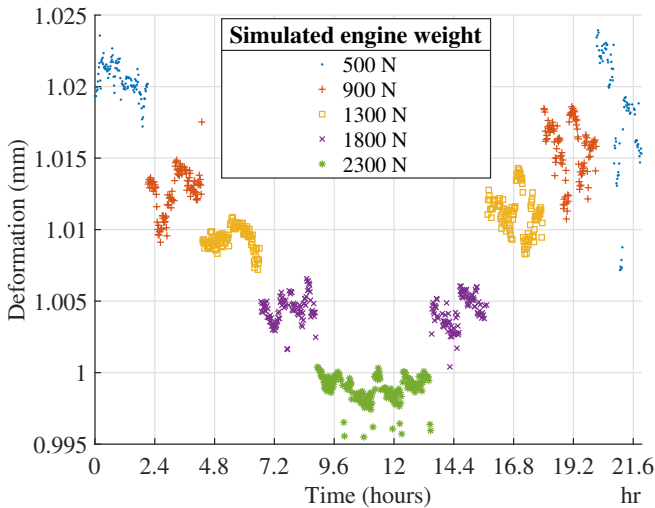


Fig. 7: Influence of engine weight on measured deformation
In this graph, the influence of varying engine weight is shown. Increasing the engine weight results in a decrease in measured thrust force deformation. The simulated thrust force is constant at 6 kN over the experiment. Note that the weight force is perpendicular to the thrust force.

The characterisation experiments showed that the frequency and amplitude in the operational range do not influence the isolator deformation caused by a certain force, as depicted in fig. 6. The engine weight was found to influence the measured deformation for a given simulated thrust force by a small but measurable margin. Increasing the engine weight by 500 N resulted in a $5\text{ }\mu\text{m}$ reduction of deformation in the thrust force direction, as depicted in fig. 7. This corresponds to a thrust measurement error of about 30 N at a maximum thrust force of 6 kN . As an example, a flight condition that results in twice the gravitational acceleration, causes a maximum measurement error of 1.6% when compared to a steady forward flight.

Each measurement point in figs. 6 and 7 is an average of a 60 second recording, during which, all parameters are constant. The maximum variation of each sensor, during this period of time, is recorded. For the vibration isolator deformation, the average of this variation is $0.0746\text{ }\mu\text{m}$, with a maximum variation of $1.1\text{ }\mu\text{m}$ over the 21 hours of measurements. The variation of the thrust load cell measurement is 27.02 N on average, with a maximum variation of 118 N . It is noticeable that the dynamic variation is strongly correlated to the applied frequency. This is in line with the expectations, as the hydraulic cylinder rod has a vibration dependent loading, which is caused by the inertia of the cylinder.

The influence of temperature difference is measured by mounting the vibration isolator such that the thrust force is simulated with the MTS cylinder (8). This enables experimental setup to automatically vary thrust force over a larger period of time. In this setup, the vibration isolator is cooled down from $80\text{ }^\circ\text{C}$ to $30\text{ }^\circ\text{C}$ in 15 hours. After correcting for the contraction in the metal connection components, it was found that this temperature decrease does not influence the magnitude of deformation that is caused by the simulated thrust force, and is depicted in fig. 8.

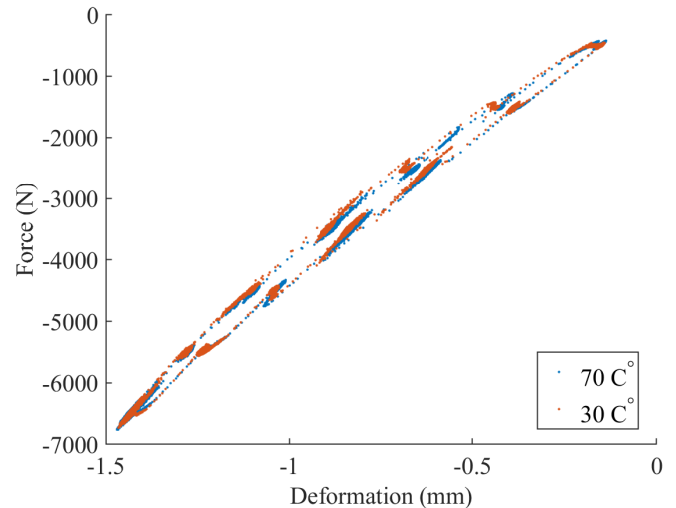


Fig. 8: Influence of temperature on the measured deformation. The graph depicts a stepwise thrust force-deformation characteristics of the vibration isolator at different temperatures. The shape of the force-deformation curve is the same at both temperatures. Indicating, that temperature variations have no influence on the magnitude of deformation caused by the thrust force.

B. Identification experiments

Identification is modelling based on experiments [44]. The purpose of identification experiments is to collect relevant information about the process dynamics. With the identification data, a mathematical model is constructed that estimates the force input of the vibration isolator based on the measured deformation.

The force-deformation curve in the thrust direction is found to describe a hysteresis loop, indicating a nonlinearity in the input output behaviour. To map the complete surface of the hysteresis, a program is generated that steps through random values in the operational thrust range of 400 N to 6.5 kN . Additional experiments analyse the system response to sinusoidal thrust shapes at various frequencies.

IV. MODEL RESULTS

The models intend to reconstruct the applied force with a single input, which is the measured isolator deformation. For successive models, it is possible to use the engine weight as an input to compensate for the error of in-flight manoeuvres. In the current test setup, it is not possible to simulate dynamic thrust and dynamic weight simultaneously, as these forces are perpendicular to each other and one is simulated by a manually powered hydraulic system.

The data sets, that are used to generate the models and later validate the models, are generated by stepping through random thrust forces. Each force step remains constant for several minutes to include the low frequency responses, such as the dynamic stress-relaxation. Note that all mentioned forces are per vibration isolator and not per engine.

The simulated thrust force and resulting deformation is shown in fig. 9. Only one hour of the validation data is shown for the sake of clarity.

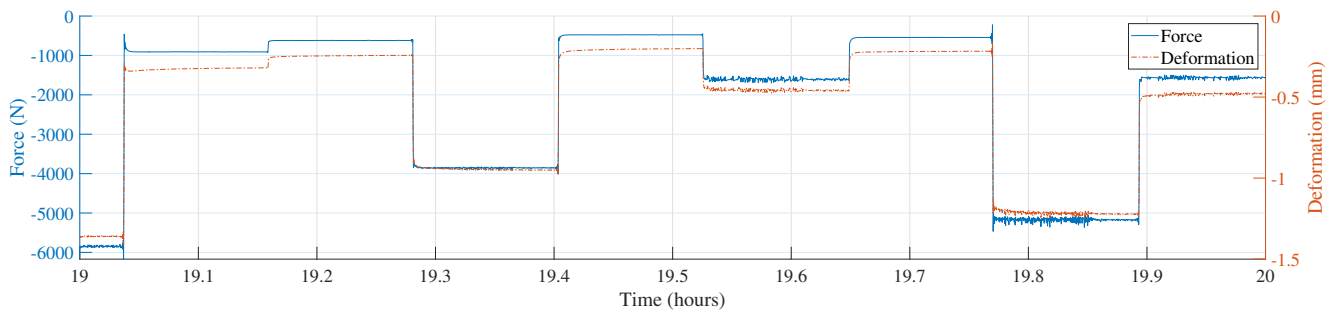


Fig. 9: **Simulated thrust force and measured deformation.** One hour of simulated thrust force and deformation of the validation data. On the left-hand side, the simulated thrust force axis is depicted. The simulated thrust force steps through random values in the operational thrust range of the engine. The right-hand axis shows the measured magnitude of deformation due to the implied thrust force. The stress relaxation is best noticed after the first thrust step, as the deformation gradually reduces over time.

Implementing the Voigt and Maxwell models in the MathWorks® Simscape™ environment, resulted in poor model performances, with root mean square errors between 150 and 300 N on the validation data. Using a finite amount of Maxwell in parallel or Voigt models in series facilitates accurate approximations of real systems [45]. However, the manual tuning of the individual components causes this approach to be a non-practical one and is therefore not further investigated.

The static nonlinear model is approximated with a third order polynomial using the ordinary least squares method and yielded a root mean square error of 103 N on the validation data. A polynomial order, higher than three, was found to not further improved the performance. The model shows large errors in the dynamic parts of the data and, as expected, no creep or stress relaxation is modelled. The benefit of this model is the high calculation performance. Constructing the model with $N = 2.9 \cdot 10^6$ samples, and predicting the output of the validation data with $N_{val} = 13.4 \cdot 10^6$ samples, is performed in 0.7 seconds on a standard laptop.

The linear dynamic output error model features improved dynamic model behaviour. However, the overall performance decreased to a root mean square error of 142 N on the validation data, using a second order polynomial transfer function. Any increase in the order of the transfer function resulted in no further improvement. This is a clear indication that the system contains nonlinear behaviour.

Combining the fourth order polynomial static nonlinear model and a second order dynamic linear model, respectively, yields a nonlinear dynamic model or so-called Hammerstein model. This model renders a root mean square error of 65 N on the validation data. Increasing the transfer function to a sixth order, increased the performance to 59 N error. A permutation of the static nonlinear model and the dynamic linear model results in the Wiener model and renders a root mean square error of 61 N on the validation data.

A logical evolution is combining these Hammerstein and Wiener models, resulting in the Hammerstein-Wiener model. Using the polynomial estimation for the Hammerstein-Wiener system nonlinearities yielded no improvement compared to the Hammerstein model. Introducing a ten segment piecewise-linear approximation for both the input and output nonlinearity, further reduced the root mean square error to 56 N . An overview of the model performances are found in table 1.

A root mean square error under 60 N suggests a model error under 1% of the maximum thrust force. Calculating the average of the absolute model error on 37 hours of validation data in the expected operation range ($> 2 \text{ kN}$) is 1.1%. The currently most accurate and widely implemented gas generator method achieves an accuracy of about 3% [15], [16]. Note that the Hammerstein-Wiener model does not account for sensor errors and uncertainty. Although, with the right equipment, this is an order of magnitude lower than the model error.

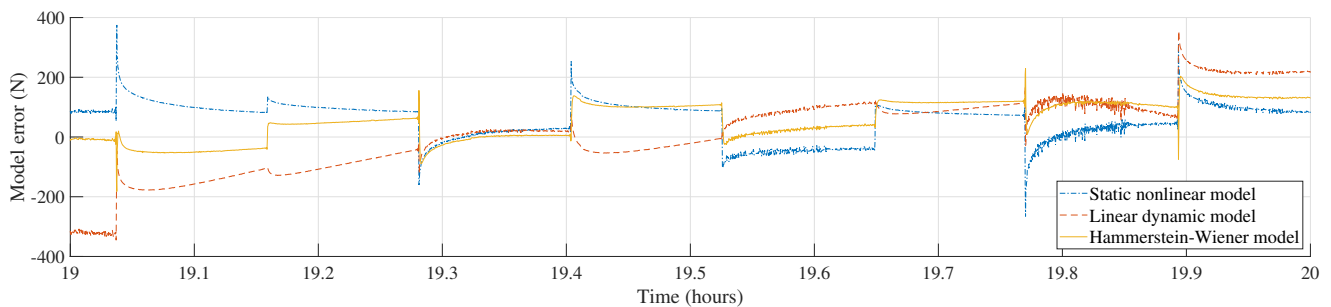


Fig. 10: **Model error comparison.** The model errors of one hour of previously depicted validation data. The static nonlinear model renders large errors at large thrust force steps in the experimental data, which is expected from a static model. The linear dynamic model improves on the dynamic components, while the overall performance decreases when compared to the static nonlinear model. The Hammerstein-Wiener model provides the lowest model error. The observed noise is caused by either the system controller or external machines that is connected to the same hydraulic system.

Model	RMSE (N)
Physical models	150
Static nonlinear	103
Dynamic linear	143
Hammerstein	59
Wiener	61
Hammerstein-Wiener	56
Piecewise-linear	

Table 1: Model performance on validation data.

All models are constructed in the MathWorks® environment. The ordinary least square estimation is performed using the Moore-Penrose pseudoinverse to calculate the covariance matrix. The linear dynamic transfer functions and nonlinear models are constructed using System Identification Toolbox™ commands. The polynomial orders, and piecewise-linear segment count, are manually determined to achieve a parsimonious model.

V. MODEL COMPARISON

In order to gain an understanding of the model characteristics, a visualisation of each model output is depicted in fig. 11. In this graph, the output prediction of a static nonlinear, dynamic linear and a Hammerstein-Wiener model are shown

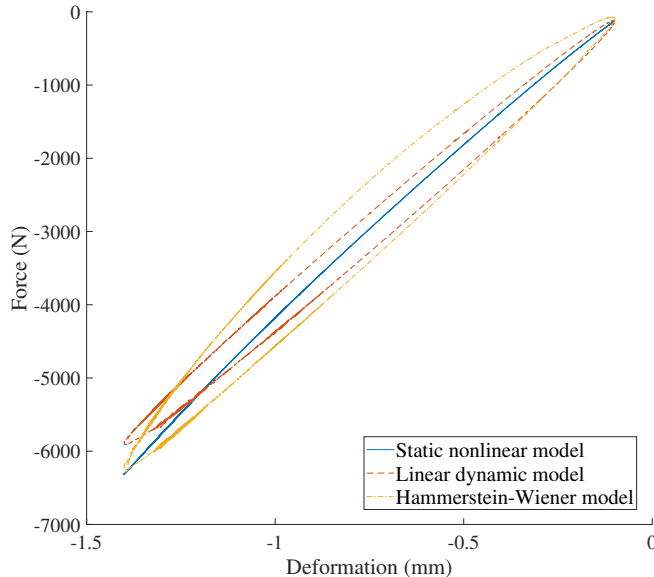


Fig. 11: **Comparison of model characteristics on sine wave input.** In this graph, the characteristics of the three model approaches is depicted for the interest of comparison and not for practical use. The static nonlinear model is illustrated by the solid line, where the absence of system dynamics is recognised by the path of the rebound stroke, which is the same as the compression stroke. The linear dynamic model is recognised by the dashed line and angled symmetric ellipse shape. The Hammerstein and Wiener models produces a curved ellipse, which approximates the characteristics of the vibration isolator with high accuracy, and conceals the measurements as a result. The noise at higher load levels is caused by the hydraulic control of the test bench.

for a sinusoidal input. The shown models are generated for the interest of comparison, and have no practical application.

Insight into the model characteristics allows us to recognise these characteristics in the model errors shown in fig. 10. Observations show large peaks in the static model at large thrust force steps. Which is expected from a static model. The linear dynamic model improves on the dynamic components, while the overall performance decreases when compared to the static nonlinear model. An example is the first few minutes of the error data, which shows a large error for the linear dynamic model. The force load at this moment is almost at the maximum, which corresponds to the large model discrepancy that is shown in fig. 11. The Hammerstein-Wiener model, which is estimated on the same constant frequency, has a root mean square error of 13 N, and overlaps the measurement data.

For a practical use, no sinusoidal inputs are given. Thrust inputs are performed in a stepwise fashion, accordingly, the identification experiments are performed using random step inputs. Intuitively, one would expect this to describe a random pattern within the boundaries of the hysteresis. Where a higher rate of change follows a *rounder* hysteresis due to the viscous component of the material, and a lower rate of change would approach the centreline of the hysteresis, which is traced by the static nonlinear model. Instead, no full return to this centreline is observed, as the used material is silicone rubber, which is a viscoelastic solid and affected by internal material friction, that results in energy dissipation, and forestalls a fully elastic return to the static centreline. This effect is clearly observed in fig. 8, where the time in between the step inputs is 10 minutes.

The Hammerstein-Wiener model allows to estimate the initial dynamics of a step response. By implementing a higher order linear dynamic model, the internal friction is approximated by a sluggish return to the steady state of the step response. Utilising a 6th order polynomial as numerator and 4th order polynomial as denominator for the linear dynamic model, the 1% settling time is reached in the order of hours. Consequently, better estimation results are observed when compared to the nonlinear static and linear dynamic approach.

The prediction of the thrust model on experiments with sinusoidal thrust input showed deteriorated prediction performances. This indicates that the dynamic behaviour of the vibration isolator is not captured with enough detail. If one intends to perform test flights with sinusoidal thrust inputs, additional identification experiments with frequency sweeps are required. These can be performed on either a biaxial test setup, an adjusted engine rig, or an actual aircraft with a static run. Performing these experiments with an actual engine provides, naturally, the best representation of the engine dynamics. Moreover, the maximum rate of change for a jet engine is limited by the engine spin up time, and dependent on the conditions, may take up to 8-13 seconds from idle to 95% rated take-off thrust for this particular engine [46], [47].

One might wonder if the additional model complexity of the Hammerstein-Wiener model is justified given the simplicity of the static nonlinear model and the gained performance. Both models lead to thrust estimation, it is the application that determines which model would be the best suited.

For the static nonlinear model, the largest error is observed in the first half a minute after a thrust step, and reduces gradually over the following minutes. For the Hammerstein-Wiener system, generally a one-second peak is observed after a thrust step input, followed by relatively stable and low error prediction of the thrust.

If one intends to adjust the throttle settings once every hour, a static model is expected to show adequate prediction performance, and the effort of implementing the Hammerstein-Wiener system should be avoided. If, on the other hand, parabolic test flight are part of the flight program, the Hammerstein-Wiener model highly recommended as the throttle is adjusted from full power, to idle, and back to full power in quick succession. Furthermore, the time to execute test flight manoeuvres is confined, and waiting up to ten minutes after each throttle adjustment to lower the thrust measurement error is not cost effective, or might not be feasible.

Apart from this, is a Hammerstein-Wiener model capable of capturing the engine transient response, which is an important parameter to monitor the engine condition and determine deteriorated performances [48].

VI. CONCLUSION

A novel method for low-cost in-flight thrust measurement is presented. Facilitating a direct thrust reading is interesting for several areas of aerospace research, examples are the system identification, aerodynamics, or propulsion research fields. The proposed method utilises the two engine vibration isolators that convey the generated jet engine thrust to the airframe. The vibration isolators exploit the material characteristics of silicone rubber for noise abatement and vibration reduction purposes. Consequently, a deformation of the vibration isolator is observed due to the applied jet engine thrust force. This poses the question of whether one can draw a relevant analogy between the deformation and the imposed thrust force.

Inclined to answer this question, an engine vibration isolator is subjected to numerous experiments of either the characterisation or identification category. The characterisation experiments are executed to determine the influence of environmental and operational conditions on the deformation and thrust force analogy. The examined conditions include the operation temperature, engine vibrations, and varying engine weight. The identification experiments intend to capture the dynamics of the vibration isolator and serve as input for the mathematical model construction.

The characterisation experiments revealed an independence of the operation temperature and engine vibration, with the proposed analogy. The engine weight exhibited a measurable effect on the deformation at a constant thrust force. Given that the engine is exposed to double the gravitational acceleration, a maximum thrust measurement error of 1.6% is observed.

The mathematical thrust model, based on the data that is obtained during the identification experiments, intends to apprehend the nonlinear dynamic behaviour of the vibration isolator system. The best performing model construction is a compounding of static nonlinear models and a dynamic linear model, resulting in a Hammerstein-Wiener system estimator.

In the developed model, the static system nonlinearities are approximated by implementing a piecewise-linear approach, and the linear system dynamics are estimated by an output error transfer function model. The model structure implies a generic and robust model approximation and accurate system output estimation for sufficiently smooth systems. Consequently, a system output estimation error, in the operational thrust range, of 1.1 % is observed on the validation data.

To justify the additional complexity of the dynamic nonlinear, over the static nonlinear approach, the intended application is decisive. If one intends to perform multiple throttle alterations within the timespan of half an hour, the model dynamics are essential. Additionally, a dynamic nonlinear model facilitates the monitoring of the engine transient response characteristics and determine excessive performance degradation.

To conclude, the presented cost effective method of direct thrust prediction is found highly feasible, and paves a way to support the system identification, aerodynamic research and accelerate the development of low emission, or hybrid fuel engines advancing the aviation industry and preparing for the future.

OUTLOOK

The implementation of the Bouc-Wen or the Preisach hysteresis model into the Hammerstein-Wiener could be considered in further studies. This would presumptively improve the estimation of the internal friction hysteresis, since the current model only approximates the hysteresis with a low frequency step response.

Research into the ageing characteristics of the vibration isolator is beneficial for the practical application of the concept. This knowledge allows one to determine the required calibration interval, and possible necessary model corrections.

Identification experiments on a biaxial dynamic experiment setup enable the capture of the influence of the engine weight and thrust force in one dataset. This enables the construction of a multiple input, single output model which accounts for varying engine weight. Additionally, identification experiments with frequency sweeps are required to improve the dynamic response of the model. An engine that is mounted in a test stand facilitates the simultaneous execution of both identification experiments in a realistic setup.

Further research is required to estimate the engine weight during flight manoeuvres, based on the measured accelerations and the positioning of the engine.

Combining the prediction data of dissimilar sources using a Kalman filter could improve the overall thrust prediction performance.

ACKNOWLEDGEMENT

The author gratefully acknowledges financial support from the flying laboratory (PH-LAB) department of the Delft University of Technology (TU Delft). Gratitude is expressed towards the Delft Aerospace Structures and Materials Laboratory (DASML) for the use of the experiment machines and support. Thanks go to dr. ir C.C. de Visser, the supervisor of this research.

REFERENCES

- [1] AGARD, *Guide to In-Flight Thrust Measurement of Turbojets and Fan Engines*. Advisory Group for Aerospace Research and Development, 1979.
- [2] M. Chen, "Static thrust measurement for propeller-driven light aircraft," in *Proceedings of the 2012 International Conference on Computer Application and System Modeling, ICCASM 2012*, 2012.
- [3] M. Bronz, H. G. de Marina, and G. Hattenberger, "In-flight thrust measurement using on-board force sensor," in *AIAA Atmospheric Flight Mechanics Conference, 2017*, 2017.
- [4] G. L'Erario, L. Fiorio, G. Nava, F. Bergonti, H. A. O. Mohamed, E. Benenati, S. Traversaro, and D. Pucci, "Modeling, Identification and Control of Model Jet Engines for Jet Powered Robotics," *IEEE Robotics and Automation Letters*, 2020.
- [5] T. R. Conners and R. L. Sims, "Full flight envelope direct thrust measurement on a supersonic aircraft," in *34th AIAA/ASME/SAE/ASEE Joint Propulsion Conference and Exhibit*, 1998.
- [6] H. Muhammad, W. Kuntjoro, and B. E. Sritjahjono, "In-Flight Thrust Determination by Load Measurement on the Engine Mounting System," in *Proceedings of the 22nd International Congress of Aeronautical Sciences*, 2000.
- [7] M. F. Neef, C. P. Fritzen, and G. Schuhmacher, "Evaluation of mount loads in dynamic testing of a jet engine," *Mechanical Systems and Signal Processing*, vol. 17, no. 3, pp. 665–681, 2003.
- [8] M. Bauer, J. Friedrichs, D. Wulff, and C. Werner-Spatz, "Measurement Quality Assessment of an On-Wing Engine Thrust Measurement System," in *Proceedings of the ASME Turbo Expo*, 2018.
- [9] X. Lei, Q. Zhang, M. Wen, R. Ren, and D. Lei, "Mount thrust measurement technique for aero-engines and its tests," *Hangkong Xuebao/Acta Aeronautica et Astronautica Sinica*, 2017.
- [10] X. Lei, M. Li, Q. Zhang, Y. Gao, and M. Wen, "Direct thrust measurement flight test of aero-engine," *Hangkong Dongli Xuebao/Journal of Aerospace Power*, 2018.
- [11] W. F. Kimzey, S. Wehofer, and E. E. Covert, *Gas Turbine Engine Performance Determination*. AIAA, jan 1985.
- [12] R. Abernethy, J. Roberts, J. Lewis, D. Clicken, R. Morin, J. Mancini, S. R. S. Wehofer, E. Rooney, E. Wilt, and B. Ringhiser, "In-flight thrust determination and uncertainty SP-647," in *Exposition, Aerospace Technology Conference & Engineers., Society of Automotive*. Warrendale, PA: Society of Automotive Engineers, 1986.
- [13] J. R. P. Negrão, R. E. Fanton, R. P. de La Fuente, and J. R. Barbosa, "In-Flight Thrust Determination," in *SAE Technical Paper*, 11 1998.
- [14] G. Di Fiore Dos Santos, R. J. Lewis, and J. R. Barbosa, "Residual error for in-flight thrust determination," in *SAE Technical Papers*, 2000.
- [15] P. Del Mónaco Monteiro, R. M. Machiaverni, C. Bringhenti, and J. T. Tomita, "In-flight thrust determination for high-bypass-ratio turbofan using residual error methodology," *Journal of the Brazilian Society of Mechanical Sciences and Engineering*, vol. 40, no. 2, 2018.
- [16] D. L. Hughes, "Comparison of Three Thrust Calculation Methods Using In-Flight Thrust Data," *NASA Technical Memorandum*, pp. 62–85, 1981.
- [17] R. J. Ray, *Evaluating the dynamic response of in-flight thrust calculation techniques during throttle transients*. Washington: NASA, 1994.
- [18] M. Athavale, B. Steinetz, and R. Hendricks, "Gas turbine primary-secondary flowpath interaction - transient, coupled simulations and comparison with experiments," in *37th Joint Propulsion Conference and Exhibit*. AIAA, jul 2001.
- [19] Z. hong Chang, "Numerical simulation of steady and transient working progress in aviation gas turbine engine," in *AIAA SPACE 2009 Conference & Exposition*. AIAA, jun 2009.
- [20] N. R. P. P. Li, Y. G.; L. MacCallum, "Pressure waves in volume effect in gas-turbine transient-performance models," *Journal of Propulsion and Power*, vol. 17, pp. 706–710, 2001.
- [21] M. B. Tischler and R. K. Rempke, *Aircraft and Rotorcraft System Identification*. AIAA, 2006.
- [22] R. V. Jategaonkar, *Flight Vehicle System Identification - A Time Domain Methodology*, ser. Progress in Astronautics and Aeronautics, Volume 216. AIAA, 2006.
- [23] Textron, *Cessna model 550 Illustrated Parts Catalog*. Wichita: Textron Aviation Inc., 2020.
- [24] H. F. Brinson and L. C. Brinson, *Polymer Engineering Science and Viscoelasticity*. Springer, 2015.
- [25] R. S. Lakes, *Viscoelastic Solids*. Boca Raton, Florida: CRC Press, 1999.
- [26] O. Nelles, *Nonlinear System Identification: From Classical Approaches to Neural Networks, Fuzzy Models, and Gaussian Processes*, 2nd ed. Springer, 2021.
- [27] A. Hammerstein, "Nichtlineare integralgleichungen nebst anwendungen," *Acta mathematica*, vol. 54, pp. 117–176, 1930.
- [28] N. Wiener and T. Teichmann, "Nonlinear problems in random theory," *Physics Today*, vol. 12, no. 8, p. 52, 1959.
- [29] S. Boyd and L. Chua, "Fading memory and the problem of approximating nonlinear operators with volterra series," *IEEE Transactions on circuits and systems*, vol. 32, no. 11, pp. 1150–1161, 1985.
- [30] L. Ljung, *System Identification: Theory for the User*, 2nd ed. Prentice Hall, 1999.
- [31] J. Vörös, "Identification of nonlinear dynamic systems using extended hammerstein and wiener models," *Control Theory Adv. Technol.*, vol. 10, no. 4, pp. 1203–1212, 1995.
- [32] J. Vörös, "Parameter identification of discontinuous hammerstein systems," *Automatica*, vol. 33, no. 6, pp. 1141–1146, jun 1997.
- [33] J. Vörös, "Identification of hammerstein systems with time-varying piecewise-linear characteristics," *IEEE Transactions on Circuits and Systems II: Express Briefs*, vol. 52, pp. 865–869, 2005.
- [34] F. G. Er-Wei Bai, *Block-oriented Nonlinear System Identification*, 1st ed., ser. Lecture Notes in Control and Information Sciences 404. Springer-Verlag London, 2010.
- [35] J. Vörös, "Recursive identification of hammerstein systems with discontinuous nonlinearities containing dead-zones," *IEEE Transactions on Automatic Control*, vol. 48, pp. 2203–2206, 12 2003.
- [36] J. Vörös, "Parameter identification of wiener systems with discontinuous nonlinearities," *Systems & Control Letters*, vol. 44, pp. 363–372, 2001.
- [37] M. Rantzer, A.; Johansson, "Piecewise linear quadratic optimal control," *IEEE Transactions on Automatic Control*, vol. 45, pp. 629–637, 2000.
- [38] J. Vörös, "Modeling and parameter identification of systems with multisegment piecewise-linear characteristics," *IEEE Transactions on Automatic Control*, vol. 47, no. 1, pp. 184–188, 2002.
- [39] J. Vörös, "Iterative algorithm for parameter identification of hammerstein systems with two-segment nonlinearities," *IEEE Transactions on Automatic Control*, vol. 44, 1999.
- [40] K. Menard and N. Menard, *Dynamic Mechanical Analysis*. CRC Press, 2020.
- [41] M. Sjöberg and L. Kari, "Nonlinear isolator dynamics at finite deformations: An effective hyperelastic, fractional derivative, generalized friction model," *Nonlinear Dynamics*, 2003.
- [42] M. Sepe, *Dynamic mechanical analysis for plastics engineering*. William Andrew Inc., 1998.
- [43] F. A. Zanette, João Vitor; de Almeida, "Realsysid: A software tool for real-time aircraft model structure selection and parameter estimation," *Aerospace Science and Technology*, vol. 54, pp. 302–311, 2016.
- [44] T. B. P. Yucai Zhu PhD, *Identification of Multivariable Industrial Processes: for Simulation, Diagnosis and Control*, 1st ed., ser. Advances in Industrial Control. Springer-Verlag London, 1993.
- [45] E. Riande, R. Díaz-Calleja, M. G. Prolongo, R. M. Masegosa, and C. Salom, *Polymer Viscoelasticity : Stress and Strain in Practice*, D. Hudgin, Ed. New York: Marcel Dekker Inc., 2000.
- [46] FAA, "Airplane flying handbook faa-h-8083-3b." 2016.
- [47] D. Boyd, "Adaptation of a small commercial fan jet trainer for military applications," in *Turbo Expo: Power for Land, Sea, and Air*, vol. 79054. ASME, 1990.
- [48] T. Grönstedt and Y. Zhao, "A numerically efficient method for transient gas turbine performance estimation," in *40th AIAA/ASME/SAE/ASEE Joint Propulsion Conference and Exhibit*. AIAA, jun 2004.



Robert Poppe was born in Vlissingen, The Netherlands in July 1994. He obtained the aircraft mechanic degree at the Aircraft Maintenance & Training School (AM&TS) in 2014 in Hoogerheide, the Netherlands. He obtained the Bachelor degree in Aeronautical Engineering in 2018 at the Inholland University of Applied Sciences in Delft, the Netherlands. In 2019, he started the Control & Simulation Master at the Aerospace Faculty of the Delft University of Technology (TU Delft). He maintained a part-time job as an aircraft mechanic throughout his

student life, resulting in a unique and requisite skill set for the presented study.

References

- Abernethy, R., Roberts, J., Lewis, J., Clicken, D., Morin, R., Mancini, J., ... Ringhiser, B. (1986). In-flight thrust determination and uncertainty SP-647. In *Exposition, aerospace technology conference & engineers., society of automotive*. Warrendale, PA: Society of Automotive Engineers.
- Adams, G. R., Thompson, J. W., Abernethy, R. B., Biesiadny, T., Havey, C. T., Steurer, J. W., ... Williams, D. D. (1983). Application of in-flight thrust determination uncertainty. In *Sae technical papers*. doi: 10.4271/831439
- AGARD. (1979). *Guide to In-Flight Thrust Measurement of Turbojets and Fan Engines*. Advisory Group for Aerospace Research and Development.
- Athavale, M., Steinetz, B. & Hendricks, R. (2001, jul). Gas turbine primary-secondary flowpath interaction - transient, coupled simulations and comparison with experiments. In *37th joint propulsion conference and exhibit*. American Institute of Aeronautics and Astronautics. doi: 10.2514/6.2001-3627
- Bauer, M., Friedrichs, J., Wulff, D. & Werner-Spatz, C. (2018). Measurement Quality Assessment of an On-Wing Engine Thrust Measurement System. In *Proceedings of the asme turbo expo*. doi: 10.1115/GT2018-76496
- Baz, A. M. (2019). *Active and Passive Vibration Damping*. Wiley. doi: 10.1002/9781118537619
- Botman, M. (1980). Vibration aspects of small turbine engines in aircraft installations. In *Sae technical papers*. doi: 10.4271/800617
- Boyd, D. (1990). Adaptation of a small commercial fan jet trainer for military applications. In *Turbo expo: Power for land, sea, and air* (Vol. 79054).
- Boyd, S. & Chua, L. (1985). Fading memory and the problem of approximating nonlinear operators with volterra series. *IEEE Transactions on circuits and systems*, 32(11), 1150–1161.
- Brinson, H. F. & Brinson, L. C. (2015). *Polymer Engineering Science and Viscoelasticity*. Springer. doi: 10.1007/978-1-4899-7485-3
- Bronz, M., de Marina, H. G. & Hattenberger, G. (2017). In-flight thrust measurement using on-board force sensor. In *Aiaa atmospheric flight mechanics conference, 2017*. doi: 10.2514/6.2017-0698
- Bueche, F. (1961). Molecular Basis for The Mullins Effect. *Rubber Chemistry and Technology*. doi: 10.5254/1.3540224
- Chang, Z. (2009, jun). Numerical simulation of steady and transient working progress in aviation gas turbine engine. In *AIAA SPACE 2009 conference & exposition*. American Institute of Aeronautics and Astronautics. doi: 10.2514/6.2009-6657
- Chen, M. (2012). Static thrust measurement for propeller-driven light aircraft. In *Proceedings of the 2012 international conference on computer application and system modeling, iccasm 2012*. doi: 10.2991/iccasm.2012.165
- Connors, T. R. & Sims, R. L. (1998). Full flight envelope direct thrust measurement on a supersonic aircraft. In *34th aiaa/asme/sae/asee joint propulsion conference and exhibit*. doi: 10.2514/6.1998-3872
- Cook, D. L. (1972, 2). Development of the JT15D-1 Turbofan Engine. In *Sae technical paper series*. SAE International. doi: 10.4271/720352
- Covert, E. E., James, C. R. & Kimzey, W. F. (2000). *Thrust and Drag : Its Prediction and Verification* (NV - 1 onl ed.). Reston: American Institute of Aeronautics and Astronautics. Retrieved from <https://public.ebookcentral.proquest.com/choice/publicfullrecord.aspx?p=3111481>

- Davidson, T. W. (1964). Measurement of net thrust in flight. *Journal of Aircraft*, 1(3), 107 - 117. doi: 10.2514/3.43575
- Del Mónico Monteiro, P., Machiaverni, R. M., Bringhenti, C. & Tomita, J. T. (2018). In-flight thrust determination for high-bypass-ratio turbofan using residual error methodology. *Journal of the Brazilian Society of Mechanical Sciences and Engineering*, 40(2).
- Di Fiore Dos Santos, G., Lewis, R. J. & Barbosa, J. R. (2000). Residual error for in-flight thrust determination. In *Sae technical papers*. doi: 10.4271/2000-01-3251
- Er-Wei Bai, F. G. (2010). *Block-oriented nonlinear system identification* (1st ed.). Springer-Verlag London.
- FAA. (2016). *Airplane flying handbook faa-h-8083-3b*. United States Department of Transportation Oklahoma, OK.
- Ferrar, A. M., Schneck, W., Wicks, A. & O'Brien, W. (2016). Effects of total pressure inlet distortion on transonic fan blade wake properties. In *Proceedings of the asme turbo expo*. doi: 10.1115/GT2016-57703
- Ferry, J. D. (1980). *Viscoelastic properties of polymers*. John Wiley & Sons, Inc. doi: 10.1149/1.2428174
- Fisher, R. A. (1997). On an absolute criterion for fitting frequency curves. *Statistical Science*.
- Gent, A. N. (2012). *Engineering with Rubber: How to Design Rubber Components* (3th ed.). Cincinnati: Hanser Publications.
- Gruenberg, S., Blough, J., Kowalski, D. & Pistana, J. (2001). The effects of natural aging on fleet and durability vehicle engine mounts from a dynamic characterization perspective. In *Sae technical papers*. doi: 10.4271/2001-01-1449
- Grönstedt, T. & Zhao, Y. (2004, jun). A numerically efficient method for transient gas turbine performance estimation. In *40th AIAA/ASME/SAE/ASEE joint propulsion conference and exhibit*. American Institute of Aeronautics and Astronautics. doi: 10.2514/6.2004-4175
- Gudmundsson, S. (2014). Selecting the Power Plant. In *General aviation aircraft design*. doi: 10.1016/b978-0-12-397308-5.00007-6
- Guo, Y., Mao, J. & Zhou, K. (2015). Rate-dependent modeling and H_∞ robust control of gma based on hammerstein model with preisach operator. *IEEE Transactions on Control Systems Technology*, 23, 2432–2439. doi: 10.1109/TCST.2015.2413497
- Haeussler, M., Klaassen, S. W. & Rixen, D. J. (2020). Experimental twelve degree of freedom rubber isolator models for use in substructuring assemblies. *Journal of Sound and Vibration*. doi: 10.1016/j.jsv.2020.115253
- Hammerstein, A. (1930). Nichtlineare integralgleichungen nebst anwendungen. *Acta mathematica*, 54, 117–176.
- Harrison, M., Sykes, A. O. & Martin, M. (1952). Wave Effects in Isolation Mounts. *Journal of the Acoustical Society of America*, 24(1), 62–71. doi: 10.1121/1.1906850
- Harwood, J. A., Mullins, L. & Payne, A. R. (1965). Stress softening in natural rubber vulcanizates. Part II. Stress softening effects in pure gum and filler loaded rubbers. *Journal of Applied Polymer Science*. doi: 10.1002/app.1965.070090907
- Holt, W. L. (1932). Behavior of Rubber under Repeated Stresses. *Rubber Chemistry and Technology*. doi: 10.5254/1.3539319
- Hughes, D. L. (1981). Comparison of Three Thrust Calculation Methods Using In-Flight Thrust Data. *NASA Technical Memorandum*, 62–85.
- Ibrahim, R. A. (2008). *Recent advances in nonlinear passive vibration isolators*. doi: 10.1016/j.jsv.2008.01.014
- Janczak, A. (2004). *Identification of nonlinear systems using neural networks and polynomial models: A block-oriented approach* (1st ed.). Springer.
- Jategaonkar, R. V. (2006). *Flight Vehicle System Identification - A Time Domain Methodology*. American Institute of Aeronautics and Astronautics.
- Jones, D. I. G. (2001). *Handbook of Viscoelastic Vibration Damping*. Chandler: John Wiley & Sons, LTD.

- Kari, L. (2001). Dynamic transfer stiffness measurements of vibration isolators in the audible frequency range. *Noise Control Engineering Journal*, 49(2), 88. doi: 10.3397/1.2839644
- Kari, L. (2003). On the dynamic stiffness of preloaded vibration isolators in the audible frequency range: Modeling and experiments. *The Journal of the Acoustical Society of America*, 113(4), 1909–1921. doi: 10.1121/1.1557214
- Keesman, K. J. (2011). *System identification: An introduction* (1st ed.). Springer-Verlag London.
- Kim, S. & Singh, R. (2001). Multi-dimensional characterization of vibration isolators over a wide range of frequencies. *Journal of Sound and Vibration*. doi: 10.1006/jsvi.2001.3617
- Kopczynski, T. (2011). *Five factors that can affect your weighing system's accuracy* (Tech. Rep.). San Diego: Hardy Process Solutions. Retrieved from <https://www.hardysolutions.com/tenants/hardy/documents/5factorsa.pdf>
- Laka, Z. K. (2016). *Dynamic stiffness and damping prediction on rubber material parts, FEA and experimental correlation* (Doctoral dissertation, London Metropolitan University). Retrieved from <http://repository.londonmet.ac.uk/1125/>
- Lakes, R. S. (1999). *Viscoelastic Solids*. Boca Raton, Florida: CRC Press.
- Larsen, R. T. (1966). Dynamic versus static spring rates for vibration mounts. In *Sae technical papers*. doi: 10.4271/660599
- Lei, X., Li, M., Zhang, Q., Gao, Y. & Wen, M. (2018). Direct thrust measurement flight test of aero-engine. *Hangkong Dongli Xuebao/Journal of Aerospace Power*. doi: 10.13224/j.cnki.jasp.2018.07.011
- Lei, X., Zhang, Q., Wen, M., Ren, R. & Lei, D. (2017). Mount thrust measurement technique for aero-engines and its tests. *Hangkong Xuebao/Acta Aeronautica et Astronautica Sinica*. doi: 10.7527/S1000-6893.2017.121190
- L'Erario, G., Fiorio, L., Nava, G., Bergonti, F., Mohamed, H. A. O., Benenati, E., ... Pucci, D. (2020). Modeling, Identification and Control of Model Jet Engines for Jet Powered Robotics. *IEEE Robotics and Automation Letters*. doi: 10.1109/LRA.2020.2970572
- Li, Y. G., MacCallum, N. R. & Pilidis, P. (2001). Pressure waves in volume effect in gas-turbine transient-performance models. *Journal of Propulsion and Power*, 17, 706–710. doi: 10.2514/2.5799
- Lin, T. R., Farag, N. H. & Pan, J. (2005). Evaluation of frequency dependent rubber mount stiffness and damping by impact test. *Applied Acoustics*. doi: 10.1016/j.apacoust.2004.10.004
- Lion, A. (1997). On the large deformation behaviour of reinforced rubber at different temperatures. *Journal of the Mechanics and Physics of Solids*, 45(11-12), 1805–1834. doi: 10.1016/S0022-5096(97)00028-8
- Ljung, L. (1999). *System identification: Theory for the user* (2nd Edition ed.). Prentice Hall.
- LORD. (2020a). *Aerospace & Defence Isolator Catalog*. LORD Corporation Aerospace Development Group. Retrieved from https://lordfulfillment.com/pdf/44/PC6116_AerospaceandDefenseIsolator.pdf
- LORD. (2020b). *LORD Engine Mount Solutions for Aircraft*. LORD Corporation Aerospace Development Group. Retrieved from http://files.lord.com/pdf/44/PB6065_EngineMountSolutions.pdf
- Menard, K. & Menard, N. (2020). *Dynamic Mechanical Analysis*. CRC Press.
- Milliken, W. F. (1947). *Progress in Stability and Control Research*. Journal of the aeronautical sciences.
- Morelli, E. A. & Klein, V. (2016). *Aircraft System Identification: Theory and Practice*. Sunflyte Enterprises.
- Muhammad, H., Kuntjoro, W. & Sritjahjono, B. E. (2000). In-Flight Thrust Determination by Load Measurement on the Engine Mounting System. In *Proceedings of the 22nd international congress of aeronautical sciences*.
- Mukhopadhyay, T., Adhikari, S. & Batou, A. (2019). Frequency domain homogenization for the viscoelastic properties of spatially correlated quasi-periodic lattices. *International Journal of Mechanical Sciences*. doi: 10.1016/j.ijmecsci.2017.09.004
- Mullins, L. (1949). Permanent Set in Vulcanized Rubber. *Rubber Chemistry and Technology*. doi: 10.5254/1.3543010

- Murata, H., Taguchi, N., Hamada, T. & McCabe, J. F. (2000). Dynamic viscoelastic properties and the age changes of long-term soft denture liners. *Biomaterials*. doi: 10.1016/S0142-9612(00)00010-7
- Neef, M. F., Fritzen, C. P. & Schuhmacher, G. (2003). Evaluation of mount loads in dynamic testing of a jet engine. *Mechanical Systems and Signal Processing*, 17(3), 665–681. doi: 10.1006/mssp.2001.1405
- Negrão, J. R. P., Fanton, R. E., de La Fuente, R. P. & Barbosa, J. R. (1998, 11). In-Flight Thrust Determination. In *Sae technical paper*. Retrieved from <https://www.sae.org/content/982869/> doi: 10.4271/982869
- Nelles, O. (2021). *Nonlinear system identification: From classical approaches to neural networks, fuzzy models, and gaussian processes* (2nd ed.). Springer.
- Ooi, L. E. & Ripin, Z. M. (2011). Dynamic stiffness and loss factor measurement of engine rubber mount by impact test. *Materials and Design*, 32(4), 1880–1887. doi: 10.1016/j.matdes.2010.12.015
- Oppenheim, A., Willsky, A. & Nawab, S. (1997). *Signals and Systems (Second Edition)*. Prentice-Hall International, Inc.
- Pain, H. J. (2005). *The Physics of Vibrations and Waves: Sixth Edition* (Sixth ed.). Chichester: John Wiley & Sons Ltd. doi: 10.1002/0470016957
- Paoletta, M. S. (2019). *Linear Models and Time-Series Analysis*. Oxford: John Wiley & Sons Ltd.
- Payne, A. R., Whittaker, R. E. & Smith, J. F. (1972). Effect of vulcanization on the low-strain dynamic properties of filled rubbers. *Journal of Applied Polymer Science TA - TT -*, 16(5), 1191–1212. doi: 10.1002/app.1972.070160513LK-<https://tudelft.on.worldcat.org/oclc/5154251360>
- Pratt & Whitney. (1975). *Installation Handbook JT15D*. Longueuil: Pratt & Whitney.
- Rantzer, M., A.; Johansson. (2000). Piecewise linear quadratic optimal control. *IEEE Transactions on Automatic Control*, 45, 629–637. doi: 10.1109/9.847100
- Ray, R. J. (1994). *Evaluating the dynamic response of in-flight thrust calculation techniques during throttle transients*. Washington: NASA.
- Riande, E., Díaz-Calleja, R., Prolongo, M. G., Masegosa, R. M. & Salom, C. (2000). *Polymer Viscoelasticity : Stress and Strain in Practice* (D. Hudgin, Ed.). Ney York: Marcel Dekker.
- Rivin, E. I. (2003). *Passive vibration isolation*. ASME Press.
- Robb, G. (1965). *Hewlett packard catalog* (Vol. 25). Retrieved from <http://hparchive.com/Catalogs/HP-Catalog-1965.pdf>
- Schreurs, P. (2012). One-dimensional Material Behaviour. In *Material models*. Retrieved from <http://www.mate.tue.nl/~piet/edu/mmm/pdf/mmmsy11213.pdf>
- Sepe, M. (1998). *Dynamic mechanical analysis for plastics engineering*.
- Sjöberg, M. & Kari, L. (2002). Non-linear behavior of a rubber isolator system using fractional derivatives. *Vehicle System Dynamics*. doi: 10.1076/vesd.37.3.217.3532
- Sjöberg, M. & Kari, L. (2003). Nonlinear isolator dynamics at finite deformations: An effective hyperelastic, fractional derivative, generalized friction model. *Nonlinear Dynamics*. doi: 10.1023/A:1026037703124
- Smallman, R. & Bishop, R. (1999). *Modern Physical Metallurgy and Materials Engineering Science, process, applications*.
- Snowdon, J. C. (1980). Vibration Isolation: use and Characterization. *Rubber Chemistry and Technology*. doi: 10.5254/1.3535079
- Tanner, R. I. (2000). *Engineering Rheology* (2nd ed.). Oxford University Press.
- Textron. (2020a). *Cessna 560XL Aircraft Maintenance Manual*. Wichita: Textron Aviation Inc.
- Textron. (2020b). *Cessna model 550 Illustrated Parts Catalog*. Wichita: Textron Aviation Inc.
- Tischler, M. B. & Remple, R. K. (2006). *Aircraft and Rotorcraft System Identification*. American Institute of Aeronautics and Astronautics (AIAA). doi: 10.2514/4.868207

- Vahdati, N. & Saunders, L. K. L. (2002). High frequency testing of rubber mounts. *ISA Transactions*. doi: 10.1016/s0019-0578(07)60074-3
- Vörös, J. (1995). Identification of nonlinear dynamic systems using extended hammerstein and wiener models. *Control Theory Adv. Technol.*, 10(4), 1203–1212.
- Vörös, J. (1997a, jun). Parameter identification of discontinuous hammerstein systems. *Automatica*, 33(6), 1141–1146. Retrieved from [https://doi.org/10.1016/s0005-1098\(97\)00009-5](https://doi.org/10.1016%2Fs0005-1098%2897%2900009-5) doi: 10.1016/s0005-1098(97)00009-5
- Vörös, J. (1997b, jun). Parameter identification of discontinuous hammerstein systems. *Automatica*, 33(6), 1141–1146. doi: 10.1016/s0005-1098(97)00009-5
- Vörös, J. (1999). Iterative algorithm for parameter identification of hammerstein systems with two-segment nonlinearities. *IEEE TRANSACTIONS ON AUTOMATIC CONTROL*, 44.
- Vörös, J. (2001). Parameter identification of wiener systems with discontinuous nonlinearities. *Systems & Control Letters*, 44, 363–372. doi: 10.1016/s0167-6911(01)00155-4
- Vörös, J. (2002). Modeling and parameter identification of systems with multisegment piecewise-linear characteristics. *IEEE Transactions on Automatic Control*, 47(1), 184–188. doi: 10.1109/9.981742
- Vörös, J. (2003, 12). Recursive identification of hammerstein systems with discontinuous nonlinearities containing dead-zones. *IEEE Transactions on Automatic Control*, 48, 2203–2206. doi: 10.1109/TAC.2003.820146
- Vörös, J. (2005). Identification of hammerstein systems with time-varying piecewise-linear characteristics. *IEEE Transactions on Circuits and Systems II: Express Briefs*, 52, 865–869. doi: 10.1109/TCSII.2005.853339
- Wang, P., Su, Z., Lai, L., Jiang, H. & Wang, J. (2015). Engine isolate mount elastomers. In *Proceedings of the 2015 international conference on structural, mechanical and material engineering* (pp. 5–9). doi: 10.2991/icmmme-15.2015.2
- Wang, Z., Golob, M. J. & Chesler, N. C. (2016). Viscoelastic Properties of Cardiovascular Tissues. In *Viscoelastic and viscoplastic materials*. doi: 10.5772/64169
- Ward, I. M. & Sweeney, J. (2004). *An Introduction to the Mechanical Properties of Solid Polymers* (Vol. 2). John Wiley & Sons, Inc. doi: 10.5860/choice.42-2247
- Wheeler, A. J. & Ganji, A. (2009). *Introduction to Engineering Experimentation* (3th ed.). Prentice Hall.
- Wiener, N. & Teichmann, T. (1959). Nonlinear problems in random theory. *Physics Today*, 12(8), 52.
- Williams, M. L., Landel, R. F. & Ferry, J. D. (1955). The Temperature Dependence of Relaxation Mechanisms in Amorphous Polymers and Other Glass-forming Liquids. *Journal of the American Chemical Society*. doi: 10.1021/ja01619a008
- Wrong, C. B. (1969). An introduction to the JT15D engine. In *Proceedings of the asme turbo expo*. doi: 10.1115/69-GT-119
- Zadeh, L. A. (1962). From Circuit Theory to System Theory. In *Proceedings of the ire* (Vol. 50, pp. 856–865).
- Zanette, F. A., João Vitor; de Almeida. (2016). Realsysid: A software tool for real-time aircraft model structure selection and parameter estimation. *Aerospace Science and Technology*, 54, 302–311. doi: 10.1016/j.ast.2016.04.025

Appendix A

Model performance on validation data

